UNIVERSIDAD COMPLUTENSE DE MADRID

FACULTAD DE CIENCIAS FÍSICAS

SOLITONES ÓPTICOS BIDIMENSIONALES EN SISTEMAS DISIPATIVOS

MEMORIA PARA OPTAR AL GRADO DE DOCTOR
PRESENTADA POR

Cristian Mejía-Cortés

Bajo la dirección del doctor

José María Soto Crespo

Madrid, 2013

Two-Dimensional Optical Solitons in Dissipative Systems

By

Cristian Mejía-Cortés

Thesis Advisor: Jose María Soto Crespo

A thesis submitted to

UNIVERSIDAD COMPLUTENSE
MADRID

for the degree of
Doctor of Philosophy
Faculty of Physics
September 2012

Typeset in $\LaTeX\,2_\varepsilon$.

Except where acknowledged in the customary manner, the results presented in this thesis is, to the best of my knowledge, original and has not been submitted in whole or part for a degree in any university.

Cristian Mejía-Cortés

Todos vuelven a la tierra en que nacieron;
al embrujo incomparable de su sol.
Todos vuelven al rincón de donde salieron:
donde acaso floreció más de un amor.

Bajo el árbol solitario del pasado,
cuántas veces nos ponemos a soñar
todos vuelven, por la ruta del recuerdo,
pero el tiempo del amor no vuelve más.

El aire, que trae en sus manos la flor del pasado, y su aroma de ayer,
nos dice muy quedo al oído su canto aprendido del atardecer;
nos dice, con voz misteriosa de cardo y de rosa, de luna y de miel,
que es santo el amor de la tierra,
que es triste la ausencia que deja el ayer.

Todos vuelven.

RUBEN BLADES

Preface

This Doctoral Thesis concludes a big step of my research on *Optical Solitons*, which has been developed in about four years. The concept of optical soliton caught my imagination during the last year of my undergraduate studies. At that time, I begun exploring this exciting field focusing my interest on temporal solitons. This topic bore principally two aspects that became very interesting to me: its theoretical formulation through the classical field theory and their technological applications in telecommunications.

I am grateful to my supervisor: Dr. Jose María Soto Crespo, from whom I learned a lot about this field, in particular, the fascinating world of computational physics. Thanks for all the time you devoted to this research. Professors Mario Molina and Rodrigo Vicencio deserve special thanks for their continuous support and valuable advice during my Ph.D. studies. The internship developed in their research group (Nonlinear Optics Group) in Santiago, Chile, was a fruitful scientific experience.

This dissertation could not have been completed without the support of a large number of people. I would like to thank the members of the Optics Institute at the Spanish Research Council, CSIC. Thanks to the people of the MIX-2 Volleyball club, and in general to everyone who shared great moments to either side of the net. You have been my family here...

The first part of this book corresponds with a brief summary written in Spanish, as it is demanded by Universidad Complutense de Madrid, UCM. I would like to thank to UCM for letting me to write my Thesis in English. The financial support of the Spanish Ministry of Education and Science under project FIS2006-03376 via the FPI research fellowship as well as the project FIS2009-09895, are acknowledged.

Cristian Mejía Cortés
September, 2012.

Dedicado a mi familia...

Resumen

Capítulo 1 - Introducción

Hoy en día, la comunidad científica emplea cada vez más modelos no lineales para alcanzar una comprensión fundamental de la naturaleza. Las ondas solitarias (*solitones*) son una de las soluciones más importantes y fascinantes de las ecuaciones que describen los fenómenos no lineales. Históricamente, este tipo de ondas se observaron por primera vez en sistemas hidrodinámicos, pero con el paso del tiempo, se han observado en otras ramas de la ciencia tales como: química, biología, economía, ciencias sociales, etc. En física, solitones han sido reportados en áreas como: plasmas, sistemas magnéticos, materiales superconductores, condensados de Bose-Einstein y en óptica no lineal.

En general, todos los sistemas físicos en los que existen ondas localizadas se caracterizan principalmente por manifestar dos efectos que provienen de naturalezas diferentes. Por ejemplo, en los sistemas hidrodinámicos el efecto de la gravedad y la tensión superficial actúan sobre las ondas de agua como una fuerza de restauración que contribuye a su ensanchamiento (dispersión). De otra lado, cada uno de nosotros ha observado cómo una ola en el mar aumenta su altura cuando ésta se aproxima a la playa; su amplitud se vuelve tan grande que la ola rompe. Esta modificación en la forma de la onda es predominantemente un proceso no lineal. Entonces, si tenemos un sistema en el que la dispersión y no linealidad están débilmente presentes, sus efectos pueden llegar a balancearse de tal manera que pueda originarse una onda solitaria.

Comúnmente, a estas ondas solitarias se les conoce como solitones por que, a pesar de su naturaleza ondulatoria, en muchos fenómenos se comportan como partículas. En efecto, los solitones son objetos físicos que pueden sufrir colisiones con otras ondas localizadas y su forma posterior no cambia dramáticamente.

En óptica no lineal, una de las ecuaciones no lineales de evolución más utilizada es la ecuación no lineal de Shcrödinger (NLS). Dicha ecuación describe la evolución de una onda en un medio con dispersión/difracción y en el que, además, el índice de refracción cambia linealmente con la intensidad de la luz (Efecto Kerr). En modelos conservativos, tales como los descritos por la ecuación NLS o sus diversas variantes, el intercambio de energía con el entorno no está permitido. Las soluciones localizadas para la ecuación NLS se originan a partir del balance entre la difracción/dispersión cromática y la no linealidad (efecto Kerr). Distinto sucede en los sistemas disipativos donde las soluciones pueden intercambiar energía con una fuente externa, lo cual hace más compleja, pero a su vez más interesante, la descripción del sistema.

Los sistemas disipativos son los mas comunes en la naturaleza. De hecho cualquier otro modelo físico es solo una idealización. Los llamados conservativos o Hamiltonianos proporcionan modelos adecuados para el tratamiento matemático de dinámicas simples pero no funcionan bien para describir sistemas reales, especialmente en largos periodos temporales. Como sistemas disipativos se tiende a pensar en aquellos que sólo tienen pérdidas y por lo tanto cualquier solución se desvanece paulatinamente al propagarse a través de ellos. No son estos los que ocuparán nuestra atención a lo largo de esta tesis. Nosotros entendemos por sistemas disipativos aquellos que poseen pérdidas, pero además disponen de una fuente externa de energía que es capaz de compensarlas. Ello permite la existencia de soluciones estacionarias y estables las cuales hoy en día se conocen como solitones disipativos. Ejemplos de tales solitones en óptica son los pulsos ultracortos en láseres y las estructuras espaciales en láseres de gran apertura. En este último tipo de láseres también puede formarse solitones disipativos espacio-temporales.

En sistemas conservativos se asume un medio no lineal infinito, pero, como es de esperar, en la realidad los medios (disipativos) tienen dimensiones finitas. De hecho, excepto en las fibras ópticas, los solitones rara vez pueden propagarse más allá de unos pocos centímetros antes de salir del medio. Por lo tanto, para aumentar la longitud de propagación, es conveniente colocar espejos en los extremos del sistema (láser), y así confinar el solitón en una muestra de material con tamaño finito. Si nuestros espejos reflejaran perfectamente (sin absorción), uno podría confinar un solitón en una caja (cavidad); pero aunque los espejos reales están hechos de materiales que sufren perdidas, aún así es posible compensarlas con un señal que amplifique al solitón.

En general, cualquier láser está compuesto de diferentes elementos; esto hace que la modelización de ellos requiera un conjunto de varias ecuaciones. Este ejercicio puede ser necesario cuando buscamos una descripción detallada de un láser en particular. Dado que la luz se propaga secuencialmente a través de cada uno de los elementos, es posible realizar un estudio más general basado en una ecuación maestra, que recoja de manera distribuida cada uno de los efectos esenciales que ocurren en una cavidad láser.

La ecuación compleja de Ginzburg-Landau (ECGL) de quinto orden es un modelo genérico que describe la formación de ondas localizadas en láseres. Su versión más simple ocurre cuando la distribución transversal del campo está fijada por la geometría del láser (láser de fibra), debido a que el campo está confinado espacialmente (transversalmente) y por lo tanto el fenomeno de difracción es suprimido. Cuando la distribución transversal del campo no está fijada por la geometría, la ecuación ECGL de quinto orden ha de ser complementada con un término que de cuenta de la difracción del haz y de cualquier tipo de filtrado espacial.

A lo largo de este trabajo nos restringiremos al estudio de ondas localizadas espacialmente, analizaremos la propagación de un campo eléctrico $E(x, y, z)$ de una onda monocromática de frecuencia ω que se propaga a lo largo de la dirección z. Dicho campo se supone que es transversal, es decir, se halla polarizado en el plano (x, y) y varía lentamente a lo largo de la dirección z. La propagación de una onda de estas características en una cavidad láser puede ser descrita a través de la siguiente ECGL

$$i\psi_z + \frac{\mathcal{D}}{2}\nabla_\perp^2 \psi + |\psi|^2\psi + \nu|\psi|^4\psi = i\delta\psi + i\varepsilon|\psi|^2\psi + i\beta\nabla_\perp^2 \psi + i\mu|\psi|^4\psi. \tag{1}$$

Esta ecuación predice la existencia de solitones espaciales disipativos en sistemas (2+1)D, y es el modelo que hemos usado para predecir todos los resultados reportados en el capítulo 3 de este trabajo.

El capítulo 4 de esta tesis está dedicado al análisis de sistemas discretos bidimensionales con disipación. En fotónica, el modelo discreto mas estudiado es la ecuación NLS, la cual describe la propagación de la luz en arreglos de guías de onda. Las soluciones localizadas de la ecuación NLS discreta, comúnmente se conocen como *solitones discretos*, y ellos corresponden con estados auto atrapados de la luz. La extensión al caso disipativo de la ecuación discreta NLS surgió con el fin de modelar un conjunto de cavidades acopladas, las cuales fueron obtenidas colocando espejos tanto al inicio como al final de las guías de onda.

La ecuación usada para modelar dicho sistema fue la versión 1D discreta de la ECGL, la cual puede escribirse como:

$$i\dot{\psi}_n + \hat{C}\psi_n + |\psi_n|^2\psi_n + \nu|\psi_n|^4\psi_n = i\delta\psi_n + i\varepsilon|\psi_n|^2\psi_n + i\mu|\psi_n|^4\psi_n. \tag{2}$$

En realidad, la Eq. (2) es un sistema de ecuaciones diferenciales ordinarias no lineales acopladas, las cuales describen la evolución del campo a lo largo de cada una de las guías de onda.

Tanto en el caso continuo como en el caso discreto, los solitones espaciales disipativos en dos dimensiones son excitaciones ópticas auto-localizadas, las cuales no dependen de las condiciones de frontera en el plano transversal al eje de propagación. Una de las propiedades más interesantes es que pueden estar presentes o ausentes bajo las mismas condiciones externas, esto es, el sistema es biestable. La gran mayoría de los resultados reportados en esta esta Tesis Doctoral tienen origen en el fenómeno de biestabilidad. Para un mismo conjunto de parámetros, tanto en la Eq. (1) como en la Eq. (2), hemos encontrado soluciones con diferentes características.

A lo largo de las siguientes secciones se realiza un breve resumen de los resultados obtenidos y conclusiones, expuestos en los capítulos que conforman esta Tesis doctoral.

Capítulo 2 - Ecuaciones nolineales de propagación

En este capítulo se hace una retrospección sobre el origen físico de las ecuaciones que gobiernan la propagación de ondas localizadas, tanto para medios continuos como para medios discretos. A partir de las ecuaciones de Maxwell y asumiendo una dependencia no lineal entre el campo eléctrico y la polarización del medio, hemos derivado la ecuación NLS. Esta ecuación describe la evolución de un haz en un medio continuo, en el régimen de aproximación paraxial.

A través de la ecuación NLS hemos modelado la dinámica que experimenta la luz cuando se propaga a través un sistema de guías de onda acopladas. Para conseguir esto hemos empezado describiendo cómo interactúa la luz en un sistema compuesto por dos guías de onda, es decir, cómo el campo óptico de una guía se acopla con el campo de la guía vecina, y viceversa. Este resultado puede ser fácilmente extendido a un caso con N guías de onda, con la condición de que el acoplamiento sólamente se de entre guías vecinas, lo cual es conocido en física del estado sólido como “la aproximación del enlace fuerte”.

Capítulo 3 - Medios Continuos

Los sistemas disipativos bidimensionales admiten la existencia de soluciones estacionarias auto-localizadas sobre un fondo de energía cero. Entre ellas encontramos haces que poseen simetría radial y su perfil de intensidad tiene forma de campana. Estas estructuras pueden ser clasificadas en dos grandes conjuntos; el primero de ellos se caracteriza por estar compuesto de soluciones que están continuamente enfoncandose, es decir que poseen un *chirp* positivo. El segundo conjunto lo conforman soluciones que continuamente están desenfocandose, y a las cuales les corresponde un *chirp* negativo.

Estos haces -*o solitones espaciales brillantes*- son estables dentro de cierta región de su existencia. Más allá de estas regiones, ellos pierden su estabilidad, y aparecen nuevos comportamientos en su dinámica. Como mencionamos previamente, los solitones espaciales brillantes no son los únicos haces auto-localizados que se pueden encontrar en un fondo de energía cero para medios disipativos. Soluciones autolocalizadas tipo vórtice -*o solitones vórtice*-, también son estables en un rango finito de parámetros de la ECGL. Dichas soluciones están caracterizadas por una cantidad entera conocida como la carga topológica, la cual nos dice el número de 2π-vueltas que da la fase alrededor del vórtice.

En este capítulo, se presentan varios tipos de inestabilidades relacionadas con cada configuración de los haces y también se dan ejemplos de nuevas dinámicas en las zonas adyacentes a la región de estabilidad. A éstas nuevas dinámicas corresponden estructuras asimétricas, estructuras complejas formadas por la interacción entre dos haces, y por último estructuras con perfiles espaciales oscilantes.

Capítulo 4 - Medios Discretos

Estructuras discretas auto localizadas en medios no lineales - *o solitones discretos*- son soluciones de un sistema de ecuaciones diferenciales acopladas, que describen la evolución de la luz en un arreglo de guías de onda o cavidades laser. Este tipo de soluciones han sido predichas en medios multidimensionales y además han sido observadas experimentalmente. Los solitones discretos unidimensionales fueron reportados en arreglos de guías de onda fabricados con materiales semiconductores. Para poder observar este tipo de soluciones en dos dimensiones, fue necesario inducir patrones periódicos transversales mediante la interferencia de cuatro haces, en cristales fotorefractivos, los cuales actuaban como guías.

Mediante la combinación de diferentes métodos, hemos encontrado un gran conjunto de soluciones de tipo vórtice para la versión discreta de la ECGL. Dicho conjunto corresponde con un sólo valor para cada uno de los parámetros en la Eq. (2). Además, para cada una de estas soluciones hemos calculado su estabilidad frente a pequeñas perturbaciones en el régimen lineal.

Entre todas las soluciones estables que hemos encontrado, cabe destacar que, algunas de ellas tienen la fascinante característica de poseer, simultáneamente, dos cargas topológicas. Esto quiere decir que hemos encontrado dos valores distintos de la carga topológica para dos caminos distintos que encierran la singularidad del vórtice. Adicionalmente, hemos predicho la formación dinámica de una variedad de "estados ligados", compuestos de dos o más de estos vórtices con dos cargas.

Para concluir este capítulo, hemos analizado los casos mas interesantes en el limite cúbico conservativo. Paulatinamente hemos suprimido todos y cada uno de los parámetros de la Eq. (2) hasta alcanzar el limite de Schrödinger, es decir: $\{\delta = \varepsilon = \mu = \nu = 0\}$. A través de este procedimiento, hemos podido comprobar que hay una estrecha relación entre la disipación presente en el sistema y la estabilidad de sus soluciones; en la práctica esto se vio reflejado en que a pesar de que éstas también existen en el caso conservativo, su región de estabilidad disminuía conforme la disipación iba desapareciendo del sistema.

Conclusiones

A lo largo de esta tesis Doctoral se ha analizado la existencia, dinamica, formación e interacción de estructuras de luz autolocalizadas, en sistemas no lineales disipativos, tanto para medios continuos como también para medios discretos.

Para el caso de medios continuos disipativos, hemos estudiado la evolución de una gran variedad de solitones espaciales bidimensionales. En particular, nos hemos restringido a ciertos subespacios cercanos a las fronteras de las regiones en las que solo existen soluciones estacionarias radialmente simétricas. En estos, hemos encontrado una multiplicidad de solitones con distintos perfiles transversales y un sinfín de bifurcaciones entre ellos. Adicionalmente, hemos podido concluir que la distribución transversal del modo y su evolución depende fuertemente de la región en el espacio de parámetros que nos encontremos.

Hemos encontrado varios tipos de bifurcaciones en las fronteras de la región donde existen soluciones, estacionarias y estables, que están continuamente enfoncándose. Bifurcaciones de haces radialmente simétricos a haces con distribución elíptica, pasando luego por regiones en las que encontramos haces con pulsaciones armónicas (e incluso pulsaciones más complejas) en su perfil espacial, los cuales además de estar pulsados también pueden girar alrededor de su eje de propagación. Estos escenarios de evolución son consecuencia de los intentos fallidos de división del haz en dos solitones brillantes. En general, cualquier bifurcación alrededor de esta región destruye la simetría radial de la solución.

Muy cerca de la región donde existen soluciones, estacionarias y estables, que están continuamente desenfoncandose, el haz mantiene su simetría radial después de la bifurcación. En este caso los haces tienen pulsaciones en su perfil de intensidad, pero su distribución transversal mantiene la simetría radial. Aun más, esta clase de haces pueden sufrir “explosiones” que fugazmente los despojan de cualquier clase de simetría, pero que increiblemente vuelven a recuperar su perfil original entre cada una de las explosiones.

Por otro lado, para el mismo tipo de medio, también hemos estudiado la formación de estructuras tipo vórtice. Al igual que antes, hemos encontrado regiones donde ellos existen en forma de soluciones estacionarias y estables, compartiendo todos una distribución de intensidad en forma de anillo. A partir de nuestro análisis, hemos comprobado que su existencia está garantizada para un rango amplio de valores de su carga topológica, el cual contiene valores para S que van desde 1 hasta 9.

Estas soluciones solitónicas con forma de anillo pueden sufrir transformaciones y su perfil espacial llegar a ser modulado. Éstas también pueden pulsar de forma periódica o caótica. A pesar de todos estos tipos de modificaciones, las soluciones permanecen estables como un único anillo, conservando su carga topológica. Estas propiedades los hacen completamente distintos de los solitones vórtice en sistemas conservativos.

Para el caso de medios discretos disipativos, hemos predicho la existencia de solitones vórtice con valores altos de su carga topológica. Entre ellos hemos podido identificar estructuras tanto simétricas como asimétricas. Adicionalmente, para algunas soluciones hemos identificado a partir de su perfil de fase, la coexistencia de dos cargas topológicas. Es decir, la solución exhibe simultaneamente dos valores distintos para dicha característica.

También hemos hecho un análisis de estabilidad lineal para las soluciones cuando la disipación en el sistema es modificada. Hemos observado que el tamaño de la región de estabilidad en el espacio de parámetros aumenta a medida que se incrementa la disipación. Para efectos comparativos, hemos buscado este tipo de soluciones en el modelo cúbico en sistemas conservativos (ecuación NLS), estableciendo que dichas soluciones solamente son estables para valores de potencia óptica mucho mas altos que en el correspondiente caso disipativo analizado.

Para terminar, y con animo de completar la descripción de este tipo de sistemas, hemos estudiado distintos escenarios de interacción para algunas de las soluciones anteriormente descritas. Hemos analizado la interacción entre soluciones de la misma familia para diferentes separaciones iniciales. Como resultado, hemos encontrado soluciones compuestas ("estados enlazados") que también son estables y que además poseen un perfil de fase bastante complejo, en el cual también pueden identificarse, simultáneamente, dos cargas topológicas. Por otro lado, la interacción entre soluciones de distinta familia no conduce a la formación de estructuras compuestas.

List of Publications

Papers

- J. M. Soto-Crespo, N. Akhmediev, N. Devine and C. Mejía-Cortés, *Transformations of continuously self-focusing and continuously self-defocusing dissipative solitons.* Opt. Express. **16**, pp. 15388-15401 (2008).
- J. M. Soto-Crespo, N. Akhmediev, C. Mejía-Cortés and N. Devine. *Dissipative ring solitons with vorticity.* Opt. Express. **17**, pp. 4236-4250 (2009).
- C. Mejía-Cortés, J. M. Soto-Crespo, Mario I. Molina and Rodrigo A. Vicencio. *Dissipative vortex solitons in two-dimensional lattices.* Phys. Rev. A. **82**, 063818 [5 pages] (2010).
- C. Mejía-Cortés, J. M. Soto-Crespo, Rodrigo A. Vicencio, and Mario I. Molina. *Vortex solitons of the discrete Ginzburg-Landau equation.* Phys. Rev. A. **83**, 043837 [6 pages] (2011).
- C. Mejía-Cortés, J. M. Soto-Crespo, Rodrigo A. Vicencio, and Mario I. Molina. *Bound states and interactions of vortex solitons in the discrete Ginzburg-Landau equation.* Phys. Rev. A. **86**, 023834 [9 pages] (2012).

Other Publications

- J. M. Soto-Crespo and C. Mejía-Cortés. *Optical solitons in dissipative media.* Opt. Pura Apl. **44** (3) 425-431 (2011).

Congress Contributions

- N. Devine, J. M. Soto-Crespo, N. Akhmediev and C. Mejía-Cortés. *Bifurcations of two transverse dimensional dissipative solitons and antisolitons.* **Australian Institute of Physics 18th National Congress**. (AIP) 30 November - 5 December (2008). Adelaide, Australia.
- N. Devine, J. M. Soto-Crespo, C. Mejía-Cortés and N. Akhmediev. *Dissipative ring solitons with high value of vorticity.* **European Quantum**

Electronics Conference (EQEC). 14 - 19 June (2009). Munich, Germany.

- C. Mejía-Cortés, J. M. Soto-Crespo, N. Devine, and N. Akhmediev. *Rotura de simetría y dinámicas complejas de solitones disipativos.* **IX Reunión Nacional de Óptica** (RNO). 14 - 17 September (2009). Ourense, Spain.
- C. Mejía-Cortés, J. M. Soto-Crespo, N. Akhmediev and N. Devine. *Transformations of Continuously Self-Focusing Dissipative Solitons.* **Australasian Conference on Optics, Laser and Spectrocopy** (ACOLS), **Australian Conference on optical Fibre Technology** (ACOFT) and **International Workshop on Dissipative Solitons** (DS). 29 November - 3 December (2009). Adelaide, Australia.
- C. Mejía-Cortés, J. M. Soto-Crespo, Mario I. Molina and Rodrigo A. Vicencio. *Discrete vortex solitons in 2D Ginzburg-Landau lattices.* **Complexity in Periodically Structured Systems, International Workshop**. (CPSS). 30 August - 3 September (2010). Dresden, Germany.
- C. Mejía-Cortés and J. M. Soto-Crespo. *Vortex solitons of the discrete Ginzburg-Landau equation.* **VII Reunión Española de Optoelectrónica** (OPTOEL). 29 June - 1 July (2011). Santander, Spain.
- C. Mejía-Cortés, J. M. Soto-Crespo, Mario I. Molina and Rodrigo A. Vicencio. *Two-Dimensional Optical Solitons in Dissipative Systems.* **2nd Conference on Localized Excitations in Nonlinear Complex Systems** (LENCOS). 9 July - 12 July (2012). Sevilla, Spain.

Contents

"En cualquier lugar que estuvieran, recordarán siempre que el pasado era mentira, que la memoria no tenía caminos de regreso, que toda primavera antigua era irrecuperable, y que el amor más desatinado y tenaz era de todos modos una verdad efímera"

Gabriel García Márquez - Cien Años de Soledad

1

Introduction

This section provides an introduction to the research work presented in this thesis. It describes the research background and explains the motivation for pursuing this work. In addition it provides an overview of the approach taken as well as of the results obtained and finally presents the structure of the thesis.

1.1 Generalities

Nowadays, the scientific community is increasingly using nonlinear models to obtain a fundamental understanding of nature. Localized waves are one of the most important and fascinating solutions of the equations that describe nonlinear phenomena. Historically, this kind of waves were first observed in hydrodynamic systems, but over time, have been observed in other branches of science (physics, chemistry, biology, economy, social sciences, etc.). Through theoretical predictions and their subsequent experimental corroboration, these nonlinear localized waves, known as *solitons*, have been found in different physical disciplines, for example in fluids, plasmas, magnetic systems, super-conducting Josephson junctions, Bose-Einstein condensates and nonlinear optics.

In general, all the physical systems in which exists wave localization are characterized by two effects, both of them arising from a different nature. For example, in hydrodynamic systems the effect of the gravity and the surface tension acts on the water waves as a restoring force which contributes to their dispersion (spreading). On the other hand, every one has observed how a water wave increases as it approaches the beach; its amplitude becomes so great that the wave breaks down. This modification in the *shape* of the wave is predominantly a nonlinear process. Then, if we have a system in which weak dispersion and weak nonlinearity are present, *they can balance* and originate a solitary wave.

FIGURE 1.1: Soliton on the Scott Russell Aqueduct on the Union Canal near Heriot-Watt University, 12 July 1995.

The first reported observation of solitons was made in 1834 by Scott Russell, a Scottish scientist and later famous Victorian engineer and shipbuilder, while studying water waves in the Glasgow-Edinburgh channel. As part of this investigation, he was observing a boat being pulled along, rapidly, by a pair of horses. For some reason, the horses stopped the boat rather suddenly, and the stopping of the boat caused a very strong wave to be generated. This wave, in fact, a significant hump of water stretching across the rather narrow canal, rose up at the front of the boat and proceeded to travel, quite rapidly down the canal. Russell, immediately, realised that the wave was something very special. It was "alone", in the sense that it sat on the canal with no disturbance to the front or the rear, nor did it die away until he had followed it for quite a long way. The word "alone" is synonymous with "solitary", and Russell soon referred to his observation as the Great Solitary Wave.

On Wednesday 12 July 1995, an international gathering of scientists witnessed a re-creation of the famous 1834 "first" sighting of a soliton or solitary wave on the Union Canal near Edinburgh. They were attending a conference on nonlinear waves in physics and biology at Heriot-Watt University, near the canal, Fig. 1.1.

These solitary and localized waves are commonly called *solitons* due to their quasi-particle properties. Indeed, solitons are physical objects that can suffer collisions with other localized waves and their posterior shapes are not dramatically changed. Their existence and robustness against collisions was observed in the numerical solutions of the Korteweg-de Vries (KdV) equation (Zabusky & Kruskal, 1965). This equation governs the wave propagation in shallow water channels. Two years later (Gardner et al., 1967) developed a powerful mathematical technique, called the *inverse scattering transform*, which allowed to find analytically soliton-type solutions of the KdV equation.

The Korteweg and de Vries theory has been widely used; for example modeling the blood-pressure pulse propagation along the major arteries in the human body (McDonald, 1974). Besides the KdV equation, exists another nonlinear partial differential equation for the propagation of long waves on the surface of water with a small amplitude. The French scientist Joseph Boussinesq (1842-1929) described in the 1870s model equations for this system and these were called the Boussinesq equations.

Other equations with similar characteristics admit soliton solutions. For example, in mathematics, the sine-Gordon equation is a nonlinear hyperbolic partial differential equation in one-dimensional systems involving the d'Alembert operator and the sine of the unknown function. It was originally considered in the nineteenth century in the course of study of surfaces of constant negative curvature for a wide variety of physical and mathematical systems, for example, differential geometry and relativistic field theory. The sine-Gordon equation also appears in a number of physical applications including the propagation of fluxons in Josephson junctions (a junction between two superconductors), the motion of a rigid pendula attached to a stretched wire, and dislocations in crystals. (Baker, 1897; Bishop, 1981; Davydov, 1991; Infeld & Rowlands, 2000)

A Bose-Einstein condensate is a rare state (or phase) of matter in which a large percentage of bosons collapse into their lowest quantum state, allowing quantum effects to be observed on a macroscopic scale. The bosons collapse into this state in circumstances of extremely low temperature, near the value of absolute zero. The Gross-Pitaevskii equation describes the ground state of a quantum system of identical bosons using the Hartree-Fock approximation and the pseudo-potential interaction model. Dynamics of low-temperature super flows and Bose-Einstein Condensates (BEC) are some examples of physical systems governed by this equation (Denschlag et al., 2000; Rubi, 2004)

In nonlinear optics, one of the most widely used equations of this type is the nonlinear Schrödinger (NLS) equation; it describes wave evolution in dispersive/diffractive continuous media with an optical Kerr response, i.e. a refractive index that changes linearly with the light intensity. In conservative models, such as the ones described by the NLS equation or its several variants, the exchange of energy with the surroundings is not allowed. Self-localized solutions for the nonlinear Schrödinger equation originate from a balance between nonlinearity (e.g. the Kerr effect) and dispersion/diffraction. As we know, conservative models offers an useful description when we assume that the system is closed, i.e. its energy is not absorbed by the surroundings. In realistic systems, the energy exchange with an external source must be considered, then the dynamic of the system will be more complex and rich. In this case, an extra balance between gain and loss is required in order to obtain stationary solutions. This kind of systems are commonly known as *dissipative systems*.

1.2 Optical Solitons

As in hydrodynamic systems, a similar balance may occur when an optical beam/pulse propagates in a material. The diffractive/dispersive process experimented by the wave can be counteracted with the nonlinear response of the medium. This self compensation in the system gives rise to the formation of *optical solitons*. Generally, conventional sources of light are not intense enough to modify the optical response of the materials, but with the advent of lasers at the beginning of the 60's, several nonlinear optical phenomena could be observed.

Light propagating through a material induces a variation in its refraction index that is proportional to the incident intensity. This extra contribution to the refractive index is known as the optical Kerr effect (Boyd, 2008). In the spatial domain, this effect leads to a focusing (or defocusing) beam (as illustrated in Fig. 1.2[a]) and, in the temporal domain, the pulse suffers a phase modulation which induces a change in its spectrum (Fig. 1.2[b]). Diffraction and chromatic dispersion are equivalent effects that leads to the spatial and temporal spreading of the waves, beams and pulses, respectively. Localized waves are called *spatial optical solitons* when the beam shape remains unaltered due to the balancing between focusing and diffraction, and *temporal optical solitons* when the pulse shape (and its spectrum) is not modified due to the balancing between phase modulation and chromatic dispersion.

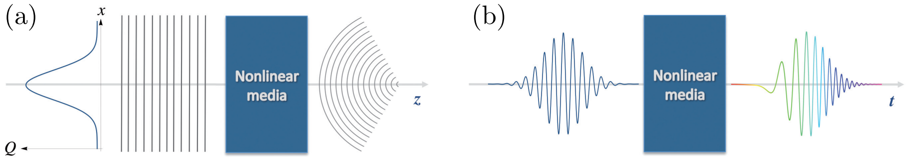

FIGURE 1.2: (a) Focusing and (b) Phase modulation effects on beams and pulses propagating through nonlinear media.

1.2.1 Temporal optical solitons

In general, the temporal and spectral shapes of a short optical pulse change during propagation in a transparent medium due to the Kerr effect and chromatic dispersion. As it was mentioned previously, under certain circumstances, the effects of Kerr nonlinearity and chromatic dispersion can exactly cancel each other (apart from producing a constant phase delay per unit propagation distance), so that the temporal and spectral shape of the pulses is preserved even over long propagation distances. The possibility of soliton formation in optical fibers was suggested by Hasegawa & Tappert (1973).

The nonlinear Schrödinger equation for temporal solitons propagating through an optical fiber takes the form

$$i\psi_z - \frac{\beta_2}{2}\psi_{tt} + \gamma\left|\psi\right|^2\psi = 0, \tag{1.1}$$

where $\psi(z,t)$ represents the amplitude of the pulse envelope, β_2 is the group velocity dispersion parameter (GVD), and γ is the nonlinear parameter responsible for self phase modulation (SPM). In this case, the Inverse Scattering Method is applicable for solving this kind of equations (Zakharov & Shabat, 1974).

However, the lack of a suitable source of picosecond optical pulses at wavelengths above 1.3 μm delayed their experimental observation until 1980 (Mollenauer et al., 1980). This experiment was carried out by using a mode-locked color-center laser capable of emitting short optical pulses ($T_{FWHM} \approx 7$ ps) near 1.55 μm, a wavelength near which optical fibers exhibit anomalous GVD together with minimum losses. The pulses were propagated inside a 700 meters long single-mode fiber with a core diameter of 9.3 μm. The fiber parameters for this experiment were estimated to be $\beta_2 \approx -20$ ps^2/km and $\gamma \approx 1.3$ W^{-1}/km. Using an initial pulse with a temporal width of T_0=4 ps, the peak power for exciting a fundamental soliton is ≈ 1 W.

Fundamental soliton pulses are technically very important, in particular for long-distance optical fiber communications (Govan et al., 1998; Hasegawa, 2002). Solitons are also applied in various techniques for pulse compression using optical fibers; examples are adiabatic soliton compression and higher-order soliton compression (Ouzounov et al., 2005).

1.2.2 Spatial optical solitons

The change of the refraction index in nonlinear materials can be understood as if the media became a convergent lens while the beam is propagating through it. The width and height of the beam diminishes and grows, respectively, which leads to a narrowing of the wave shape. This focusing of the beam is the opposite to the natural spreading that experiments a beam when it propagates in any linear homogeneous medium. Then, this balancing is equivalent to think in a emergent waveguide induced by the intensity of the beam. This effect is known as *self-trapping* and it is illustrated in Fig. 1.3.

The input beam diffracts at low power but forms a spatial soliton when its intensity is large enough to create a self-induced waveguide by changing the refractive index. This change is larger at the beam center and gradually reduces to zero near the beam edges. From all the above we can accept the following definition:

> *Spatial solitons are optical beams that propagate in a nonlinear medium without diffraction, i.e. their beam diameter remains invariant during propagation* (Stegeman et al., 2000).

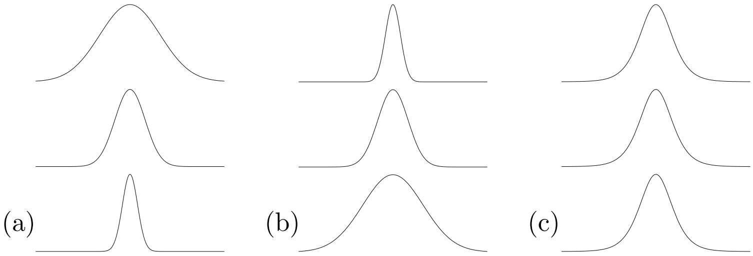

FIGURE 1.3: Schematic illustration of the lens analogy for spatial solitons. (a) Diffraction acts as a concave lens while the (b) Self-focusing medium acts as a convex lens. (c) A soliton forms when the two lenses balance each other such that the phase front remains plane.

Spatial solitons in nonlinear optical Kerr media were observed for the first time at the beginning of the 60s (Askaryan, 1962; Chiao et al., 1964). Kerr nonlinearities are characterized by a local, instantaneous refractive index change, $\Delta n = n_2 I$, where $I = |\psi|^2$ is the local intensity and n_2 is a real constant. All media exhibit the optical Kerr effect at frequencies very far from any resonances so that the nonlinearity is very weak. The change in the refractive index can not grow infinitely, it become saturated at high intensities. This is often taken into account by considering the following dependence on the change of the refractive index with the intensity:

$$\Delta n = -\frac{\Delta n_{max}}{1 + I/I_{sat}}, \tag{1.2}$$

where Δn_{max} denotes the maximum refractive index change. When the field intensity is much smaller than the saturation intensity, I_{sat}, the system operates in the Kerr-regime. In the other limit, for $I \gg I_{sat}$ the refractive index change decreases and thereby prevents the collapse of the light beam.

Temporal solitons propagate unaltered long distances along optical fibers. Optical fibers posses a very weak glass nonlinearity that becomes cumulatively sufficient for soliton formation. For spatial solitons it is necessary that nonlinearities and/or operating powers to be large enough, because sample sizes are typically limited to a few centimeters. What sets spatial solitons apart from their fiber counterparts is their dimensionality. Fiber solitons are described by a nonlinear $(1 + 1)$-dimensional space-time evolution equation, whereas spatial solitons are by nature $(2+1)$-dimensional structures (two transverse dimensions plus one propagation coordinate).

The properties of optical solitons in a non-Kerr media are governed by the generalized NLS equation (1.3). Using $\Delta n = n_2 F(I)$ with $n_2 > 0$, the $(2+1)$-dimensional NLS equation takes the form

$$i\psi_z + \frac{1}{2}\nabla^2\psi + F(I)\psi = 0 \tag{1.3}$$

The fact that the spatial domain exhibits a higher dimensionality leads to a host of interesting phenomena and processes, which have not analogous in the temporal case. These include for example, full 3D interaction between solitons, vortex solitons, rotating dipole vector solitons and many others. The consideration of additional degrees of freedom, such as new transverse dimensions, does lead to extremely sophisticated dynamics of the processes. A direct consequence of the fact that the number of different nonlinear mechanisms that can support spatial solitons is to date much larger than for their temporal counterparts. However, despite more than two decades of intense research, solitons were restricted to one-dimensional nonlinear propagation, i.e. to temporal or spatial one-dimensional solitons.

1.2.3 Optical vortex solitons

Optical beams whose phase circulates around a singular point -or central core-, changing by $2\pi S$ times in each closed loop around it (with S being an integer number), are called optical vortices. The integer number S is known as the topological charge of the vortex, and its sign defines the direction of the phase circulation. To introduce the notion of optical vortices, we recall that a light wave can be represented by a complex scalar function ψ (e.g. an envelope of an electric field), which varies smoothly in space and/or time. Phase singularities of the wave function ψ appear at the points at which its modulus vanishes, i.e. when $\mathbb{R}\{\psi\} = \mathbb{I}\{\psi\} = 0$. Such points are referred to as wave-front screw dislocations, because the surface of constant phase structurally resembles a screw dislocation in a crystal lattice.

Optical vortices are associated with zeros in light intensity (doughnut-like shape) and can be recognized by a specific helical wave front, the phase gradient direction swirls around the singular line much like fluid in a whirlpool, (Fig. 1.4). If the complex wave function is presented as $\psi(x, y, z) = A(x, y)\exp[i\theta(x, y, z)]$, in terms of its real modulus $A(x, y)$ and phase $\theta(x, y, z)$, the dislocation strength, S, is defined by the circulation of the phase gradient around the singularity,

$$S = \frac{1}{2\pi}\oint \nabla\theta \cdot \mathrm{d}\,\mathbf{l}. \tag{1.4}$$

In quantum information, they have an enormous potential for codifying information beyond two levels using their topological charge value (Molina-Terriza

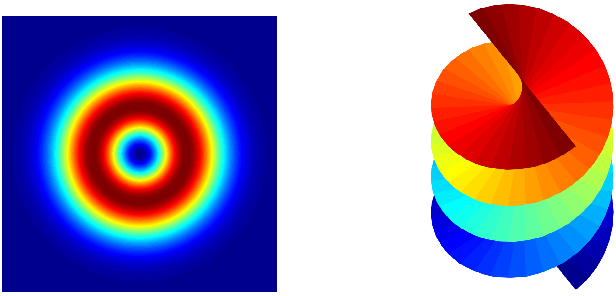

Figure 1.4: Typical characteristics of an optical vortex. To the left is illustrated the transversal distribution of the intensity of the field. To the right, is illustrated a 3D plot of the phase for an optical vortex with $S = 2$.

et al., 2001). In other fields, such as biophotonics for example, they are useful due to their ability to affect the motion of particles (microorganisms) through angular momentum transfer (Mair et al., 2001). Other scientific and technological applications for optical vortices are found in optical systems communication, spintronics and optical tweezers (Ashkin et al., 1987; Scheuer & Orenstein, 1999; Ganichev et al., 2001). These potential applications of optical vortices have intrigued to the scientific community because their basic properties and characteristics.

There exist two main categories to generate optical vortices: intra cavity excitation of a laser beam (Arecchi et al., 1991) and redistribution of a laser beam outside a laser cavity (Baranova et al., 1983). Laser cavities with large Fresnel numbers produce a set of non-stationary vortices (Arecchi et al., 1991). Selective excitations of frequency-degenerated transverse modes through locking techniques show regular arrangement of vortices, referred to as phase singularity crystals, at precisely defined positions (Brambilla et al., 1991). Dynamic optical vortices are also demonstrated in photorefractive oscillators (Malos et al., 1996) These laser cavity excitations sacrifice the TEM_{00} mode. In contrast, the generation of optical vortices outside a laser cavity can be achieved by modulating the amplitude and/or phase of an incident wave. Speckle patterns obtained by scattering light from random media show random distribution of optical vortices (Baranova et al., 1983). Computer-generated holograms, including spiral Fresnel zone plates (Heckenberg et al., 1992b) and synthesized diffraction gratings (Heckenberg et al., 1992a; Basistiy et al., 1995) are well-known techniques.

Optical vortices in nonlinear media can exist as dark beams, i.e. vortices produced by a phase dislocation which is embedded in an infinite background; and bright beams, with the vortex core embedded in the ground state (bell-shaped beam) with vanishing amplitude at infinity. Dark vortex solitons are stable only in self-defocusing nonlinear Kerr media, i.e. when the nonlinear refractive index of the media is negative.

On the other hand, bright vortex soliton are not stable in a medium with Kerr nonlinearity response, in fact, simple two-dimensional self trapped beams neither exist in this model. Instead, it predicts either eventual diffraction or catastrophic collapse for input power below or above a certain threshold value, respectively (Bergé, 1998). Hence, in order to ensure the existence of stable self-localized beams in two dimensions, a different nonlinear response is necessary. It is known that the saturation of nonlinearity, Eq. (1.2), at high intensities is sufficient to prevent collapse and provides stabilization of some two-dimensional beams (Kivshar & Pelinovsky, 2000). The physical mechanism behind the stabilizing action of the nonlinearity saturation is very simple: when a beam increases its amplitude the effective action of nonlinearity decreases, therefore preventing the further self-focusing and collapse.

However, for bright vortex solitons, the absence of the collapse does not guarantee dynamical stability. Unlike ground state, a ring tends to be strongly destabilized by azimuthal perturbations which break it up into several separating $S = 0$ bright solitons (the latter ones are stable). In models with quadratic (χ^2) and saturable nonlinearities, numerical simulations have revealed a strong azimuthal instabilities (Firth & Skryabin, 1997; Skryabin & Firth, 1998), which was later observed experimentally in a χ^2 medium (Petrov et al., 1998). In conservative systems, stabilization of a ring-shaped vortex soliton is possible only in some exceptional cases, one example being the competing quadratic and self-defocusing nonlinearities (Quiroga-Teixeiro & Michinel, 1997). A combination between cubic (focusing) and a quintic (defocusing) refractive index dependence, with the light intensity, also has been proposed to counteract the azimuthal instability (Quiroga-Teixeiro & Michinel, 1997; Michinel et al., 2001).

The chapter 3 of this thesis is devoted to analyze complex dynamics of (2+1)-dimensional solitons, both, bell-shaped and ring solitons will be analyzed in the frame of dissipative systems.

1.2.4 Discrete optical solitons

Wave propagation in nonlinear periodic lattices is associated with a host of exciting phenomena that have no counterpart whatsoever in bulk media. Perhaps, the most intriguing entities that can exist in such systems are discrete self-localized states better known as discrete solitons (Flach & Willis, 1998). Numerous applications of these phenomena have emerged ranging from nonlinear optics, in the dynamics of guided waves in inhomogeneous optical structures (Eisenberg et al., 2002; Peschel et al., 2002) and photonic crystal lattices (Efremidis et al., 2002; Sukhorukov et al., 2003), to atomic physics, in the dynamics of Bose-Einstein condensate droplets in periodic (optical lattice) potentials (Cataliotti et al., 2001, 2003; Abdullaev et al., 2001; Alfimov et al., 2002) and from condensed matter, in Josephson-junction ladders (Fistul, 2003; Mazo & Orlando, 2003), to biophysics, in various models of the DNA double strand (Dauxois et al., 1993; Peyrard et al., 1993).

Optical discrete solitons in nonlinear waveguide arrays were first predicted by Christodoulides & Joseph (1988). In this study, the primitive band structure of the waveguide array (the first band and Brillouin zone of the system) was recognized and the possibility of observing discrete self-trapped states and discrete modulational instability in Kerr arrays was suggested. In general, discrete solitons in array lattices represent collective excitations of the nonlinear chain as a whole and by their nature they have not analogous whatsoever in continuous systems. The process of optical soliton formation in such array structures can be intuitively understood as a balance between on-site nonlinearity and discrete diffraction effects arising from linear coupling among adjacent waveguides. In this case, the optical energy is nonlinearly confined in a few waveguides and it can propagate undistorted, free of diffraction effects.

From a mathematical point of view, a discrete nonlinear Schrödinger (DNLS) equation is any equation that can be obtained from a NLS equation of general form (1.3) by employing some finite-difference approximation to the operators acting on the continuous field $\psi(\mathbf{r}, z)$. In Eq. (1.3), ∇^2 is the Laplace operator acting in one or two transversal spatial dimensions. By definition, the discrete nonlinear Schrödinger equation denotes a set of coupled ordinary differential equations resulting from discretizing all spatial variables in (1), while keeping the evolution-coordinate z continuous. The simplest example of a DNLS equation can be formally obtained by just replacing the Laplacian operator in (1.3) with the corresponding discrete Laplacian. Thus, for the one-dimensional case we let $\psi_i(z) = \psi(x = ia, z)$ where a is the lattice parameter. Hence for the particular case of cubic nonlinearity, $F(I) = |\psi|^2$, the following equation is obtained:

$$i\dot{\psi}_i + C(\psi_{i+1} + \psi_{i-1} - 2\psi_i) + \gamma|\psi_i|^2\psi_i = 0, \tag{1.5}$$

where $C = 1/a$.

The previous statement is a fairly generous definition for the DNLS equation. Although the model (1.5) is mathematically correct, and its physical predictions are right, we prefer approaching the problem from a physical point of view. The model we follow, has been widely used in the past and it is explained in detail in References (Campbell et al., 2004; Lederer et al., 2008; Flach & Gorbach, 2008). It can be shown that when two waveguides are positioned in close proximity, a linear interaction between them appears due to a coupling through their evanescent fields (tails) in each waveguide.

The idea of discrete optical components emerged rather gradually in the field of optics. This slow pace of development was due to several reasons. To begin with, from a classical perspective, the optical or electromagnetic field itself is a continuous function of both space and time. From a more practical point of view, an important barrier that prevented these thoughts from becoming reality was the state of fabrication technologies, especially in the first few decades after the discovery of the laser. Clearly, discretizing light behavior will require optical elements that can confine the optical energy at distinct sites.

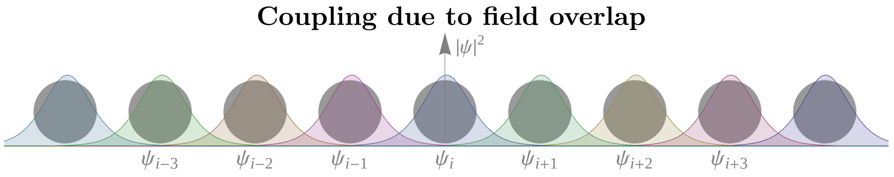

FIGURE 1.5: The sketch drawing of coupling due to field overlap of each waveguide in one-dimensional waveguide arrays.

Figure 1.5 depicts such a periodic waveguide array arrangement. All waveguide elements are identical and equally spaced from each other. Yet, they are close enough so that the modal fields supported by these waveguides overlap, and as a result cross-talking takes place. This kind of phenomena (power exchange process) can be effectively modeled using coupled-mode theory (or the tight-binding approximation). This is possible if the waveguide sites are sufficiently separated. The underlying evolution equation is given by

$$i\dot{\psi}_i + C(\psi_{i+1} + \psi_{i-1}) = 0. \tag{1.6}$$

The second term of Eq. (1.6) is known as the discrete diffraction effect. The behavior of these arrays was first considered by Jones (1965) as a part of a larger effort towards the understanding of optical coupling processes. In simpler terms, discreteness appears as an effect of weakly interacting systems, for example arrays of coupled optical waveguides. Another very important physical example is what is called, in solid-state physics, tight-binding. The interaction between different lattices sites appears as the overlapping of the electronic wave functions, i.e. a linear coupling. Many works have been devoted to analyzing different physical effects in homogeneous and inhomogeneous arrays. Discrete diffraction (Jones, 1965), defect waveguides (Trompeter et al., 2003), Bloch oscillations and Zener tunneling (Zener, 1934) and dynamical localization (Longhi et al., 2006) are some of the most relevant phenomena in the linear regimen.

In Eq. (1.6), ψ_i represents the modal field amplitude in the ith waveguide site, z is the propagation coordinate in space, and C stands for the coupling constant resulting from the field overlap. In fact, if in the model (1.5) we perform the following transformation, $\psi_i(z) \to \psi_i(z)e^{-2iCz}$, we can remove its linear local term $-2C\psi_i$. Thus, the model (1.5) can be rewritten as

$$i\dot{\psi}_i + C(\psi_{i+1} + \psi_{i-1}) + \gamma|\psi_i|^2\psi_i = 0. \tag{1.7}$$

Discrete solitons in nonlinear waveguide arrays were first experimentally observed by Eisenberg et al. (1998) in AlGaAs waveguide arrays similar to the one showed in Fig. 1.6(a). They observed that for lower powers (at 70W) the array behaved linearly and the beam diffracted through the array in agreement with Eq. (1.6). However, at higher peak powers ($\sim 500W$), the energy became

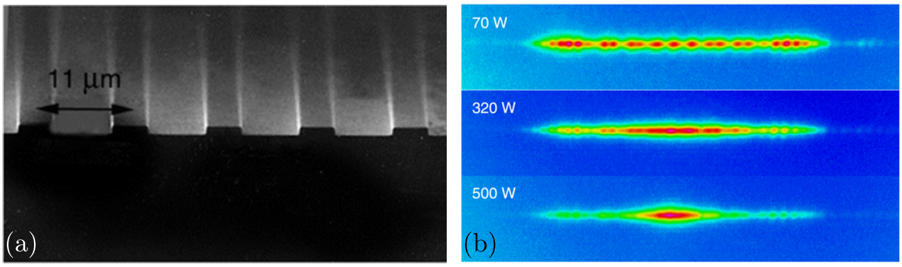

FIGURE 1.6: (a) AlGaAs waveguide array similar to that used for the first (b) experimental observation of discrete optical solitons.

confined in a few waveguide sites, (Fig. 1.6[b]), a clear indication of discrete soliton formation. The light source used for this experiment was an optical parametric oscillator (OPO) pumped by a Ti:sapphire laser, producing 100-200 fs pulses at a 80 MHz repetition rate. The OPO was tuned to a wavelength of 1.53mm, which is below the half-band-gap of the AlGaAs material and where detrimental effects of nonlinear absorption are minimized.

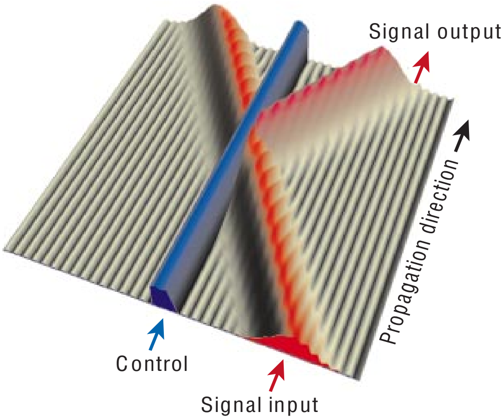

FIGURE 1.7: Schematic all-optical routing of on input signal beam to a specific output position using light interaction in a nonlinear waveguide array.

The steering and trapping of solitons in the framework of model (1.7) have been analyzed some years ago by Vicencio et al. (2003). As it is kicked by an external force, the discrete soliton can propagate through the lattice for some distance, but then it gets trapped as a result of the effect of discreteness. For a larger force, the output soliton position fluctuates between two (or more) neighboring waveguides, making switching uncontrollable. Additionally to this, it is possible to design "architectures" that use light as a signal control to block and change the trajectory of the beam, or signal input (Fig. 1.7).

Since the beginning of the last decade, several experiments were carried out to observe discrete solitons in two-dimensional waveguide arrays. The test bed here is not a two-dimensional extension of the semiconductor configuration used to construct the one dimensional waveguide array. Semiconductor materials such as AlGaAs are highly nonlinear and can be easily etched to form high-quality one-dimensional arrays. However, such etching techniques are by nature epitaxial, making it difficult to fabricate two dimensional arrays.

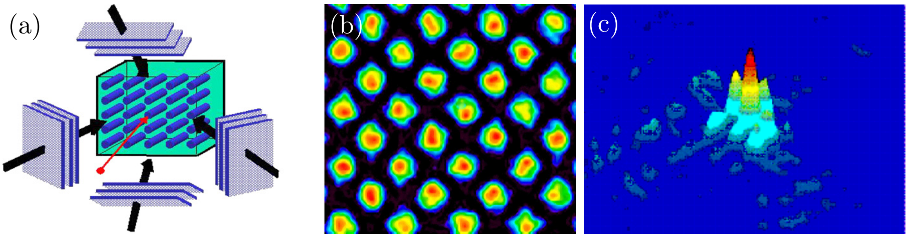

Figure 1.8: Four interfering beams (left) forming an optical lattice structure (center). Two-dimensional discrete soliton experimental observation (right)

The observation of two-dimensional discrete solitons in optical lattices were first reported in biased photorefractive crystals (Fleischer et al., 2003a,b), and it was possible through the optical induction method (Efremidis et al., 2002). Two dimensional optical induced lattices can be created by interfering multiple plane wave beams (Fig. 1.8[a]), launched at the same angle with respect to the propagation axis, inside a crystal with large electrooptic anisotropy. With an appropriate polarization of the plane wave it is possible to generate an optical periodical potential (Fig. 1.8[b]). The bias voltage applied to the photosensitive crystal and the periodical pattern set the desired scenario to observe self localized nonlinear waves (Fig. 1.8[c]).

At the beginning of the last decade, Christodoulides & Eugenieva (2001) showed theoretically that discrete solitons in two-dimensional nonlinear waveguide array networks can provide an attractive test bed for all-optical data processing applications. More specifically, this family of solitons could realize intelligent functional operations such as routing, blocking, logic functions and time-gating. These discrete solitons could be routed anywhere (Fig. 1.9[a]) in the network along pre-assigned array pathways that acted like “soliton wires”. Even more importantly, discrete solitons can be routed at array intersections using vector-incoherent interactions with other ones. In essence, these intersections behave as discrete soliton switching junctions. Such systems can also be used to realize logic operations (Fig. 1.9[b]).

For discrete systems, it is also possible to observe such optical self-trapped vortex structures. By means of the optical induction technique, described above,

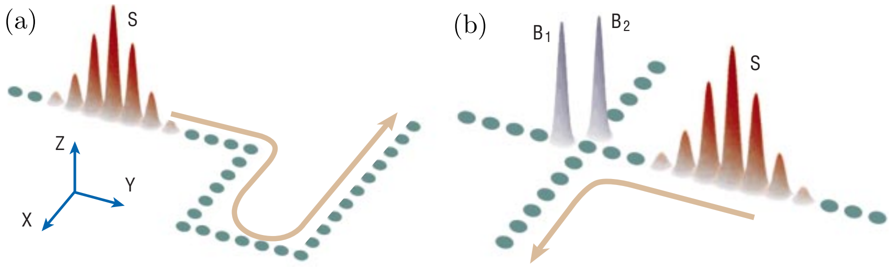

FIGURE 1.9: Possible applications of discrete solitons. A nonlinear array network involving consecutive bends (a). An X-switching junction that uses two different discrete solitons families, the so-called “signals” and “blockers”, denoted by S and B, respectively (b).

it was possible to observe waves carrying angular momentum on nonlinear waveguide arrays, i.e, discrete vortex solitons (Neshev et al., 2004; Fleischer et al., 2004). Both on-site vortices (vortices whose singularity is located on a lattice waveguide site) and off-site vortices (vortices whose singularity is located between lattice sites) were successfully observed in these studies.

1.3 Dissipative Systems

Dissipative systems are commonly understood as those that only have losses, and therefore any solution hopelessly will vanish on propagation. We are interested in a more general system that allows the interchange of energy between the system and its surroundings. Namely, the flow of energy should go in both directions, apart from the losses. The system can be amplified from an external source which allows the existence of stationary solutions with a fixed (nonzero) or periodic energy value.

Let us consider the most favorite exercise in the introductory courses of classical mechanics, the simple pendulum. From this, we can make the following classification. When the amplitude of the oscillations is small, the system can be approximated by a linear oscillator ($\ddot{\varphi} + \omega^2\phi = 0$), Fig. 1.10(a). If we had several coupled oscillators, the general solution could be written as a linear superposition of normal modes. If the amplitude of the oscillations is not small, then the oscillations are nonlinear ($\ddot{\varphi} + \omega^2 \sin\phi = 0$), Fig. 1.10(b). The exact analytic solution for this case does exist and it can be written in terms of elliptic Jacobi functions. However, for a coupled set of equations, the solution can not be written as a linear superposition of modes. Finally, when losses are included ($\ddot{\varphi} + \gamma\dot{\varphi} + \omega^2\phi = F(\varphi, t)$), Fig. 1.10(c), the system becomes dissipative. The oscillations are undamped only if there is an external force pumping energy into the pendulum. For a system of coupled equations, the solution can only be found numerically in most cases.

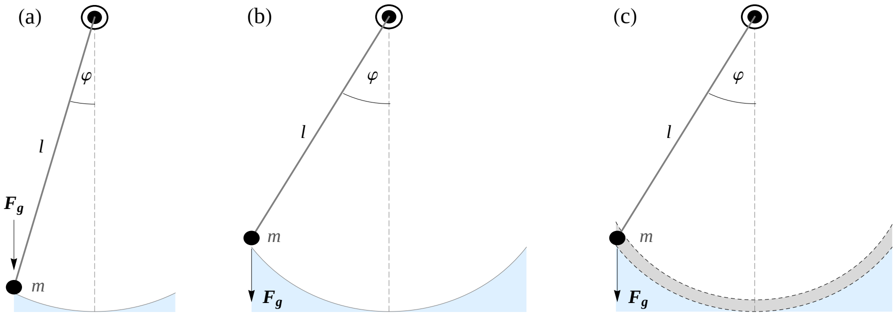

FIGURE 1.10: Dynamical classification for a pendulum system. (a) linear oscillations for small amplitude. (b) nonlinear oscillation for not small amplitude. (c) The pendulum experiments friction and the amplitude is damped.

In the same way that we have classified the solutions of the above example, dissipative systems can be considered as the most general model for dynamical evolution. The complex cubic-quintic Ginzburg-Landau (CQGL) equation is widely-known as a universal model for several dissipative systems in many branches of knowledge, and dissipative solitons are probably their most interesting solutions. For one-dimensional systems, it looks like:

$$i\frac{\partial\psi}{\partial\xi} + \frac{D}{2}\frac{\partial^2\psi}{\partial\eta^2} + |\psi|^2\psi + \nu|\psi|^4\psi = i\delta\psi + i\varepsilon|\psi|^2\psi + i\mu|\psi|^4\psi. \tag{1.8}$$

We emphasize here that Eq. (1.8) is a model accounting for, in a distributed way, each of the effects experimented while the wave is propagating in the system. A lumped description of the mode-locked fiber laser is more accurate, but its model is too involved. In this approach, the light propagates sequentially through the individual elements in the laser, while each of them is described by the proper equations. It is worth to mention here that in a fiber laser model, the variables ξ and η must be replaced with z and t, respectively.

1.3.1 Generalities about Dissipative Solitons

The notion of dissipative solitons (Akhmediev & Ankiewicz, 2005) is a useful concept that allows us to describe, in general terms, a variety of phenomena in physics, chemistry, biology and medicine (Akhmediev & Ankiewicz, 2008). Some specific features of these formations are common for all of them, independent on the problem that we are solving and the model we are using.

The dissipative soliton concept is a fundamental extension of that for solitons in conservative and integrable systems. It includes ideas from three major sources, namely, the standard soliton theory developed since the 1960s, ideas from nonlinear dynamics theory and Prigogine's ideas of systems far from equilibrium and self-organization, Fig. 1.11. These are basically the three sources and three components of this novel paradigm.

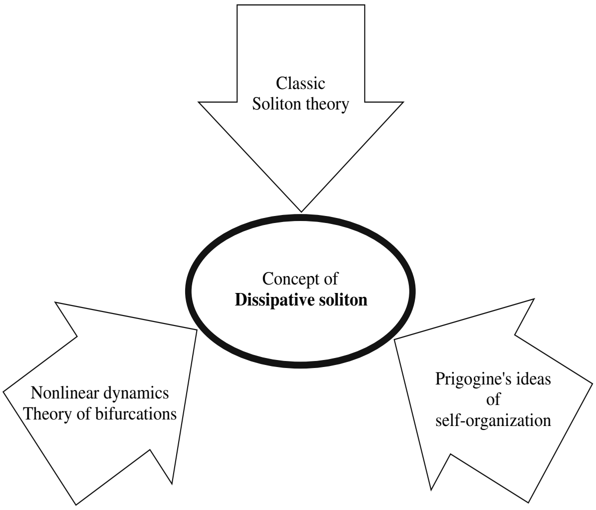

FIGURE 1.11: Three sources and three component parts of the concept of dissipative soliton.

In conservative and integrable (Hamiltonian) systems, the first source, soliton solutions appear as a result of a balance between diffraction (dispersion) and nonlinearity. The balance between the two opposed effects results in stationary solutions, which are usually a one-parameter family. In open systems, in order to have stationary solutions, gain and loss must also be balanced. This situation is illustrated qualitatively in Fig. 1.12, which shows that this additional balance imposes a second constraint, so that, as a result we get solutions which are fixed. The shape, amplitude and the width are all fixed and depend on the parameters in Eq. (3.1). There can be exceptions to this rule, but the solutions are usually fixed, i.e. isolated from each other.

The second part of the foundation, the nonlinear dynamics, establishes the idea of a soliton as a fixed point of an infinite-dimensional dynamical system. Stability properties of fixed points determine the stability of the soliton itself. Fixed points can be transformed into limit cycles at certain values of the system parameters, and then the soliton becomes a pulsating object. Further transformations may include irregular behavior of the trajectory, thus creating chaotic solitons. Therefore, nonlinear dynamics supplies the ideas of soliton bifurcations and the chaotic evolution of solitons.

Finally, the third part of the basis, the theory of systems far from equilibrium, establishes that solitons are self-organized formations requiring a continuous supply of matter or energy. As soon as that supply finishes, a dissipative soliton ceases to exist. In simple terms, self-organization is a convergence of certain initial conditions to a localized solution of the system that is stable for

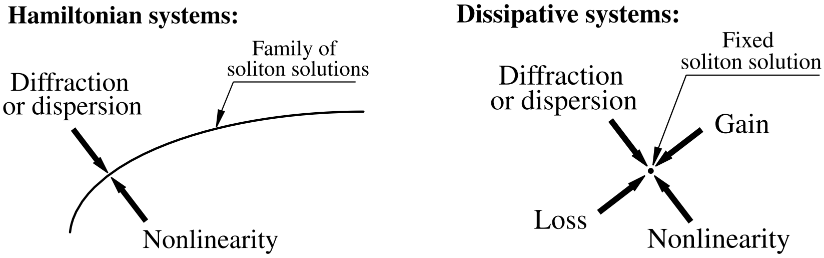

Figure 1.12: Qualitative difference between the soliton solutions in Hamiltonian and dissipative systems. In Hamiltonian systems, soliton solutions are the result of a single balance, and comprise one- or few-parameter families, whereas, in dissipative systems, the soliton solutions are the result of a double balance and, in general, are isolated. On the other hand, it is quite possible for several isolated soliton solutions to exist for the same equation parameters.

a given set of external parameters. Thus, the final state is determined by the physical laws and not by the initial condition. For infinite-dimensional dynamical systems, this stable solution can be very complicated. It is not necessarily a smooth function with a single maximum and exponentially decaying tails. Moreover, there can be several stable solutions existing for the same set of parameters. This can even happen in the case of a relatively simple equation like the complex CQGL equation. The majority of processes in nature are governed by far more complicated dynamical factors. Thus, stationary solutions of these systems can be considerably more involved.

Another simple qualitative picture is presented in Fig. 1.13. In order to be stationary, solitons in dissipative systems need to have regions where they extract energy from an external source, as well as regions where energy is dissipated to the environment. A stationary soliton is the result of a dynamical process of continuous energy exchange with the environment and its redistribution between various parts of the soliton. As soon as this energy redistribution ends, the soliton disappears.

As we have mentioned previously, dissipative systems interacts with the surrounding medium. Having into account that, it is natural to think that its energy is not a conserved quantity during the dynamical evolution. Then, an equilibrium is necessary between the external sources of energy, for the system to reach a stationary solution. This condition can be handled choosing an adequate set of values for the parameters of the complex CQGL equation.

Integrable systems are the result of adopting extreme simplifications of real (dissipative) systems. They can be considered as a subclass of the more general Hamiltonian systems (Akhmediev & Ankiewicz, 1997). In particular, the system is Hamiltonian when we set $\delta = \varepsilon = \beta = \mu = 0$ in Eq. (1.8). The system is integrable, when, in addition, $\nu = 0$. Then it follows that Hamiltonian systems can be considered as a subclass of dissipative ones, while integrable systems can

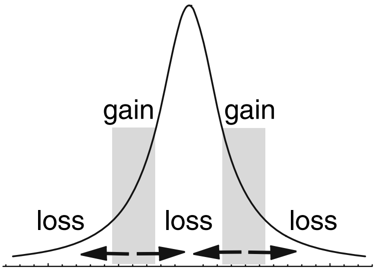

FIGURE 1.13: Qualitative description of solitons in dissipative systems. The soliton has areas of consumption as well as expenditure of energy, and these can be both frequency (spatial or temporal) and intensity dependent. Arrows show the energy flow across the soliton.

be viewed as a subclass of Hamiltonian ones. This classification is illustrated in Fig. 1.14.

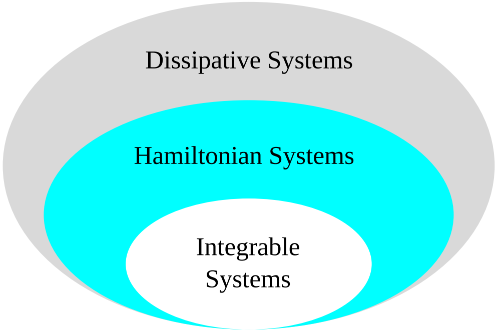

FIGURE 1.14: Diagrammatic classification of nonlinear systems with an infinite number of degrees of freedom admitting soliton solutions.

Solitons in Hamiltonian (but non-integrable) systems can also be regarded as nonlinear modes, but in the sense that they allow us to describe the behavior of systems with an infinite number of degrees of freedom in terms of a few variables, thus allowing us to effectively reduce the number of degrees of freedom. Solitons in these systems collide inelastically and interact with radiation waves, thus showing that they are qualitatively different from those in integrable systems. However, as in the integrable case, the solitons are still a one- (or few-)parameter family of solutions.

Another interesting property of Hamiltonian systems is that there are no pulsating solutions. If the system is near integrable, then the two-soliton solutions of the nonlinear Schrödinger (NLS) equation which are initially excited will gradually split into two solitons or transform into a single soliton solution, depending on the type of the perturbation (Artigas et al., 1997). If the system is far from integrable, pulsations may exist if a single soliton solution is excited with a perturbation; however, they die out, so that the pulse gradually converges to a stationary soliton.

Solving numerically the Eq. (1.8), Soto-Crespo et al. (2000a) found numerically a pulsating soliton with periodic behavior along z being the period around 14 (Fig. 1.15). It has a different shape at each z, since it evolves, but it recovers its exact initial shape after a period.

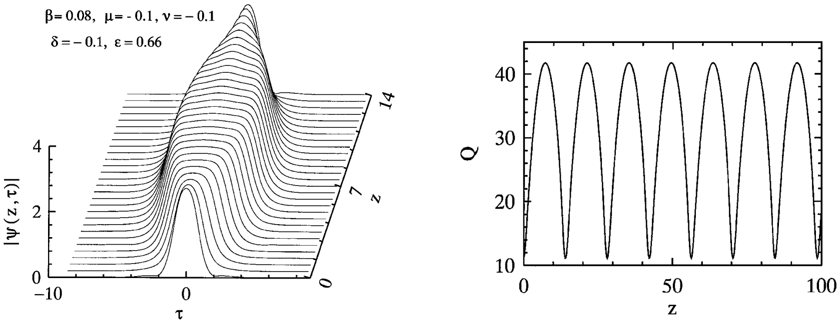

FIGURE 1.15: Plain pulsating soliton of complex CQGL equation.

1.3.2 Spatial optical Dissipative Solitons

Conservative solitons in Kerr media are described by the NLS equation (1.3). This model assumes an infinite nonlinear medium. Real nonlinear optical media have finite dimensions and (except in glass fiber) solitons can rarely propagate more than a few centimeters before running out of the material. To increase the propagation length it is therefore convenient to place mirrors at the ends of the medium, thus confining the soliton into a finite slab of material. With perfect reflection and zero absorption, one could indeed confine a soliton in such a “box”. Real mirrors and materials are lossy, but we can make good the loss by “feeding” the caged soliton with an input field.

The existence of stable two-dimensional spatial solitons in conservative systems is widely outweighs by dissipative ones. The existence of these localized structures in materials with Kerr-type nonlinearity response, in many cases, is limited to one dimensional systems. However, as many researchers demonstrated over the last years, dissipative schemes can support stable soliton solutions with lots of intriguing and new properties. Perhaps, the most appropriate dissipative scenario to find and observe two-dimensional spatial dissipative solitons is a nonlinear optical cavity, hence, some authors usually denominate this kind of structures as *cavity solitons*.

A spatial dissipative solitons is a stable, self-localized optical excitation sitting on a uniform, or quasi-uniform, background, and substantially independent of transverse boundary conditions. A key property is that it can be present or absent under the same external conditions, i.e. it exhibits bistability between "off" and "on" states. Its ground state, usually, is a bright spot of light on some low amplitude background. It is self-localized in the two spatial dimensions transverse to the main propagation axis (e.g. the cavity axis). The decay of energy in the wings is asymptotically exponential.

The introduction of dissipation in discrete systems is due to Peschel et al. (2004) who derived a model of spatially coupled cavities obtained by placing mirrors at the open ends of the waveguides (see Fig. 1.16). The model used to describe this problem is equivalent to the discrete version of Eq. (1.8), and its main differences with the DNLS equation (1.7) are the presence of losses due to the partially transmitting mirrors, as well as a driving field. Hence, the model is not exclusive for coupled cavities, it can be applied to model externally driven defects in photonic crystal fibers.

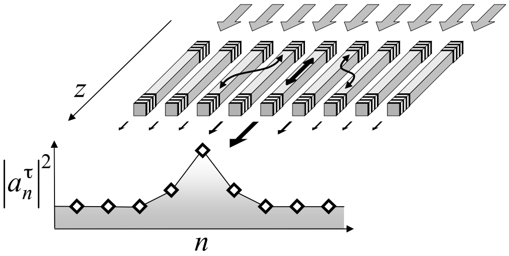

FIGURE 1.16: Coupled cavities formed by a waveguide array with mirrors on each end facet.

As in continuous media, discrete models also exhibit bistability over certain ranges of the parameters related with, losses, gain and coupling. Numerical schemes for the determination and stability of spatial solutions, as those presented in Appendices B and C, can be used to find discrete stable dissipative solitons at generic values of these parameters.

1.4 Overview of the Thesis

The properties and the dynamics of localized structures, define, to a large extent, the behavior of the relevant nonlinear system. Thus, it is a crucial and fundamental issue of nonlinear dynamics to fully characterize these objects in dissipative nonlinear environments. Apart from this fundamental point of view, solitons exhibit a remarkable potential for applications in optical systems. Regarding the type of localization, one can distinguish between temporal and spatial solitons. Optical Solitons in dissipative media presents a rich variety of forms and behaviors. From scalar to vectorial ones, temporal to spatial and spatio-temporal, all of them can be observed in passively mode locked lasers and in optical cavities of wide aperture lasers. The main objective in this dissertation will be to analyze the existence and stability of two-dimensional soliton solutions in dissipative systems, as well as, the identification of regions where these structures exhibit novel transversal dynamics and exotic properties. We have chosen a generic model well known in the dissipative world and it is called the complex CQGL equation. The discrete counterpart of this model is useful to describe the propagation of light into an array of waveguides, for example, propagation of discrete solitons into photonic crystal fibers, as well as, in coupled-waveguide resonators.

We found several types of self-localized light beams in both, continuous and discrete media. Exotic pulsating and rotating 2D solutions in continuous media, besides stable discrete solutions with two topological charges, simultaneously, are the main results reported in this work. Several numerical schemes were implemented to find self-localized families of solutions, as well as, to unveil complex dynamics and interactions between some solitons belonging to them. Additionally, the stability regions were identified by means of linear stability analysis and/or direct numerical simulation of the respective models.

Chapter 2 is devoted to discuss the physical model that we use along this thesis. Starting from Maxwell equations, we present the fundamental equations that governs the propagation of beams in two dimensional media: The NLS equation and its corresponding extension to dissipative systems -the complex CQGL equation. In addition, the tight binding approximation has been applied on these equations to find the corresponding model that describes the propagation of beams in discrete media.

Having in mind the results reported by Soto-Crespo et al. (2000a), we wonder about similar behavior in two dimensional dissipative systems. Chapter 3 is devoted to report and classify a big set of soliton solutions with complex dynamics in two dimensional dissipative systems, which can be continuously focusing or continuously defocusing. Additionally, we unveil several families of vortex solitons with highest values of vorticity. Some of them display several radial and azimutal asymmetries.

Additionally, we also analyze the discrete counterpart of the complex CQGL model. Thus, we have focused in vortex solitons in periodical media under the tight binding approximation. Chapter 4 is devoted to find discrete vortex solitons of the dissipative model. Several families of stable solutions have been classified, some of then having two topological charges simultaneously. Additionally, we analyze the interaction between solutions of these families and their corresponding formation of bound states. It is worth to mention here that our studies and predictions on dissipative discrete optical vortices are the first results reported about this topic.

Finally, Chapter 5 presents a summary of the main results and discusses open prospects.

"Un genio es alguien que descubre que la piedra que cae
y la luna que no cae representan un solo y mismo fenómeno"
Ernesto Sábato - El Túnel

2

Nonlinear Propagation Equations

The main equation governing the evolution of optical fields in a nonlinear isotropic continuous medium is known as the nonlinear Schrödinger equation. In this chapter, starting from the Maxwell equations, we outline the derivation of this equation for a beam propagating inside a nonlinear optical medium with Kerr nonlinearity. Additionally, for discrete media we derive the counterpart version of the nonlinear Schrödinger equation. It has been obtained by means of first principles, analyzing the interaction between the light propagating thorough two waveguides.

2.1 Maxwell Equations

The propagation of optical fields inside an optical medium with Kerr (or cubic) nonlinear response is governed by the macroscopic Maxwell equations. We are primarily interested in the solutions of these equations in regions of space that do not contain free charges, i.e.

$$\rho = 0, \tag{2.1}$$

and that contain no free currents, i.e.

$$\mathbf{J} = 0. \tag{2.2}$$

These equations, write in SI units, take the following form:

$$\nabla \cdot \mathbf{D} = 0, \tag{2.3}$$

$$\nabla \cdot \mathbf{B} = 0, \tag{2.4}$$

$$\nabla \times \mathbf{E} = -\frac{\partial \mathbf{B}}{\partial t}, \tag{2.5}$$

$$\nabla \times \mathbf{H} = \frac{\partial \mathbf{D}}{\partial t}. \tag{2.6}$$

Where **E** and **H** are the electric and magnetic fields, respectively, **D** is called the electric displacement and **B** is the magnetic flux. In order to apply Maxwell's macroscopic equations, it is necessary to specify the relations between the displacement field **D** and **E**, and the magnetic field **H** and **B**. These relations specify the response of bound charge and current to the applied fields and are called constitutive relations; they are:

$$\mathbf{D} = \epsilon_0 \mathbf{E} + \mathbf{P}. \tag{2.7}$$

$$\mathbf{B} = \mu_0 \mathbf{H}. \tag{2.8}$$

where ϵ_0 and μ_0 are the From equations (2.1) to (2.8) it is possible to obtain a general formalism to study wave propagation in waveguides. We take the rotational of Eq. (2.4), interchange the order of space and time derivatives on the right-hand side of the resulting equation, and use Eqs. (2.5) and (2.8), to replace $\nabla \times \mathbf{B}$ by $\mu_0(\partial \mathbf{D}/\partial t)$, to obtain the equation

$$\nabla \times \nabla \times \mathbf{E} + \mu_0 \frac{\partial^2}{\partial t^2} \mathbf{D} = 0. \tag{2.9}$$

We now use Eq. (2.13) to eliminate **D** from this equation, and we thereby obtain the expression

$$\nabla \times \nabla \times \mathbf{E} + \frac{1}{c^2} \frac{\partial^2}{\partial t^2} \mathbf{E} + \frac{1}{\epsilon_0 c^2} \frac{\partial^2 \mathbf{P}}{\partial t^2} = 0, \tag{2.10}$$

with $c = 1/\sqrt{\mu_0 \epsilon_0}$ is the speed of light in vacuum.

From vector analysis we know that $\nabla \times \nabla \times \mathbf{E} = \nabla(\nabla \cdot \mathbf{E}) - \nabla^2 \mathbf{E}$. Because our media has nonlinear response, $\nabla \cdot \mathbf{E} = 0$ is not completely true. However, the first term can often be shown to be small, even when it does not vanish identically, especially when the slowly varying amplitude approximation is valid.

Having in mind the above, and the fact that in our problem electromagnetic waves propagates through isotropic media, we can rewrite Eq. (2.10) as

$$\nabla^2 \mathbf{E} - \frac{1}{c^2} \frac{\partial^2}{\partial t^2} \mathbf{E} - \frac{1}{\epsilon_0 c^2} \frac{\partial^2 \mathbf{P}}{\partial t^2} = 0. \tag{2.11}$$

It is often convenient to split **P** into its linear and nonlinear parts as

$$\mathbf{P}(\mathbf{r}, t) = \mathbf{P}^{\mathbf{L}}(\mathbf{r}, t) + \mathbf{P}^{\mathbf{NL}}(\mathbf{r}, t). \tag{2.12}$$

In the linear regime is necessary that $\mathbf{P^{NL}} = \mathbf{0}$, which allows to write

$$\mathbf{D} = \epsilon_0 \mathbf{E}(\mathbf{r}, t) + \mathbf{P^L}(\mathbf{r}, t) = \epsilon_0 \hat{\boldsymbol{\epsilon}}^L \mathbf{E}(\mathbf{r}, t), \tag{2.13}$$

where $\hat{\boldsymbol{\epsilon}}^L$ is the linear relative dielectric permittivity tensor. If we consider a non dispersive media, Eq. (2.11) is reduced to:

$$\nabla^2 \mathbf{E}(\mathbf{r}, t) - \frac{1}{c^2} \hat{\boldsymbol{\epsilon}}^L \frac{\partial^2}{\partial t^2} \mathbf{E}(\mathbf{r}, t) = 0. \tag{2.14}$$

Linear and nonlinear parts of polarization are related to the electric field by the general relations

$$\mathbf{P^L}(\mathbf{r}, t) = \epsilon_0 \int_{\infty}^{\infty} \chi^{\mathbf{1}}(t - t') \cdot \mathbf{E}(\mathbf{r}, t) \mathrm{d}t', \tag{2.15}$$

$$\begin{aligned} &\mathbf{P^{NL}}(\mathbf{r}, t) = \\ &\epsilon_0 \int_{\infty}^{\infty} \chi^{\mathbf{3}}(t - t_1)(t - t_2)(t - t_3) \mathbf{E}(\mathbf{r}, t_1) \mathbf{E}(\mathbf{r}, t_2) \mathbf{E}(\mathbf{r}, t_3) \mathrm{d}t_1 \mathrm{d}t_2 \mathrm{d}t_3, \end{aligned} \tag{2.16}$$

where $\chi^{\mathbf{1}}$ and $\chi^{\mathbf{3}}$ are the first- and third-order susceptibility tensors. These relations are valid in the electric-dipole approximation under the assumption that the medium response is local. We also neglect the second-order nonlinear effects, assuming that the medium has an inversion symmetry.

Assuming that the nonlinear response is instantaneous, the time dependence in Eq. (2.17) is given by the product of three delta functions of the form $\delta(t - t_i)$, thus this equation is reduced to

$$\mathbf{P^{NL}}(\mathbf{r}, t) = \epsilon_0 \chi^{\mathbf{3}} \mathbf{E}(\mathbf{r}, t) \mathbf{E}(\mathbf{r}, t) \mathbf{E}(\mathbf{r}, t). \tag{2.17}$$

The last expression can be simplified even further if the optical field maintain its polarization along the propagation, so a scalar approach can be used. Besides, the optical field is assumed to be quasi-monochromatic. When the envelope of the wave varies slowly in time and space compared to a period or wavelength, we can apply the slowly varying envelope approximation. Hence, it is useful to separate the rapidly varying part of the electric field by writing it in the form

$$\mathbf{E}(\mathbf{r}, t) = \frac{1}{2}[E(\mathbf{r}, t) \exp(-i\omega_0 t) + \text{c.c}]\hat{x}, \tag{2.18}$$

where ω_0 is the carrier frequency, $\hat{x}$ is the polarization unit vector, and $E(\mathbf{r}, t)$, is a slowly varying function of time (relative to the optical period). The polarization components $\mathbf{P}_L$ and $\mathbf{P}_{NL}$ can also be expressed in a similar way.

When Eq. (2.18) is substituted in Eq. (2.17), $\mathbf{P}_L(\mathbf{r}, t)$, is found to have a term oscillating at ω_0 and another term oscillating at the third-harmonic frequency,

$3\omega_0$. The latter term requires phase matching and is generally negligible. The slowly varying part $\mathbf{P}_{NL}(\mathbf{r}, t)$ of the nonlinear polarization is then given by

$$\mathbf{P}_{\mathbf{NL}}(\mathbf{r}, t) \approx \epsilon_0 \epsilon_{NL} E(\mathbf{r}, t), \tag{2.19}$$

where the nonlinear contribution to the dielectric constant is defined as

$$\epsilon_{NL} = \frac{3}{4}\chi^3_{xxxx} I, \qquad\qquad I = |E|^2. \tag{2.20}$$

The linear part of the polarization can be written from Eq. (2.15) as

$$P_L = \epsilon_0 \chi^1_{xx} E. \tag{2.21}$$

In fact, the linear and nonlinear parts can be combined to provide the following expression for the dielectric constant

$$\tilde{\epsilon}(\omega) = 1 + \chi^1_{xx}(\omega) + \epsilon_{NL}, \tag{2.22}$$

where a tilde denotes the Fourier transform of the quantity under it. The dielectric constant can be used to define the refractive index $\tilde{n}$ and the absorption coefficient $\tilde{\alpha}$. However, both $\tilde{n}$ and $\tilde{\alpha}$ become intensity dependent because of ϵ_{NL}. It is customary to introduce

$$\tilde{n} = n_0 + n_2 I, \tag{2.23}$$

$$\tilde{\alpha} = \alpha + \alpha_2 I. \tag{2.24}$$

The linear index n_0 and the absorption coefficient α are related to the real and imaginary parts of χ^1_{xx}. Using

$$\epsilon = (\tilde{n} + i\tilde{\alpha}c/2\omega_0)^2 \tag{2.25}$$

and Eqs. (2.20) and (2.22), the nonlinear, or Kerr, coefficient n_2 and the two-photon absorption coefficient α_2 are given by

$$n_2 = \frac{3}{8n}\mathbb{R}(\chi^3_{xxxx}), \qquad\qquad \alpha_2 = \frac{3\omega_0}{4nc}\mathbb{I}(\chi^3_{xxxx}), \tag{2.26}$$

where $\mathbb{R}$ and $\mathbb{I}$ stand for the real and imaginary parts, respectively.

2.2 Spatial Nonlinear Schrödinger Equation

Light beams with some limited spatial extent in the transversal direction can form a lensing effect when they propagates inside an optical Kerr media. The power of focusing/defocusing varies according to the spatial intensity distribution of the beam. In other words, the refractive index of the material varies as required by Eq. (2.23). This relation is know as the optical Kerr effect.

Depending on the sign of the coefficient n_2 (the "nonlinear refractive index"), the beam will either experience a defocusing lensing effect (if $n_2 < 0$) or a focusing lensing effect (if $n_2 > 0$); in the latter case the beam itself will create a self-induced waveguide in the medium, see Fig. 1.2(a).

In the electromagnetic wave picture, the propagation of an optical continuous wave in optical Kerr-media is governed by the wave equation (2.11). By introducing the reduced expressions previously obtained for the linear and nonlinear polarizations, and considering that the spatial part of the electrical field can be written as

$$E(\mathrm{R}) = A(\mathrm{X},\mathrm{Y})\exp(i\beta_0 \mathrm{Z}), \tag{2.27}$$

where $\beta_0 = k_0 n_0 = 2\pi n_0/\lambda$ is the propagation constant in terms of the optical wavelength $\lambda = 2\pi c/\omega_0$, the wave equation (2.11) takes the form

$$2i\beta_0 \frac{\partial A}{\partial \mathrm{Z}} + \left(\frac{\partial^2 A}{\partial \mathrm{X}^2} + \frac{\partial^2 A}{\partial \mathrm{Y}^2}\right) + 2\beta_0 k_0 n_2 I A = 0, \tag{2.28}$$

in which the second derivative respect to Z has been neglected, due to the envelope A is assumed to vary with Z on a scale much longer than the wavelength λ (the paraxial approximation), i.e.

$$\left|\frac{\partial^2 A}{\partial z^2}\right| \ll \left|\frac{\partial A}{\partial z}\right|. \tag{2.29}$$

It is useful to introduce the scaled dimensionless variables as

$$x = \mathrm{X}/w_0, \quad y = \mathrm{Y}/w_0, \quad z = \mathrm{Z}/L_d, \quad \psi = (k_0|n_2|L_d)^{1/2}A, \tag{2.30}$$

where w_0 is a transverse scaling parameter related to the input beam width and $L_d = \beta_0 w_0^2$ is the diffraction length (also called the Rayleigh range). In terms of these dimensionless variables, Eq. (2.28) takes the form of a standard $(2+1)$-dimensional nonlinear Schrödinger equation:

$$i\frac{\partial \psi}{\partial z} + \frac{1}{2}\left(\frac{\partial^2 \psi}{\partial x^2} + \frac{\partial^2 \psi}{\partial y^2}\right) \pm \gamma|\psi|^2\psi = 0, \tag{2.31}$$

where the choice of the sign depends on the sign of the nonlinear parameter $\gamma \propto n_2$; the minus sign is chosen in the self-defocusing case ($n_2 < 0$). This equation is referred to as being $(2+1)$-dimensional, where 2 corresponds to the number of the transverse dimensions in the nonlinear Schrödinger equation equation and $+1$ indicates the propagation direction z.

The standard NLS equation has the time variable t in place of z because it has its origin in quantum mechanics. Of course, one can use $\mathrm{Z} = (c/n_0)t$ and write the NLS equation in terms of t. However, it is common in optics to use z as the evolution variable. The normalized NLS equation, Eq. (2.31), has no free parameters, and even the factor $1/2$ can be removed by renormalizing x and y, as is often done in the soliton literature.

If the optical field is confined in one of its transversal coordinates the Laplace operator in Eq. (2.28) is reduced to $\nabla^2 = \partial^2/\partial x^2$, thus the normalized NLS equation (2.31) is referred to as being $(1+1)$-dimensional and constitutes the simplest form of the NLS equation, which can be solved exactly using the inverse scattering method (Zakharov & Shabat, 1974) for both signs of the nonlinear term. The bright and dark spatial solitons solutions of the NLS equation correspond to the choice of $+$ and $-$ signs, respectively. The problem is that the inverse scattering method, useful finding analytically stable soliton solutions in one dimension, is not applicable to the $(2+1)$ NLS equation.

All localized solutions obtained analytically through some simplification either spread out with propagation for input powers less than a critical value or collapse at a finite distance for powers above the critical value. Even the radially symmetric solution at the critical power is unstable. By means of numerical simulations, Towers & Malomed (2002) suggested that the Eq. (2.31) with distributed coefficients, $\gamma(z)$, may lead to stable 2D solitons. The stabilizing mechanism was the sign-alternating Kerr nonlinearity in a layered medium.

A numerical approach is therefore often necessary for an understanding of the nonlinear effects in bulk media. A large number of numerical methods can be used for this purpose. Mainly, pseudospectral methods such as the split-step Fourier method has been used extensively to solve the beam/pulse propagation problem in nonlinear disperssive/difractive media. This spectral method has been employed to find all the solutions, concerning to systems in continuous media, reported in this thesis.

2.2.1 Lagrangian Formulation of NLS Equation

We can write the NLS equation in its canonical form as

$$i\psi_z + \Delta\psi + F(|\psi|^2)\psi = 0. \tag{2.32}$$

Considering ψ and ψ^* as independent variables, the associated Lagrangian density of Eq. (2.32) can be written in the form

$$\mathcal{L} = \frac{i}{2}(\psi^*\psi_z - (\psi\psi_z^*) - \nabla\psi\cdot\nabla\psi^* + F(|\psi|^2)\psi, \tag{2.33}$$

where ψ_z corresponds to its first derivative with respect to the propagation coordinate z, the asterisk denotes complex conjugate and $F(\lambda)$ stands for the integral

$$F(\lambda) = \int_0^\lambda \mathrm{d}\,\lambda. \tag{2.34}$$

Defining the action S as the integral of the Lagrangian density $\mathcal{L}$ over $\mathbb{R}^2$ and between z_0 and z_1

$$S(\psi,\psi^*) = \int_{z0}^{z1}\int_{\mathbb{R}^2}\mathcal{L}\,\mathrm{d}\,\mathbf{r}\,\mathrm{d}\,z, \tag{2.35}$$

then the variation $\delta S = S(\psi + \delta\psi, \psi^* + \delta\psi*) - S(\psi, \psi^*)$ for infinitesimal ψ and ψ^* is given by the following expression

$$\delta S = \int_{z0}^{z1} \int_{\mathbb{R}^2} \left[\frac{\partial \mathcal{L}}{\partial \psi} - \nabla \cdot \left(\frac{\partial \mathcal{L}}{\partial \nabla \psi} \right) - \partial_z \left(\frac{\partial \mathcal{L}}{\partial \psi_z} \right) \right] \mathrm{d}\, \psi \, \mathrm{d}\, \mathbf{r} \, \mathrm{d}\, z + \left[\frac{\partial \mathcal{L}}{\partial \psi_z} \right]_{z_0}^{z_1} + \text{c.c.} \tag{2.36}$$

The action S attains an extrema ($\delta S = 0$) for functions ψ which fulfill the Euler Lagrange equations

$$\frac{\partial \mathcal{L}}{\partial \psi} = \nabla \cdot \left(\frac{\partial \mathcal{L}}{\partial \nabla \psi} \right) + \partial_z \left(\frac{\mathcal{L}}{\partial \psi_z} \right). \tag{2.37}$$

If the Lagrangian density (2.33) is inserted into the Euler-Lagrange equations, then the NLS equation (2.32) is recovered.

2.3 The 2D Complex CQGL Equation

Previously, in Section 1.3.1 we mentioned that a conservative system can be understood as limit case of more general (complex) system. In fact, those phenomena that are accounted in the complex system, can be considered as small perturbations to the conservative one. For example, the nonlinear refractive index (Eq. 2.23) was obtained through an expansion up to third-order terms of the nonlinear polarization. If we consider higher order terms in this expansion, the nonlinear dependence of the refractive index will be modified, i.e. the Kerr effect, related with cubic nonlinearity, must be extended.

The complex CQGL equation derives its character not only from an extension of the widely used cubic Kerr nonlinearity to include a quintic contribution, but also from the inclusion of complex coefficients that model loss and gain. The action taken to broaden the scope of the nonlinearity is a step towards acknowledging that the nonlinearity of many materials saturate, as the propagating power increases. The generalization to complex coefficients permits the modeling of gain and losses, both of a linear and a nonlinear origin.

Let us consider a monochromatic wave of frequency ω and propagation constant k_0, propagating along z axis. Having into account, Eq. (2.40) can be written as

$$\nabla^2 \tilde{\mathbf{E}}(\mathbf{r}, \omega) + \frac{\omega^2}{c^2} \hat{\boldsymbol{\epsilon}}^L \tilde{\mathbf{E}}(\mathbf{r}, \omega) = 0, \tag{2.38}$$

where

$$\tilde{\mathbf{E}}(\mathbf{r}, \omega) = \int_{-\infty}^{\infty} \mathbf{E}(\mathbf{r}, t) \exp{(i\omega t)} \, \mathrm{d}\, t. \tag{2.39}$$

Optical beams can diffract but this tendency is, broadly speaking, offset by the ability of the material nonlinearity to self-focus the beams. A scalar electric field amplitude, $E(x,y,z,\omega)$, associated with the beam that propagates in a isotropic media satisfies the standard wave equation

$$\frac{\partial^2 E(\mathbf{r},\omega)}{\partial z^2} + \nabla_\perp^2 E(\mathbf{r},\omega) + \frac{\omega^2}{c^2}[\epsilon^L(\omega) + \Delta\epsilon(\omega)]E(\mathbf{r},\omega) = 0, \tag{2.40}$$

where $\nabla_\perp^2$ is the transversal Laplace operator, and $\Delta\epsilon(\omega)$ is a small correction accounting for nonlinear response of the media.

The spatial dependence of E can be written as

$$\psi(x,y,z)e^{ik_0 z}, \qquad k_0 = \frac{\omega}{c}\sqrt{\epsilon^L} = \frac{\omega}{c}n_0.$$

The complex amplitude, $\psi(x,y,z)$, is actually slowly varying, thus the paraxial approximation, Eq. (2.29), can be applied. The appropriate form of the wave equation is, therefore,

$$2ik_0\frac{\partial\psi}{\partial z} + \nabla_\perp^2\psi + \frac{\omega^2}{c^2}\Delta\epsilon(\omega)\psi = 0. \tag{2.41}$$

From Eq. (2.25), and considering a non absorbing media, we can express the dielectric permittivity as $\epsilon = n^2$, then $\Delta\epsilon = 2n_0\Delta n$. But, $\Delta n = n - n_0 = n_2|\psi|^2$, therefore the third term in Eq. (2.41) is $2\frac{\omega^2}{c^2}n_0 n_2|\psi|^2\psi$. Finally, rewriting this in terms of k_0, we obtain

$$2ik_0\frac{\partial\psi}{\partial z} + \nabla_\perp^2\psi + \frac{k_0^2}{n_0}n_2|\psi|^2\psi = 0. \tag{2.42}$$

Nonlinear models discussed in the section 2.2 correspond to the lowest order nonlinearities available, namely up to the first two nonlinear terms in expansion of optical medium polarization $P = \chi^{(1)}\psi + \chi^{(2)}\psi^2 + \chi^{(3)}\psi^3 + \ldots$. For the centro-symmetric media all even terms vanish and taking into account higher-order terms one can represent the refractive index as a power-law Kerr-type nonlinearity, $n = n_0 + n_2|\psi|^2 + n_4|\psi|^4 + \ldots$. Thus, Eq. (2.42) can be generalized as

$$2ik_0\frac{\partial\psi}{\partial z} + \nabla_\perp^2\psi + \frac{k_0^2}{n_0}n_2|\psi|^2\psi + \frac{k_0^2}{n_0}n_4|\psi|^4\psi = 0. \tag{2.43}$$

If nonlinear coefficients n_2 and n_4 have the same signs, corresponding models exhibit simple increasing of strength of nonlinear self-action, self-focusing for $n_{2,4} > 0$ or self-defocusing for $n_{2,4} < 0$. Let n_4 be of self-focusing type, $n_4 > 0$. Then, for any sign of Kerr contribution n_2, there will be a maximum intensity of light beam, when higher-order self-focusing will predominate both the linear diffraction and n_2 contribution. In this case the beam will collapse, similar to the pure Kerr case with $n_2 > 0$ and $n_4 = 0$. However, if $n_4 < 0$, than the collapse can be stopped, because the parts of light beam with high enough intensity $I > I_{max}$ experience effectively self-defocusing environment, $dn/dI < 0$. Here the threshold intensity is given by $I_{max} = -n_2/(2n_4)$. Furthermore, the cubic-quintic nonlinearity can be regarded as a power-law expansion for any collapse-free nonlinearity with saturation, for example the phenomenological one mentioned in section 1.2.2, $n = n_0 + n_2 I/(1 + sI)$. In this case $n_4 = -sn_2$, and the CQ medium is refereed also as a saturable one.

Equation (2.43) can be usefully scaled by measuring x and y in the units D_0, equal to the beam width, and z in Rayleigh, or diffraction, lengths $2k_0 D_0^2$. The transformations to the now dimensionless coordinates and the admission of complex coefficients results in the generation of the familiar cubic-quintic equation

$$\begin{aligned} i\frac{\partial\psi}{\partial z} + \frac{1}{2}\nabla_\perp^2\psi + |\psi|^2\psi + \nu|\psi|^4\psi = \\ i\delta\psi + i\varepsilon|\psi|^2\psi + i\beta\nabla_\perp^2\psi + i\mu|\psi|^4\psi. \end{aligned} \tag{2.44}$$

The physical interpretation of Eq. (2.44) leads to the conclusion that δ accounts for any linear absorption, β represents diffusion, ε is the nonlinear cubic gain, ν is the quintic coefficient that measures the self-defocusing brought on by the negative sign in the last term, and μ is a nonlinear loss term, of quintic origin.

2.4 Nonlinear Discrete Propagation Equation

As it was mentioned in Section 1.2.4, the behavior of waves propagating in discrete nonlinear optical systems is known to exhibit features that are otherwise impossible in the continuous (bulk) regime. In solid-state physics, the tight-binding approximation establishes that the interaction between different lattices sites appears as a result of the overlapping of the electronic wave functions, i.e. is a linear coupling. Discreteness appears as an effect of weakly interacting systems, like for example arrays of coupled optical waveguides.

2.4.1 Tight Binding Approximation

It can be shown that when two waveguides are positioned in close proximity, a linear interaction between them appears due to an evanescent coupling of fields in each waveguide. This interesting process was first observed in GaAs waveguide arrays, (Somekh et al., 1973). Yet, at that time, it was not clear, how one could either take advantage of this rather unusual discrete diffraction effect (see Fig. 2.1), and as a result the field remained latent for several years.

Equation (1.7) can be derived if we use Eq. (2.11) to describe the propagation of an optical wave through a waveguide array. When each waveguide of the periodic structure supports a single mode that weakly overlaps with the modes of the two neighboring waveguides, the modes are only weakly coupled via a small change of the refractive index in the waveguides.

Our derivation of Eq. (1.7) starts labeling, with the indices ν and μ, the electrical field. The first one denotes in which waveguide the field is propagating

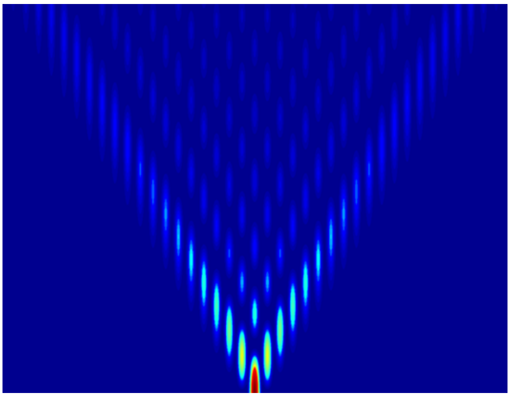

FIGURE 2.1: Discrete diffraction as function of propagation distance.

(ν), and the last one stands what waveguides are coupling with it (μ), hence we write the electrical field as

$$\mathbf{E}_{\mu}^{\nu}(\vec{r},t) = \frac{1}{2}\sum_{j}\left[\vec{f}_{\mu_j}^{\nu}(x,y)\exp\left[i(k_j z - \omega_j t)\right] + c.c\right], \tag{2.45}$$

therefore, Eq. (2.11) can be written as

$$\nabla^2\mathbf{E}_{\mu}^{\nu} - \frac{1}{c^2}\frac{\partial^2\mathbf{E}_{\mu}^{\nu}}{\partial t^2} - \frac{1}{\epsilon_0 c^2}\frac{\partial^2\mathbf{P}_{\mu}^{\nu}}{\partial t^2} = 0, \tag{2.46}$$

Having in mind this spatio-temporal field structure, the three dimensional laplacian and time derivatives can be expressed as

$$\nabla^2 \to \nabla_{\perp}^2 - k^2, \qquad\qquad \frac{\partial}{\partial t} \to -i\omega. \tag{2.47}$$

Thus, if $\mathbf{P} = 0$ the Eq. (2.46) reduces to

$$\frac{1}{2}\sum_{j}\left[\left(\nabla_{\perp}^2 - k_j^2 + \frac{\omega^2}{c^2}\right)\vec{f}_{\mu_j}^{\nu}(x,y)\exp\left[i(k_j z - \omega_j t)\right] + \mathrm{c.c}\right] = 0 \tag{2.48}$$

If the amplitude of $\mathbf{E}_{\mu}^{\nu}(\vec{r},t)$ varies slowly along z, the structure of the electrical field can be expressed as

$$\mathbf{E}_{\mu}^{\nu}(\vec{r},t) = \frac{1}{2}\sum_{j}\left[\vec{f}_{\mu_j}^{\nu}(x,y)a_{\mu_j}^{\nu}(z)\exp\left(-i\omega_j t\right) + \mathrm{c.c}\right] \tag{2.49}$$

Introducing the above expression in the Eq. (2.46) we obtain

$$\frac{1}{2}\sum_j \Bigg[a^{\nu}_{\mu_j}(z)\Big(\nabla^2_{\perp} - k^2 + \frac{\omega^2}{c^2}\Big) + \\ \Big(\frac{\partial^2 a^{\nu}_{\mu_j}}{\partial z^2} + 2ik_j\frac{\partial a^{\nu}_{\mu_j}}{\partial z}\Big)\Bigg]\vec{f}^{\nu}_{\mu_j} e^{i(k_j z-\omega_j t)} + \text{c.c.} \tag{2.50}$$

Here we assume that the amplitude varies slowly along the axis of propagation, i.e,

$$\left|\frac{\partial^2 a^{\nu}_{\mu_j}}{\partial z^2}\right| \ll \left|\frac{\partial a^{\nu}_{\mu_j}}{\partial z}\right|. \tag{2.51}$$

From the Eq. (2.48) we know that $(\nabla^2_{\perp} - k^2_j + \frac{\omega^2}{c^2})\vec{f}^{\nu}_{\mu_j}(x,y) = 0$. Thus, Eq. (2.46) reduces to

$$\frac{1}{2}\sum_j \left[2ik_j\frac{\partial a^{\nu}_{\mu_j}}{\partial z}\vec{f}^{\nu}_{\mu_j} e^{i(k_j z-\omega_j t)} + \text{c.c}\right] = 0. \tag{2.52}$$

Now, we consider the case when $\mathbf{P} \neq 0$. We can write the polarization as the sum of linear and nonlinear contributions, $\mathbf{P}^{\nu}_{\mu}(\vec{r},t) = \mathbf{P^{L}}^{\nu}{}_{\mu} + \mathbf{P^{NL}}^{\nu}{}_{\mu}$. The linear polarization can be written as

$$\mathbf{P^{L}}^{\nu}{}_{\mu} = \varepsilon_0 \chi^{(1)\nu}_{\mu_j} E^{\nu}_{\mu_j}(\vec{r},t) = \frac{1}{2}\varepsilon\chi^{(1)\nu}_{\mu_j}\left(\vec{f}^{\nu}_{\mu_j} a^{\nu}_{\mu_j} e^{i(k_j z-\omega_j t)} + \text{c.c}\right). \tag{2.53}$$

Replacing this in the Eq. (2.46) we obtain the master equation

$$\frac{1}{2}\sum_j \left[2ik_j\vec{f}^{\nu}_{\mu_j}\frac{\partial a^{\mu}_{\nu_j}}{\partial z} + \frac{\omega_j^2}{c^2}\chi^{(1)\nu}_{\mu_j}\vec{f}^{\nu}_{\mu_j} a^{\nu}_{\mu_j} e^{i(k_j z-\omega_j t)} + \text{c.c}\right] = \\ \frac{1}{\varepsilon_0 c^2}\frac{\partial^2}{\partial z^2}\sum_j \mathbf{P^{NL}}^{\nu}{}_{\mu_j}(\vec{r},t). \tag{2.54}$$

2.5 Discrete Nonlinear Schrödinger Equation

As it was mentioned before, the Eq. (1.7) can be obtained by means of physical reasoning. Here, we assume that our material is centrosymmetric and it has a cubic order nonlinear response (Kerr). The term centrosymmetric, as generally used in crystallography, refers to a point group which contains an inversion center as one of its symmetry elements.

We consider here light propagating with a single mode ($j = 1$) of frequency $\omega_1 = \omega$ and $k_1 = k = k(\omega) = n(\omega)k_0$ propagation constant. Additionally, the light is polarized along $\hat{x}$ direction. Thus, the electrical field reduces to $E^{\nu}_{\mu} = \frac{1}{2}[\vec{f}^{\nu}_{\mu} a^{\nu}_{\mu} e^{i(kz-\omega t)} + c.c]$, and the nonlinear polarization becomes

$$\mathbf{P^{NL}}^{\nu}{}_{\mu} = \varepsilon_0\chi^{(3)\nu}_{\mu}(\omega)|E^{\nu}_{\mu}|^2 E^{\nu}_{\mu} = \tfrac{1}{8}[3\chi^{(3)\nu}_{\mu}|\vec{f}^{\nu}_{\mu}|^2|a^{\nu}_{\mu}|^2\vec{f}^{\nu}_{\mu} a^{\nu}_{\mu} e^{i(kz-\omega t)} \\ + \chi^{(3)\nu}_{\mu}(3\omega)(\vec{f}^{\nu}_{\mu})^3(a^{\nu}_{\mu})^3 e^{3i(kz-\omega t)} + \text{c.c}]. \tag{2.55}$$

Replacing this nonlinear polarization in Eq. (2.54) and neglecting the terms with incoherent light ($\neq \omega$), a straightforward calculation leads to:

$$2ik\vec{f}^{\nu}_{\mu}\frac{\partial a^{\nu}_{\mu}}{\partial z} + \frac{\omega^2}{c^2}\chi^{(1)\nu}_{\mu}\vec{f}^{\nu}_{\mu}a^{\nu}_{\mu} = \frac{-3\omega^2}{8c^2}\chi^{(3)\nu}_{\mu}|\vec{f}^{\nu}_{\mu}|^2|a^{\nu}_{\mu}|^2\vec{f}^{\nu}_{\mu}a^{\nu}_{\mu}. \tag{2.56}$$

Considering a system with only two waveguide and following the original assumption of weakly interacting (linear coupling) waveguides, we can write the evolution equation of the light traveling in one of them. For example, for the waveguide number one ($\nu = 1$)

$$2ik\vec{f}^{1}_{1}\frac{\partial a^{1}_{1}}{\partial z} + \frac{\omega^2}{c^2}\chi^{(1)1}_{1}(\vec{f}^{1}_{1}a^{1}_{1} + \vec{f}^{1}_{2}a^{1}_{2}) = \frac{-3\omega^2}{8c^2}\chi^{(3)1}_{1}|\vec{f}^{1}_{1}|^2|a^{1}_{1}|^2\vec{f}^{1}_{1}a^{1}_{1}. \tag{2.57}$$

Multiplying the previous equation by $\vec{f}^{1*}_{1}$ and integrate over the transverse profile of the mode, we can identify some terms which we define as

$$P_\omega \equiv \iint\limits_{Arr} |\vec{f}^{1}_{1}|^2 \,\mathrm{d}\,x\,\mathrm{d}\,y, \qquad V_\omega \equiv \frac{1}{P_\omega}\iint\limits_{Arr} \vec{f}^{1}_{2}\vec{f}^{1}_{1}\,\mathrm{d}\,x\,\mathrm{d}\,y,$$

$$\Phi_\omega \equiv \frac{1}{P_\omega}\iint\limits_{Arr} |\vec{f}^{1}_{1}|^4 \,\mathrm{d}\,x\,\mathrm{d}\,y. \tag{2.58}$$

The quantity V_ω takes values between zero and one ($[0,1]$). If the modes do not interact, $V_\omega = 0$. On the other hand, if these completely overlaps, $V_\omega = 1$. Now, we define some useful quantities:

$$C_a \equiv \frac{\omega^2}{2kc^2}\chi^{(1)}(\omega) \qquad \text{Propagation Coefficient}$$

$$V_a \equiv \frac{\omega^2}{2kc^2}\chi^{(1)}(\omega)V_\omega \qquad \text{Strength Linear Coupling}$$

$$\gamma \equiv \frac{3\omega^2}{16kc^2}\chi^{(3)}(\omega)\Phi_\omega = \frac{\omega n}{2c}n_2\Phi_\omega \qquad \text{Nonlinear Coefficient}$$

If the beam is propagating in an optical array with identical waveguides we can simplify the index notation in Eq. (2.57), namely, $a^1_1 = a_1$, $a^2_2 = a_2$, $V_a a^1_2 = V_a a_2$ and $V_a a^2_1 = V_a a_1$. With this in mind and using the above definitions we can write the evolution equations for the array composed of two waveguides

$$i\frac{da_1}{dz} + c_a a_1 + V_a a_2 + \gamma|a_1|^2 a_1 = 0,$$

$$i\frac{da_2}{dz} + c_a a_2 + V_a a_1 + \gamma|a_2|^2 a_2 = 0. \tag{2.59}$$

Arguing in a similar way we can extend the same reasoning to arrays with N waveguides, which leads to the following set of coupled ordinary differential equations

$$i\frac{da_n}{dz} + c_a a_n + V_a(a_{n-1} + a_{n+1}) + \gamma|a_n|^2 a_n = 0. \tag{2.60}$$

Performing the following transformation

$$a_n(z) \rightarrow \sqrt{\frac{2n}{P_\omega}} A_n e^{iC_a z}(z),$$

we can remove the local interaction term and rewrite Eq. (2.60) as

$$i\frac{dA_n}{dz} + V_a(A_{n-1} + A_{n+1}) + \gamma_{eff}|A_n|^2 A_n = 0, \tag{2.61}$$

where

$$\gamma_{eff} = \frac{\omega n^2 n_2}{cA_{eff}}, \qquad \text{with,} \qquad A_{eff} = \frac{P_\omega}{\Phi_\omega}.$$

Again, we can make some substitutions with the aim of writing the last equation in its dimensionless form. For that, we normalize the amplitude of the mode to the initial peak amplitude of the beam, $A_n = A_p\psi_n$, and additionally divide by L_0 (the characteristic length of the system) the evolution coordinate z. Thus, we arrive finally to the following coupled set of equations:

$$i\frac{d\psi_n}{dz} + C(\psi_{n-1} + \psi_{n+1}) + \gamma|\psi_n|^2\psi_n = 0. \tag{2.62}$$

Equation (2.62) is the well known Discrete Nonlinear Schödinger (DNLS) equation. It is worth pointing out, to avoid confusion, that a lot of works follow the model based in Eq. (2.60), but as we saw previously both of them are equivalent, therefore the predictions gives are equivalent.

The connection with the continuous Nonlinear Schrödinger equation

$$i\psi_z + \psi_{xx} + \gamma|\psi|^2\psi = 0 \tag{2.63}$$

is more clear if we write Eq. (2.62) in an alternative form

$$i\frac{d\psi_n}{dz} + C(\psi_{n+1} - 2\psi_n + \psi_{n-1}) + \gamma|\psi_n|^2\psi_n = 0. \tag{2.64}$$

The transformation $\psi_n \rightarrow \psi_n \exp(-2iCz)$ converts Eq. (2.64) into Eq. (2.62). With $C = 1/(\Delta x)$, Eq. (2.64) is seen as a standard finite difference approximation to Eq. (2.62).

"Nada está perdido si se tiene el valor de proclamar que todo está perdido y hay que empezar de nuevo"

Julio Cortazar - Rayuela

3

Continuous Media Case

On a zero background, dissipative media admit the existence of two types of stationary self-organized bell-shaped beams: continuously "self-focusing" (positive chirp) and continuously "self-defocusing" (negative chirp). Each one of these beams or 2D *spatial bright solitons* are stable inside of a certain region of its existence. Beyond these two regions, they loose their stability, and new dynamical behaviors appear. Spatial bright solitons are not the only self-trapped beams that can be found on a zero background in continuous dissipative media. Radially symmetric ring structures with any *vorticity* can be stable (*bright vortex solitons*) in finite ranges of the parameters of the (2+1)D complex cubic-quintic Ginzburg-Landau (CQGL) equation.

In this chapter, we present several types of instabilities related to each beam configuration and give examples of beam dynamics in the areas adjacent to the region of stability. Although both types of beams mentioned above are considered as bright solitons, from now on we will use this adjective only for solutions with bell-shapped profile.

3.1 Introduction

Many problems in optics involving gain and loss can be formulated in terms of a single "master equation" that is, in one or another form, of the complex CQGL equation type (Aranson & Kramer, 2002; O. Descalzi & Tirapegui, 2005). This class of problems includes among others, passively mode-locked laser systems (Haus, 1975; Komarov et al., 2005; W. H. Renninger & Wise, 2008), optical parametric amplifiers (Taki et al., 2000), wide aperture lasers (Rosanov, 2005), spatial dissipative solitons (Ultanir et al., 2005) and three-wave mixing in optical fibers (Montes et al., 1997). Many of these problems can be (1+1)D and they deal with the evolution of spatially self localized one-dimensional fields (Deissler & Brand, 1994). More complicated are the (2+1)D problems, when the evolving optical field is two-dimensional. Examples of 2D dissipative solitons in optics are cavity solitons (Hachair et al., 2006) and solitons in wide aperture lasers (Rosanov, 2005). Special interest is given to those solutions known as optical vortices; they are screw wave front defects that appear in many branches of physics (Batchelor, 2000; Kleinert, 2008; Cramer et al., 1995). In recent years, they attracted much attention in optics (Bazhenov et al., 1992). Optical vortices in nonlinear media have special properties and they have been dubbed vortex solitons (Torres et al., 1998; Dreischuh et al., 1999; Malomed et al., 2002; Efremidis et al., 2007b). The transversal profiles of these fields can change during the evolution as well as can be stationary and stable. The variety of transverse profiles of two dimensional solitons can be enormous. An interesting observation is that the majority of these stable stationary profiles are not radially symmetric.

In the conservative cubic case, the main difference between the one-dimensional and two-dimensional systems is the problem of beam collapse. For the nonlinear Schrödinger equation, based on the paraxial approximation, 2D beams are predicted to concentrate all their energy in an extremely reduced transversal region. For the dissipative case, the collapse can be arrested, independently of its dimensionality. A beam having a positive or negative chirp in a conservative nonlinear medium would necessarily change its profile upon propagation. It would either self-focus or self-defocus. Dissipative media admit a different scenario. Even with chirp, the beam may remain stationary and propagate without changing its shape.

As in conservative homogeneous 2D systems, radially symmetric node-less (bell shaped) beams should be considered as the ground-state modes of its corresponding 2D nonlinear dynamical system. For the complex CQGL equation, ground state modes are stable in certain regions of its parameter space. At the edges of the stability regions, we can expect the appearance of either pulsating radially symmetric solutions or stable radially asymmetric solutions. Transformations happen at the points of bifurcation which in a multi-dimensional parameter space can be generalized to hypersurfaces of bifurcations. Other types of solutions can also appear as a result of such bifurcations. Thus, it is natural to find, as a first step, the set of radially symmetric solutions and then extend it to more complicated cases. However, it is occurred that dissipative systems in contrast to conservative ones admit more than one class of radially symmetric solutions.

In this chapter, we deal with optical beams of the (2+1)D complex CQGL equation. Our major observation is that there is a multiplicity of them. For bright solitons, we observed that in some cases the radial symmetry is lost for continuously focusing beams while in other case the radial symmetry is conserved during complicated beam transformations. On the other hand, vortex solitons beyond the region of stability loses their radial symmetry but may remain stable, keeping the same value of the topological charge. We have found bifurcations into solutions with n-fold bending symmetry, with n independent on S. Solitons without circular symmetry can also display $(S+1)$-fold modulation behavior. A sequence of bifurcations can transform the ring soliton into a pulsating or chaotic state which keeps the same value of the topological charge as the original ring.

3.2 Statement of the problem

Our study is based on an extended complex Ginzburg-Landau equation (Sergeev & Petviashvili, 1984; Crasovan et al., 2000), that includes cubic and quintic nonlinear terms and linear loss. In normalized form, this propagation equation reads:

$$\begin{aligned} i\psi_z + \frac{D}{2}\nabla_\perp^2\psi + |\psi|^2\psi + \nu|\psi|^4\psi = \\ i\delta\psi + i\varepsilon|\psi|^2\psi + i\beta\nabla_\perp^2\psi + i\mu|\psi|^4\psi. \end{aligned} \tag{3.1}$$

where $\psi = \psi(x, y, z)$ is the normalized envelope of the field,

$$\nabla_\perp^2 = \frac{\partial^2}{\partial x^2} + \frac{\partial^2}{\partial y^2}$$

is the transverse Laplacian, z is the propagation distance and (x, y) are the transversal coordinates, $\mathcal{D}$ is the diffraction coefficient that without loss of generality can be set to 1, ν is the saturation coefficient of the Kerr nonlinearity, δ represents linear losses, ε is the nonlinear gain coefficient, β stands for angular spectral filtering of the cavity, and μ characterizes the saturation of the nonlinear gain.

Stationary solutions of Eq. (3.1) can be found in wide regions of the space of the equation parameters. They are usually radially symmetric. In this case, the regions of their existence can be found semi-analytically using approximate methods such as in Ref. (Ankiewicz et al., 2008), with good agreement with the numerically obtained ones by solving directly Eq. (3.1).

The beam propagation method (BPM) is at present the most widely used tool employed in the study of light propagation in continuous systems. The essence of this algorithm consists of propagating the input beam over a small distance through a homogeneous space, and then correcting for the refractive index variations seen by this beam during the propagation step. We have implemented this numerical algorithm to find all the solutions reported in this chapter. A detailed description can be read in appendix A.

Around the boundaries of existence of these radially symmetric stationary solutions, more complicated objects can be observed. Then numerics appears to be the main tool to study them. They can be detected when we start from the region of stationary solutions and continuously change one or two of the equation parameters fixing all the others. At some point, the radially symmetric solution ceases to be stable, and a new solution appears.

The main parameter of the solution that we monitor in simulations is the beam power, Q:

$$Q(z) = \iint\limits_{\mathbb{R}^2} |\psi(x, y, z)|^2 \,\mathrm{d}\,x \,\mathrm{d}\,y. \tag{3.2}$$

The value of Q for a localized solution is finite and changes smoothly while the solution stays within the region of existence of a certain type of solitons. The value of Q changes abruptly when there is a bifurcation and the solution jumps from a branch of solitons that become unstable to another branch of stable solitons. Thus, monitoring Q allows us to find bifurcations in an easy way. Observing a finite Q also reveals the stability of a solution. As soon as the solution becomes unstable, it diverges and the value of Q either converges to another fixed value, vanishes or goes to infinity. In the case that the resulting solution is pulsating, instead of a fixed value of Q, we obtain a band of Q values that correspond to the changing power of the soliton. As we are interested in bifurcations from radially symmetric solitons, we start simulations from those found in Ref. (Ankiewicz et al., 2008).

Localized structures such as bell-shaped beams or rings with vorticity (topological charge) can be created using an initial condition with radial symmetry. We used the following initial condition that satisfies the above criteria:

$$\psi(r, z = 0) = A_o r^{|S|} \exp\left(-\frac{r^2}{w^2} + iS\theta\right), \tag{3.3}$$

where $r = \sqrt{x^2 + y^2}$, $S \in \mathbb{Z}$ is the vorticity, $\theta = \arctan(y/x)$, w is the radius of the intial ring structure, and A_o is a real amplitude that should generate sufficient power to place the initial condition into a basin of attraction of a spatial soliton. From here is clear that if $S = 0$ we have a bell-shapped initial condition without vorticity, being the appropiate *ansatz* to find bright solitons. If we have $S \neq 0$ the initial condition acquires a rotating phase and it can be used to find vortex solitons.

The initial condition converges to the solution which is stable at the chosen parameters of the equation. In cases when there are two or more stable solutions simultaneously, we have to take additional care choosing the parameters of the initial condition such that it falls into the desired basin of attraction. Once a soliton solution is found for a given set of equation parameters, we use it as initial condition for a nearby set of parameters. This technique is the main tool when looking for the continuous range of existence of solitons of the same type. A random perturbation can be added to stimulate the development of any asymmetry if the stationary solution has one. Numerical noise can also stimulate the asymmetry of the solution. However, the actual convergence to the stable solution in this instance takes longer distances z.

3.3 Bright solitons in dissipative media

Ankiewicz et al. (2008) showed that there are two major types of radially symmetric dissipative bright solitons of the 2D complex CQGL equation. Both have bell-shaped amplitude profiles, without nodes in their radial field distribution. The qualitative difference between them is their either concave or convex phase profiles, making them either continuously self-focusing or continuously self-defocusing beams. They were named solitons and antisolitons respectively. Both are robust in their corresponding regions of stability. However, at the edges of the stability regions, their behaviors differ significantly. The study of this difference can shed light on the properties of the stationary solitons as well.

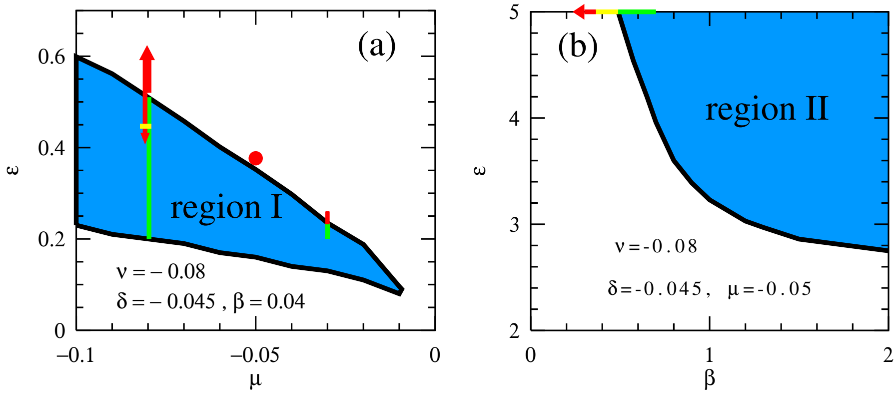

FIGURE 3.1: Regions (in blue) in the parameter space with radially symmetric stable stationary beams. The plot on the left (a) shows the region for continuously self-focusing beams (region I) and on the right (b) the one for continuously self-defocusing beams (region II). The location of these two regions in the five-dimensional parameter space is such that they cannot be represented in the same plane. Soliton solutions beyond these regions are either non-stationary or loose the radial symmetry. Below, we give examples located at the points indicated here by green, yellow and red lines. The change in color corresponds to a bifurcation. The arrows indicate the direction in which the parameters have been changed while obtaining a particular bifurcation diagram.

In particular, Soto-Crespo et al. (2000a) found that in (1+1)D configuration, dissipative solitons beyond their region of stability can be transformed into pulsating solutions and these into exploding solitons. The latter stay as stationary solitons for certain distance of propagation and intermittently explode into many pieces (Akhmediev et al., 2001). In the (2+1)D case, this is the only instability we were able to find around continuously self-defocusing beams. On the other hand, continuously self-focusing beams have a richer structure of bifurcations around the boundaries of the region of their stable existence. Radially symmetric beams can be transformed into beams of elliptic shape, beams of completely asymmetric shape, pulsating beams etc., when we change the parameters of the system. The study of these transformations is one of the interesting aspects of the theory of dissipative solitons. Thus, in this chapter we give (2+1)D solutions with distinctive features which appear close to the boundaries of the regions of existence of continuously self-focusing and continuously self-defocusing solitons.

Figure 3.1(a) shows a region in the parameter space (region I) where radially symmetric continuously self-focusing beams have been reported in the paper by Ankiewicz et al. (2008). A region of existence of continuously self-defocusing beams (region II) is shown in Fig. 3.1(b). Our aim here is to study what happens around these two regions. A complete mapping is a difficult task because of the multiplicity of the different types of solutions and the myriad of bifurcations between them. Thus, we restrict ourselves to certain examples which on one hand show these difficulties and on the other hand represent the possible types of solutions.

We have chosen a few lines that cross the boundaries of the blue regions in Fig. 3.1 and studied the types of solutions that appear around them. When two types of solutions are stable simultaneously, the simulations produce the one which is closer to the initial condition. Moving step by step in small increments of ε or β we can use as the initial condition, the solution obtained at the previous step. This technique allows us to follow the branch of the solution that was stable at the previous step. Moving first in one direction and then in the opposite direction provides us with the information about the types of solutions that exist on this line and the bifurcations between them. The bifurcation diagrams presented below are obtained in this way. Shifting the direction in the parameter space along which we move, changes the bifurcation diagram but keeps the major types of solutions obtained here intact.

As the blue region I in Fig. 3.1(a) represents the “ground state” solutions, there are no solitons below it because the power pumped into the system is smaller for lower values of ε. Solutions with higher power Q exist above the blue region I. The specific cases presented below are obtained on the two vertical lines in Fig. 3.1(a) and on the upper left horizontal line in Fig. 3.1(b). Namely, Fig. 3.2 corresponds to the right hand side vertical line with $\mu = -0.03$ at (a). Figs. 3.3, 3.4 and 3.5 are obtained for $\mu = -0.08$, i.e. on the left hand side vertical line in (a). The horizontal line in (b) for $\varepsilon = 5$ corresponds to the case shown in Fig. 3.14. Each color interval of the lines (green, yellow or red) corresponds to a particular type of solution. The arrows show the direction in which the parameters ε or β were changed when obtaining a bifurcation diagram. When there is no arrow, the bifurcation diagram does not depend on the direction of changing the parameter. The red solid circle in (a) represents the location of the case shown in Fig. 3.9.

3.3.1 Bifurcation diagrams

As it was outlined in the introduction, we are interested in soliton dynamics at the parameter regions adjacent to the regions of stable stationary solitons. Firstly we concentrate on the regions close to the region of continuously self-focusing radially symmetric solitons (region I). The existence of boundaries manifests the instability of the stationary soliton and the corresponding bifurcation of the soliton into a different state. These boundaries are surfaces in a five-dimensional parameter space $(\nu, \delta, \varepsilon, \beta, \mu)$. They can be visualized using two dimensional plots with three of the parameters being fixed. Transitions related to the loss of stability can take a multiplicity of different forms. Each one has to be studied individually. For the purposes of the present chapter we restrict to present the crossing of the boundary of stability at a single point and in a single direction. We may expect that moving this point along the boundary will leave the qualitative features of the transition being similar to the one that we present when the point is still in close proximity to the original one.

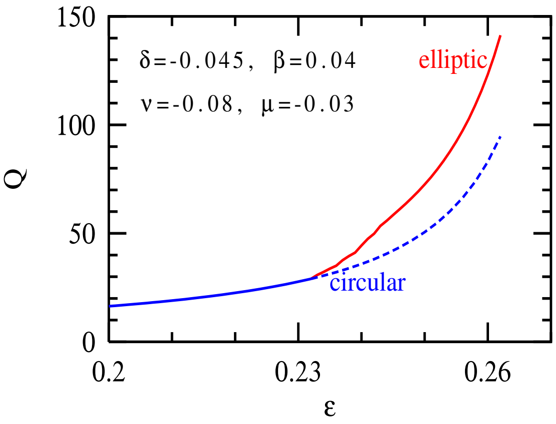

FIGURE 3.2: Bifurcation of an elliptic soliton from the self-focusing radially symmetric one.

One of the simplest bifurcations that we have found is the transition from a radially symmetric solution to a soliton of elliptic shape that is also stable and stationary. This transformation happens close to the blue region in Fig. 3.1(a) on the short green vertical line with $\mu = -0.03$. The bifurcation diagram for such transformation is shown in Fig. 3.2. The beam with radial symmetry loses its stability after the bifurcation (blue dashed curve in the diagram). This can be considered as an example of symmetry breaking bifurcation in the case of 2-D beams. Due to the symmetry of the equation 3.1 the long axis of the elliptic soliton can have any direction in the (x, y)-plane, what causes the solution to rotate. This elliptic soliton is the only stationary, although rotating, solution different from the radially symmetric one that we were able to find for $\mu = -0.03$. It exists in a stripe (marked in red) above the upper boundary of the blue region (region I). Depending on the initial conditions, the beam may oscillate around the configuration with radial symmetry before finally converging to the stationary beam of elliptic shape. An example of such oscillations for different set of the equation parameters is given in section 3.3.3. Although in that case the final stable solution is different.

Figure 3.3(a) shows, in red dotted line, the beam power of the solutions obtained when we increase ε, starting from a radially symmetric solution at $\varepsilon = 0.2$. The power Q increases continuously until an abrupt transition occurs at $\varepsilon \approx 0.52$. The latter is shown by the black arrow pointing up. It indicates the transformation of the single soliton solution into a stable rotating double-beam complex, which exists in the range of ε from 0.47 to 0.6. Thus, from here, we can either increase or decrease ε and stay at the same branch of solitons. Reaching further $\varepsilon = 0.6$, we observe a second bifurcation where Q takes a continuous interval of values. It corresponds to pulsating and simultaneously rotating double beams with an oscillating value of Q.

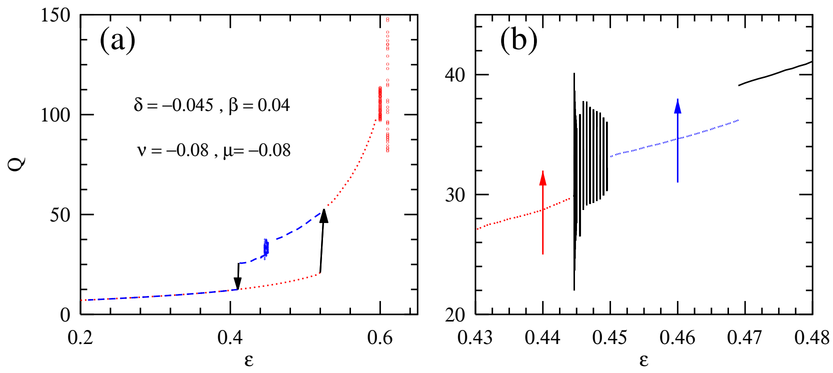

FIGURE 3.3: (a) Q versus ε diagram as obtained when increasing (red dotted line) or decreasing ε (blue dashed line). (b) magnification of a portion of the upper blue curve around the hysteresis cycle between the two black arrows in (a). The red dots in this case correspond to stationary beams of elliptic shape while the blue dashed line corresponds to stationary beams without any radial symmetry. Typical examples of these two types of solutions are plotted in Figs. 3.4(a) and 3.4(b) respectively for the ε values indicated here with the red and blue arrows. Black vertical lines with continuous values of Q in (b) correspond to pulsating localized solutions.

Alternatively, when we decrease the value of ε, Q follows the blue line.

Two solutions can be observed in a certain interval of ε values, manifesting a hysteresis phenomenon. Moreover, we can observe additional bifurcations in this region which can be clearly seen if we magnify properly this region of ε (see Fig 3.3(b)). When we move from right to left, three main transitions can be clearly seen: i) transition from a double-beam complex (black solid line) to an asymmetric comma-shaped solution (blue dashed line), both being stationary, ii) transition to pulsating solutions (vertical lines indicating that Q takes a continuous set of values) and iii) transition to elliptically shaped beams along the red dotted line. The red and blue vertical arrows indicate the values of ε for which the solution is plotted in Figs. 3.4(a) and 3.4(b) respectively. These 3D-plots illustrate the type of solutions that we obtain in the ranges between the bifurcations. Fig. 3.4(a) shows the solution with an elliptic profile while Fig. 3.4(b) shows the solution that looks as composed of two unequal beams closely attached to each other. The profile would look more like a comma-shaped on a contour plot.

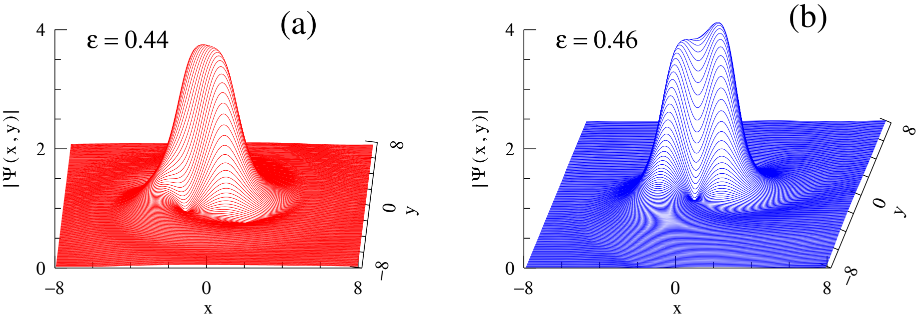

FIGURE 3.4: Solitons (a) of an elliptic shape and (b) without any radial symmetry (comma shaped) for the values of ε indicated in Fig. 3.3(b) by the red and blue arrows.

Figure 3.3 shows that soliton solutions are highly sensitive to the change of ε. Indeed, if we further magnify the scale of ε in Fig. 3.3(b) we will be able to see more bifurcations. These are shown in Fig. 3.5. For the sake of clarity, we just show here the maximal and minimal values of $Q(z)$ denoted as Q_M and Q_m respectively. The green line at the left hand side of this plot corresponds to rotating solitons with fixed elliptic profile. Their fixed, although rotating, shape results in their fixed values of Q. The green line at the right hand side of the plot corresponds to highly asymmetric solitons with the fixed shape of a comma that are also rotating. Typical examples of the two shapes are shown in Fig. 3.4. Several bifurcations appear in between these two regions. The first one, when reducing ε appears as a transition from stationary solution to pulsating soliton with a single period of pulsations. The resulting Q oscillates between the red and blue curves that correspond to the maximal and minimal values of Q of the pulsations. The oscillations of Q are very close to being harmonic for pulsating solutions with a single period. The pulsations turn into period doubled ones at the second bifurcation in Fig. 3.5. As a result, the two curves split into four at this point. Further reduction in ε results in the soliton evolution that looks very much like chaotic before finally turning into an elliptically shaped stationary solitons. Generally speaking, a myriad of other bifurcations may occur at this short interval.

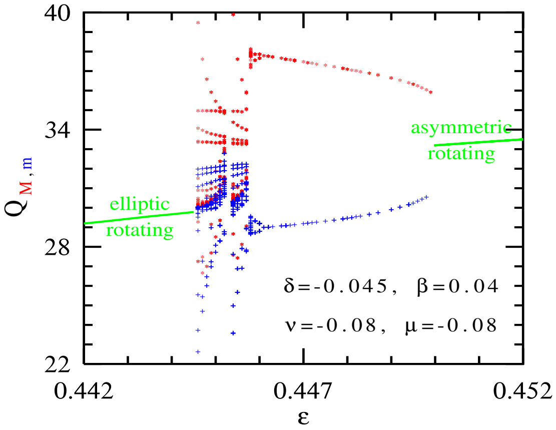

FIGURE 3.5: A portion of the diagram in Fig. 3.3(b) with a magnified scale. In this case only the maxima (Q_M) and minima (Q_m) of the beam power are shown. The two branches for stationary solutions corresponding to solutions of elliptic shape (left) or highly asymmetric solutions (comma-shaped) with constant Q are shown in green. The red points represent the maxima of the curves $Q(z)$ and the blue points the minima. The data for this plot are obtained when decreasing ε. The period-1 solutions bifurcate from the asymmetric solutions at $\varepsilon = 0.45$. Period-doubling bifurcations appear at $\varepsilon = 0.446$. A much more complicated type of pulsations appear at $\varepsilon = 0.445$. These look like a beating of the two types of stationary solutions (elliptic and highly asymmetric).

3.3.2 Period-1 pulsating solitons

Pulsating solutions appear in dissipative systems as naturally as stationary ones as they represent limit cycles of the infinite-dimensional dynamical system (Akhmediev et al., 2001). For 1-D systems they are usually located near the stationary solutions in the parameter space. The transformation of stationary solutions into pulsating ones occurs in the form of an Andronov-Hopf bifurcation. Due to the relative simplicity of the soliton profile in the 1D case, this bifurcation can be studied using a trial function approximation in combination with the method of moments (Tsoy & Akhmediev, 2005). In the 2D case, the pulsating soliton profile can be much more complicated. In fact, in most of the cases it lacks the radial symmetry, thus making the approximation with a trial functions difficult. Radially symmetric pulsating solutions exist only in the vicinity of the region of continuously self-defocusing beams (region II). Near the region I, the shape of pulsating solitons look similar to the examples shown in Fig. 3.6. The soliton profile changes continuously upon propagation. The profiles given in Fig. 3.6 are taken when the value of Q takes its maximal or minimal value inside each period of pulsations. As we can see, in each case, the beam lacks the radial symmetry.

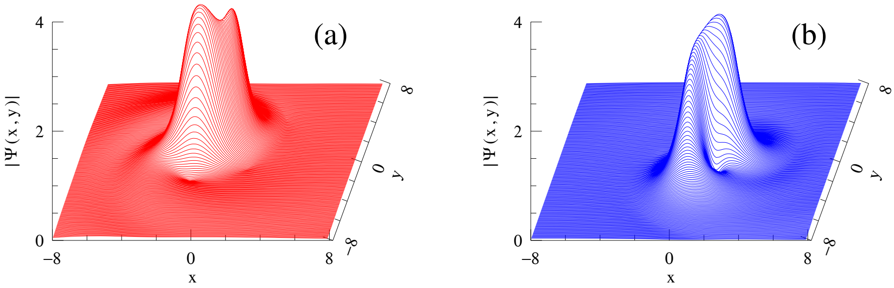

FIGURE 3.6: Pulsating 2D soliton profiles when the oscillating power Q takes its (a) maximal and minimal values (dashed and dotted vertical lines in Fig. 3.7 respectively).

The beam power Q in this case is a periodic and almost harmonic function of the propagation distance z. This function calculated for a fixed set of equation parameters is shown in Fig. 3.7. The dashed vertical lines determine the value of z for which the profiles in Fig. 3.6 are taken. Namely, the red dashed line corresponds to a maximum of power Q while the blue dotted line corresponds to a minimum of Q. The beam rotates, continuously, changing its profile at the same time. The dissipative pulsating soliton in this example should be considered as a two-soliton complex with continuous unsuccessful attempts to split into two independent beams. In the particular case that is shown above, one of the beams comprising the complex is weaker than the other one making the structure asymmetric. In addition, the whole structure is rotating. In fact, it is the asymmetry of the soliton that pushes it into a spiraling motion. The periodicity itself has nothing to do with its rotation. The angular speed of rotation is not related to the frequency of pulsations. Thus, the rotation does not influence the periodicity in evolution of Q. The transversal motion of the beam in one period, between two consecutive minima values, is sampled in Fig. 3.8. This is not surprising because the momentum as well as the power Q are not conserved in dissipative systems. The asymmetry of the beam causes its motion because of the asymmetry in the energy flow across the soliton. The asymmetry of the soliton changes with the speed different from the angular speed of its rotation thus resulting in the average transverse motion.

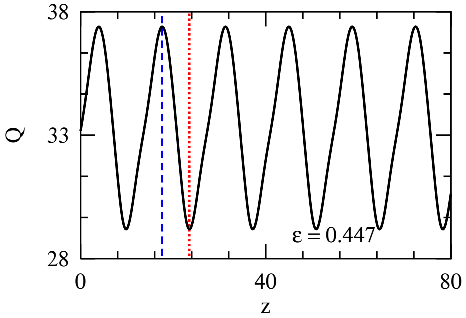

FIGURE 3.7: Periodic evolution of Q versus z for a pulsating soliton with a single period. The red and blue vertical lines show a maximum and a minimum of Q. The corresponding profiles are shown in Fig. 3.6(a) and Fig. 3.6(b) respectively.

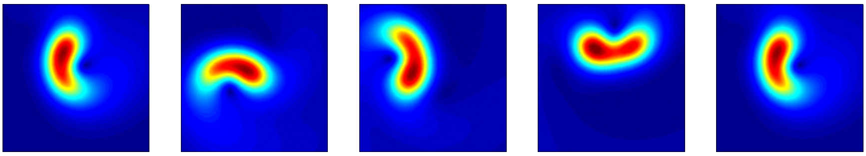

FIGURE 3.8: Snapshots of one period beam evolution between two consecutive Q minima values displayed in Fig. 3.7.

3.3.3 Elliptic beam oscillations

Soliton pulsations in the example of the previous section do not have any radial symmetry. The question arises whether pulsations that keep the radial symmetry are at all possible around the region I. When shifting to a different point (e.g., $\mu = -0.05$) along the upper boundary of region I in Fig. 3.1(a) we can find symmetric beam oscillations which, after some propagation distance, end up being transformed into an elliptic shape solution. These are shown in Fig. 3.9. The main plot shows the evolution of Q with z. Simulations started from a two-dimensional elliptical Gaussian function at $z = 0$, namely

$$\psi(x, y, z = 0) = A_0 \exp\left[-\frac{x^2}{w_x^2} - \frac{y^2}{w_y^2}\right], \tag{3.4}$$

with $w_x^2 = 1.2$, $w_y^2 = 1.1$ and $A_0 = 5$.

As the parameters are chosen at the margin of stability of stationary solutions, the beam cannot converge to the radially symmetric solution of Eq. (3.1). Instead, the small initial asymmetry increases and after an initial transition, the beam converges to a pulsating state without radial symmetry. The beam still has radially symmetric profile when Q takes its maximum value but elongates alternatively either in x or in y directions when Q takes its minimal value.

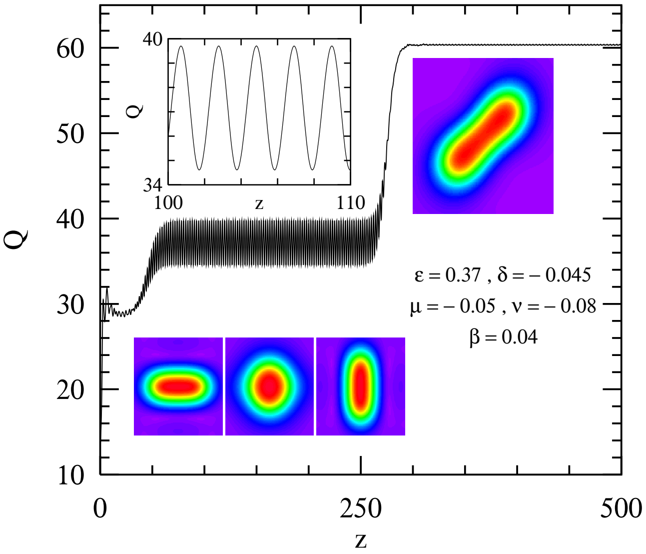

Figure 3.9: Dissipative soliton oscillations in two transverse dimensions. The solution converges to these oscillations at around $z \approx 120$. The power oscillations are shown in greater resolution in the upper left inset; they are almost harmonic. Color plots in the lower left insets show the intensity profiles when Q reaches two consecutive minima (left and right frames) and any maximum (central frame). The oscillations are weakly unstable and are transformed into a stable configuration at $z \approx 260$, consisting of a twin soliton profile shown at the upper right inset that rotates around its center of symmetry

Three consecutive color coded contour plots for the intensity profiles at the extremal points of $Q(z)$ are shown in the lower left inset panels of the figure. The orientation of the elongated profile changes from one consecutive minimum to another one, as shown in the inset. Oscillations of Q are harmonic with high accuracy as shown in the upper left panel of the figure which is a magnified version of the $Q(z)$-plot between $z = 100$ and $z = 110$. These oscillations are persistent and last from $z \approx 60$ till $z \approx 260$. However, the pulsating solution at the chosen set of parameters is not completely stable and it is transformed into another stable solution at the end of this interval. Namely, it is transformed into another elongated structure which can be considered as a two-soliton complex. The color contour plot for the intensity profile is shown in the upper right panel of the figure. This beam is also rotating around the central point of its symmetry. Thus, we tend to think that pulsations that keep the radial symmetry at any z do not exist around the region I. Additional studies are needed to give a more definite answer to the question posed in the beginning of this section.

3.3.4 More complicated pulsations

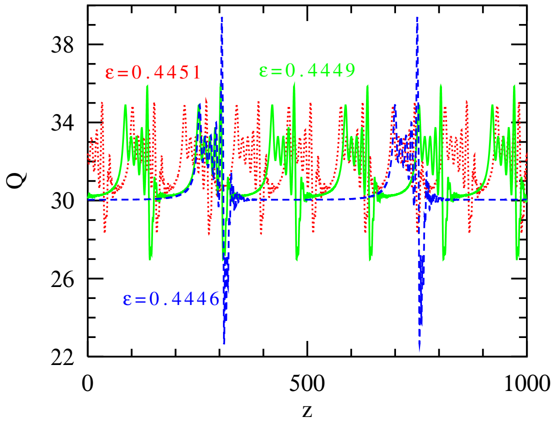

FIGURE 3.10: Periodic evolution of Q versus z for three values of ε. As ε decreases the maxima of Q increases as well as the separation between "bursts". The red curve is horizontal for large interval of values of z during which the solution is of elliptic shape.

One of the distinctive features of the simple pulsations presented in the two previous sections is the almost harmonic evolution of $Q(z)$. This feature disappears when we move into the visibly chaotic region in the center of the diagram in Fig. 3.5. The beam evolution is still periodic but far from being harmonic. Three examples of complicated evolution of $Q(z)$ are shown in Fig. 3.10(a). The three curves (blue, green and red) have a few common features. The power of the beam experiences periodic bursts with preliminary oscillations of smaller amplitude. The latter are preceded by intervals of almost constant Q. These complicated changes of Q appear due to the involved evolution of the soliton profile itself. The sequence of the beam evolution is shown in Fig. 3.10(b). In the intervals with relatively small changes of Q, the profile takes an elongated asymmetric shape. Due to the asymmetry, the beam center rotates in the transverse plane. Subsequent oscillations of Q correspond to the appearance of two maxima in the beam profile and a tendency to split the solution into two beams with radiation waves shed around them. The beam profile at this stage has the familiar comma shape. The bursts of power appear when the two beams are separated by the maximal distance inside each period. The beam itself wanders around with the center of mass moving in circles in the transverse direction.

Figure 3.11(a) shows the trajectory of the main maximum of the optical field in one full period of evolution. The curve is plotted for the value of $\varepsilon = 0.4446$ that corresponds to the blue curve in Fig. 3.10(a). Fig. 3.11(b) reproduces more clearly one period of evolution of Q for $\varepsilon = 0.4446$. The "quiet" stage of evolution with almost constant Q is shown in Fig. 3.11(a) in blue line while the "turbulent" stage of evolution, when Q changes substantially, is shown in green line. The latter corresponds to the interval in Fig. 3.11(b) enclosed inside the green rectangle. The beam moves intermittently from one position to another one inside this green interval. The beam rotates but stays almost at the same position outside of the green box where Q hardly changes. The blue trajectory in Fig. 3.11(a) is a circle rather than a point because the maximum of the field is shifted relative to the center of mass of the beam. To complete the description we should add that the evolution of Q is strictly periodic rather than intermittent.

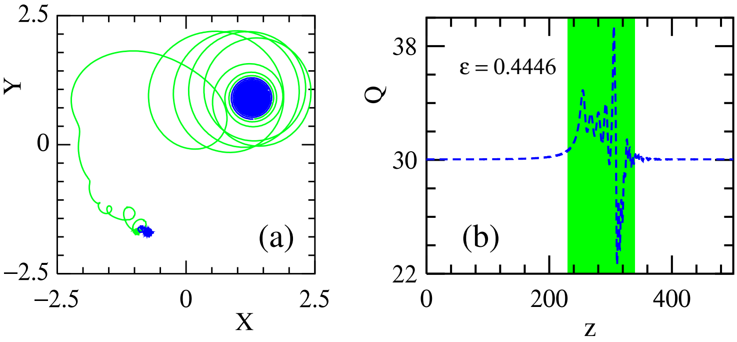

FIGURE 3.11: Periodic evolution of the solution for $\varepsilon = 0.4446$ (blue curve in Fig. 3.10). The green trajectory in (a) corresponds to the green zone in (b).

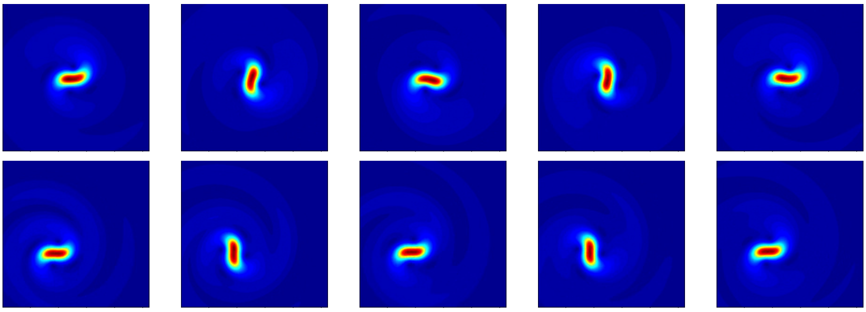

FIGURE 3.12: (Upper row) Dynamic beam evolution during its last rotation before crossing the green zone in Fig. 3.11(b). (Lower row) Color map plots for the first beam rotation after crossing the green zone. The position of the beam is transversally shifted.

Similar behavior can be observed in a small band of ε values from 0.4446 to 0.4451. Six consecutive periods of evolution of the beam for $\varepsilon = 0.4449$ are shown in Fig. 3.13. Each of the six periods is depicted in a different color. The evolution of the power Q is identical in each of the periods. The trajectory of the maximum of the optical field in each period is similar to the one shown above. Each time, it converges to a circle whose center shifts to another position from one period to the next. The shifts are regular and all circles are located around a fixed point in space. So, in average, the beam stays at the same place in space. The fast part of the trajectory is sensitive to numerical errors. Thus, the boundaries of the used numerical grids are taken to be far away from the beams and calculations have been repeated with several grid sizes and step lengths to be sure that no numerical artifacts are presented here. The snapshots in Fig. 3.12 accounts for (upper row) last rotation before the beam leaves the "quiet" zone, and the (lower row) first rotation after the beam leaves the "turbulent" zone.

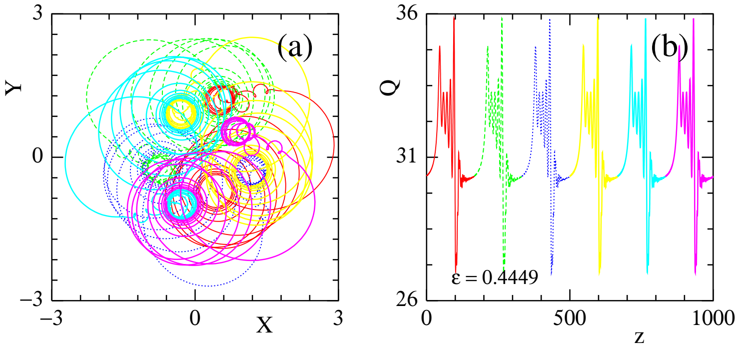

FIGURE 3.13: a) Trajectory of the peak intensity of the solutions in the (X,Y) plane and b) evolution of Q versus z. Six periods are plotted, each with a different color. The position of the solution behaves somehow chaotic.

3.3.5 Beam evolution around the region of continuously self-defocusing beams

As the last example, we consider the soliton evolution next to the region of continuously self-defocusing beams (region II) shown in Fig. 3.1(b). The beam evolution is similar across the whole lower left boundary (black solid curve). Thus, we consider a single line of exit from this region at $\varepsilon = 5$ (tri-color arrow in the top of Fig. 3.1[b]). The beam is transformed into a pulsating one on the yellow part of the arrow and further into the exploding soliton at the red part of the arrow. However, our simulations show that upon these transformations the beams do not lose the radial symmetry.

A typical example of bifurcation diagram when moving along the tri-color line out of the region of stationary beams is shown in Fig. 3.14. The power Q is finite and stays constant in z at values of β higher than 0.55. At $\beta \approx 0.55$, we observe an Andronov-Hopf bifurcation where the beam starts to pulsate. These pulsations are revealed with the splitting of the Q value into a maximum, Q_M, and a minimum Q_m values in the bifurcation diagram. This occurs at

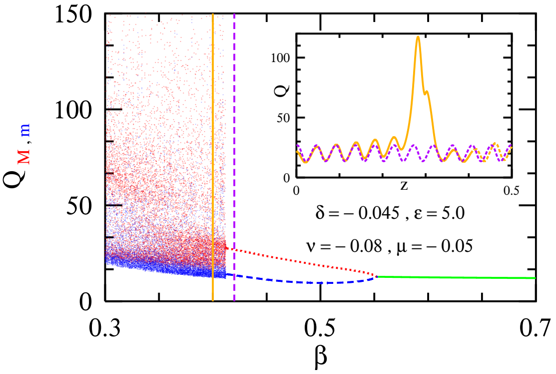

FIGURE 3.14: Bifurcation diagram at the boundary of the region II. An Andronov-Hopf bifurcation of a stationary self-defocusing beam into a pulsating one occurs at $\beta = 0.55$. The inset shows the power evolution with z for two cases: $\beta = 0.42$ (magenta) and $\beta = 0.4$ (amber). In the interval $0.41 < \beta < 055$ the beam is pulsating. The $Q(z)$ curve is harmonic. The evolution is chaotic at the values of $\beta < 0.41$. The $Q(z)$-curve (amber) reveals the beam explosions.

$\beta \approx 0.55$. An example of oscillating $Q(z)$ is shown in the inset of Fig. 3.14 by the magenta dashed curve. It is taken at $\beta = 0.42$. This value of β is indicated by the vertical dashed line in the bifurcation diagram itself. As mentioned, the beam stays radially symmetric in these pulsations. Any perturbation with radial asymmetry vanishes on propagation.

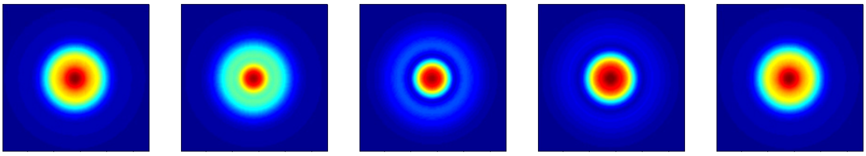

FIGURE 3.15: Snapshots for one period of the evolution corresponding to pulsating solution located at $\beta = 0.42$ in Fig. 3.14. The period has been sampled in five steps

At lower values of β, the evolution becomes chaotic. This happens below $\beta \approx 0.41$. Then instead of just two values of Q, we have a wide band of them corresponding to local maxima and minima of Q. The beam in this region becomes exploding. Its width increases dramatically to high values and the corresponding power also increases. The soliton explosions are similar to those observed in the (1+1)D case (Soto-Crespo et al., 2000a; Akhmediev et al., 2001). They occur intermittently and each explosion is different from the previous one. The increase of Q for one explosion is shown in the inset of Fig. 3.14 with the amber curve. The radial symmetry is lost at the explosion point but it is restored again in returning back to a beam with radial symmetry. The snapshots in Fig. 3.15 accounts for the evolution displayed in the inset of Fig. 3.14. This complex dynamic correspond with the amber curve, and it has been sampled in five steps.

These two types of evolution are the only ones that we were able to observe near the region of existence of self-defocusing beams.

3.4 Vortex solitons in dissipative media

In a light wave, a phase singularity is known to form an optical vortex. The intensity of the field is null at the singular point and its phase takes all the values between 0 and 2π. Vortex solitons can exist both in continuous (Tikhonenko et al., 1998; He et al., 2008; Neshev et al., 2008) and periodic media (Alexander et al., 2004; Yang, 2004; Kartashov et al., 2005; Wang & Yang, 2008). Under certain circumstances self-trapped localized states can exits as dips or holes, carrying a phase singularity, in a large-amplitude wave background. They are called *dark* vortex solitons (Kivshar & Luther-Davies, 1998). However, most of the studies have been restricted to optical vortices that are nested in bright beams on a zero intensity background (G. A. Swartzlander & Law, 1992; Tikhonenko & Akhmediev, 1996). The requirement of zero field at the center of the beam converts them into ring structures. These can exist as exact solutions of nonlinear wave equations. Vortex ring solitons with high value of vorticity are of special interest (Towers et al., 2001). Their stability in conservative media is a controversial issue (Michinel et al., 2001, 2004). Generally, ring structures in conservative media have been found to be unstable with respect to the modulation instability (Soto-Crespo et al., 1991). The result of such instability is usually the filamentation of the beam. In this respect, we should note that the stability properties of vortex solitons in dissipative media (Crasovan et al., 2001; Fedorov et al., 2003; Rosanov, 2005; Mihalache et al., 2008) are quite different from those in conservative media.

We have found families of ring solitons with arbitrary vorticity, (S), including higher-order ones ($S > 2$). For each S, there is a variety of such solutions with the ground state being a stable ring with azimuthal symmetry. The radius of the ring grows with increasing S. They are stable and stationary in large regions of the parameter space. Other types of solutions with the same S bifurcate from the ground state branch at certain values of the parameters. When the vortex ring solitons lose their cylindrical symmetry, they become modulated and exhibit a number of amplitude maxima along the ring. This number is usually equal to the value of the vorticity plus one, i.e. $S + 1$. Generally speaking, vortex solitons without cylindrical symmetry exist in narrower regions of the parameter space and their shapes vary. They remain as a complete ring but acquire a nontrivial azimuthal structure. The ring itself may pulsate and rotate simultaneously or can be involved in only one of these motions. The dynamics of the highest complexity is a chaotic one.

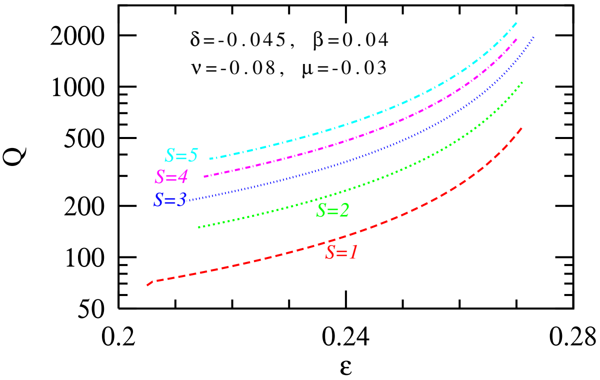

FIGURE 3.16: The power Q vs ε for the radially symmetric vortex dissipative solitons with $S = 1, 2, 3, 4$ and 5. Note the logarithmic scale along the vertical axis.

We started our simulations finding only radially symmetric solutions. Usually these solutions occupy finite, relatively large regions in the parameter space. Solutions with different values of S may exist simultaneously at the same set of the equation parameters. Moreover, the regions of existence of vortex solitons with different S roughly coincide. Only the edges of these regions vary slightly with the value of S. This can be seen from Fig. 3.16 which shows the power, Q, versus ε for radially-symmetric vortex solutions of different vorticity. The set of parameters used in these simulations are shown inside the figure. For a given ε value, the power Q of these solutions is proportional to S with high accuracy, i.e. the solution with vorticity $S > 1$ has virtually S times the power of the vortex soliton with $S = 1$. The examples for values of S from 1 to 5 allow us to conclude that ring vortex solitons with S higher than 5 must also exist. At higher values of S, the solutions are gradually transformed into round stripes of finite width. Thus, at higher S, their stability is related to the stability of the stripe. This means that ring vortex solitons can exist for any higher S value.

The region of existence for ring vortex solitons is relatively large in every direction in the parameter space. Even if the parameters are moved well away from those given in Fig. 3.16, the curves have similar width in ε domain. In the rest of this section, we use the set of parameters ($\delta = -0.1, \beta = 0.1, \mu = -0.04, \nu = -0.02$) and change only ε to observe the bifurcations. For this set of parameters, radially symmetric solutions with any particular S also exist in a finite range of ε values. Beyond that range we can observe other types of solutions. These include solutions with broken radial symmetry and non-stationary localized rings. They can be found when, starting from a symmetric vortex solution, we continuously change one of the equation parameters fixing all the others. At a point of bifurcation, the radially symmetric solution ceases to be stable, and a qualitatively new type of solution appears. The transformations and their location in the parameter space depend very much on the value of S.

Therefore, in what follows, we consider separately the bifurcation diagrams for each S.

3.4.1 Ring vortex solitons with $S = 1$

Using the set of parameters given in the previous section, we have found a variety of stable ring solitons with vorticity $S = 1$ and the ranges of their existence in the ε domain. These ranges are presented in Fig. 3.17 with the color curves in the $Q(\varepsilon)$ diagram. Different colors indicate different types of solution. Namely, vortex solutions that are represented by the red curve are radially symmetric, while the blue and green curves represent vortex solitons with broken radial symmetry. In particular, the green dashed curve corresponds to unstable stationary solutions, the green solid line stands for stable stationary ones, and the blue stripe represents stable pulsating ring structures. The finite width of this stripe shows the range of Q-values that the soliton takes in its oscillations.

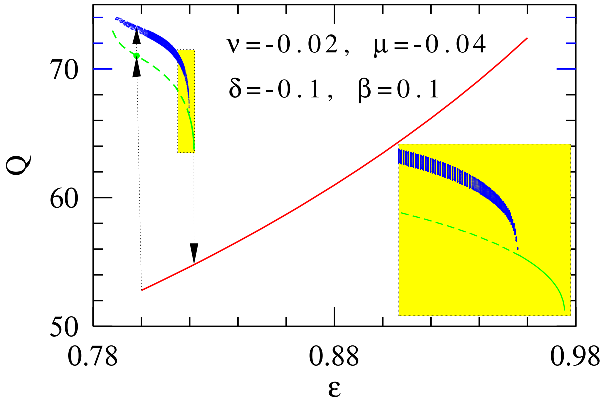

FIGURE 3.17: Power Q versus ε diagram for the ring solitons with vorticity $S = 1$. The red and blue curves and the solid part of the green curve correspond to stable solutions, while the dashed green one is for unstable ones. Solutions on the red curve have a radially symmetric amplitude profile while other solutions are radially asymmetric. The yellow inset in the lower right corner is a magnification of the curves enclosed into the small yellow rectangle in the upper left part of the main diagram. This magnification shows more clearly the bifurcation of the pulsating vortex solutions (blue stripe) from the stationary radially asymmetric ones (green curve).

In order to plot these curves, we started the numerical simulations at the point $\varepsilon = 0.88$ using the initial conditions (3.3). From this point, we moved step by step in the directions of decreasing and increasing ε and found new solutions using the solution at the previous point as initial condition for the new point. When ε is decreased below 0.80, the radially symmetric vortex solution loses its stability and transforms itself into a vortex soliton without radial symmetry.

This transition is shown by the black vertical arrow pointing at a solid dot on the green dashed curve. Solutions on the dashed part of the green curve occurred to be weakly unstable. They are transformed upon farther propagation into pulsating vortex ring solitons. This transformation is shown by the smaller black arrow above the first one.

Starting the simulations with this new radially asymmetric solution as initial condition, we can plot the $Q(\varepsilon)$ curves for these branches of solitons in the same way as described above, i. e. increasing and decreasing ε in small increments. For clarity, the part of the curves enclosed into the small yellow rectangle in the upper left corner of the diagram is magnified and plotted separately in the lower right hand side yellow panel of Fig. 3.17. This inset shows clearly the bifurcation of the pulsating solutions from the stationary radially asymmetric ring solitons. The latter solutions turn to be unstable to the left of the point of bifurcation (i. e. on the dashed green line). The instability occurred to be weak and these solutions still can serve as temporary attractors for initial conditions that are close to the radially symmetric solitons of the red curve. This is why the transition shown by the black arrow stops temporarily at the solid green circle before the solution is further transformed into the pulsating soliton of the blue stripe. Radially asymmetric vortex solitons exist up to the point $\varepsilon = 0.821$. Further increase of ε transforms them into radially symmetric ring solitons. This transition is shown by the black arrow directed down to the red curve. The two arrows enclose the hysteresis cycle.

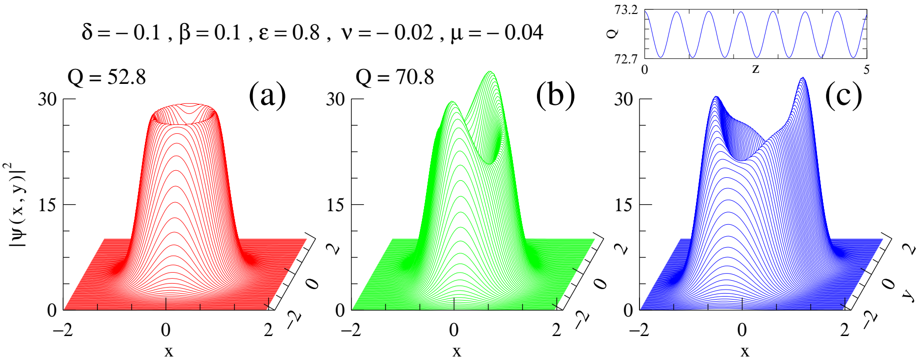

Figure 3.18: 2D vortex soliton profiles for $S = 1$ for the equation parameters, written in the upper left part of the figure. In the cases (a) and (b) the power, Q is constant, while for (c) the power is a periodic function of z, as it is shown on top of the panel (c).

Soliton profiles in the (x, y) plane for the three types of solutions described above are presented in Fig. 3.18. The color of the plot corresponds to the color of the curve in Fig. 3.17 to which they belong. All profiles are calculated for the same set of equation parameters. They are given on the top of the figure. The

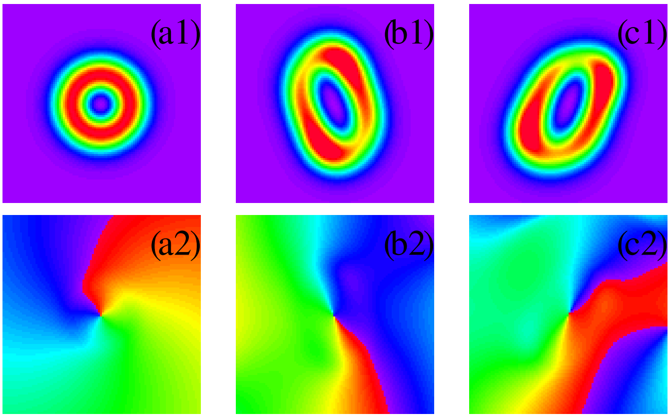

Figure 3.19: (Upper row) Contour color plots of the soliton profiles shown in Fig. 3.18. (Lower row) Contour color plots of the phase profiles for the same solutions.

profile shown in red is radially symmetric while the solutions (b) and (c) are not. The profile in (b) still has two-fold azimuthal symmetry which is lost in further transformations. The two latter solutions rotate on propagation. The profile (c) also changes periodically in z. Consequently, the power Q oscillates as shown in the upper blue panel in (c).

Contour color plots of the same soliton profiles are shown in the upper row of Fig. 3.19. This plot shows clearly that the solitons of the red branch are radially symmetric while the solitons of the blue and green branches are not. The lower row of Fig. 3.19 shows the phase contour plots for each solution. In each case, the phase increases by 2π in one rotation around the center of the ring. The snapshots sequence recorded in Fig. 3.20 illustrates a quarter-period of the clockwise rotation of this solution.

Ordinary bell-shaped solitons with zero vorticity also exist at this range of parameters. They are not shown here because the power Q for them is much below the scale of Fig. 3.17. Namely for the equation parameters presented in Fig. 3.17, they are stable in the interval of ε values: $[0.30, 0.89]$. This means that if any of the ring vortex solitons loses stability for one or another reason inside the above interval, it will be transformed into a finite number of plain bell-shaped dissipative solitons. The process is similar to a small scale filamentation of the rings (Soto-Crespo et al., 1991).

3.4.2 Ring solitons with $S = 2$

Following the same procedure as above we have obtained the regions of existence of vortex solitons with $S = 2$ for the same set of parameters as in the previous case. These regions are presented in Fig. 3.21 by the red and blue curves. In contrast to the case $S = 1$, we have only two branches of ring vortex solitons.

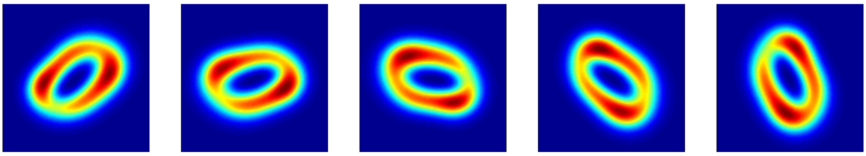

Figure 3.20: Snapshots of dynamical evolution of the soliton profile shown in Figs. 3.18(c). The sequence corresponds with quarter-period of the clockwise rotation of this solution.

The red curve corresponds to solitons with circular symmetry while the radially asymmetric solitons are shown with the blue curve. In each case, the solutions have constant power, Q, at any fixed ε although radially asymmetric solitons may change the shape in propagation. In particular, the solitons represented by the blue curve are close to have a triangular shape with three maxima. In addition, this triangular structure rotates with a constant angular velocity.

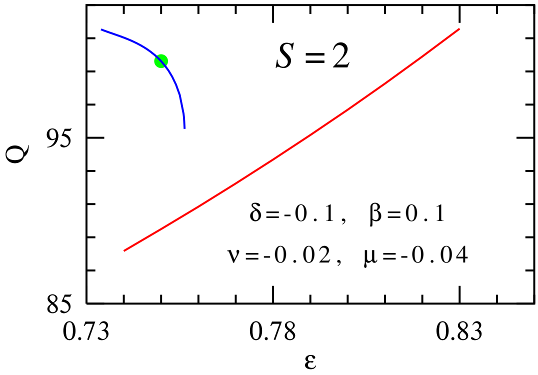

Figure 3.21: Regions of existence of vortex solitons with $S = 2$. The red curve corresponds to the radially symmetric ring solitons. Solitons represented by the blue curve are radially asymmetric. The thick filled green circle indicates the location, in the parameter space, of the vortex soliton whose intensity and phase profiles are shown in Fig. 3.22.

An illustrative example of this class of ring vortex solitons is shown in Fig. 3.22. This example corresponds to the thick filled green circle in Fig. 3.21. The soliton with $S = 2$ has approximately the same amplitude as the one with $S = 1$ as it is mainly defined by the values of the dissipative parameters δ, ε and μ. However, they occupy a wider space in the (x, y)-plane, thus resulting in the higher values of their power, Q. Another difference from the case $S = 1$ is that the regions of existence in the ε-domain are shifted to smaller values of ε. This is due to the choice of the system parameters which are different from those presented in Fig. 3.16.

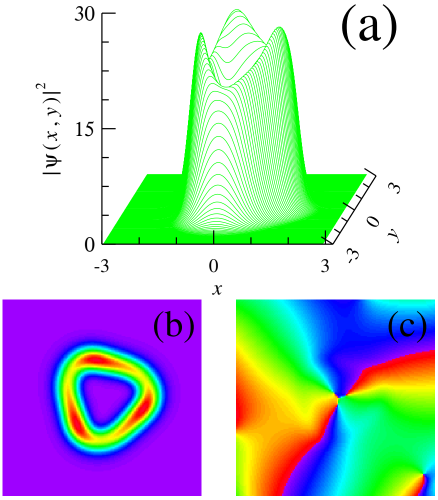

FIGURE 3.22: Radially asymmetric ring vortex soliton with $S = 2$. (a) 3D plot of the intensity profile. (b) Color contour plot of the same intensity profile in the transversal plane. (c) Color contour plot of the phase profile. The system parameters are chosen at the thick filled green circle in Fig. 3.21.

Radially asymmetric solitons on the blue curve are stable. An unstable branch may also exist. It would be natural for this curve to start as a bifurcation at the red curve. However, our numerical technique does not allow us to find these solutions. When changing ε and reaching the right hand side limit of the blue curve, we found a direct transformation of the radially asymmetric ring solitons into the radially symmetric solitons of the red branch. The reverse transformation occurs at the leftmost point of the red curve.

A remarkable feature of the radially asymmetric ring vortex soliton is a three-fold azimuthal bending symmetry along with the specific amplitude modulation. Namely, the number of maxima along the soliton ring is 3 rather than 2. The same type of modulation is observed for radially asymmetric ring solitons with $S = 1$ and $S = 3$. Namely, the number of maxima is equal to $S + 1$ (see below for the case $S = 3$). Clearly, the bending symmetry and the amplitude modulation are more related to the length of the ring rather than to its vorticity. In conservative systems, the ring structure can be split into a number of separate beams that depends on the ring diameter (Soto-Crespo et al., 1991). The latter is defined by the growth rate dependence on the spatial frequency of the modulation. In contrast to higher-order beams in conservative media, here, the modulation of the ring dissipative solitons is incomplete, and the ring structure of the soliton does not actually split it into separate beams.

3.4.3 Ring solitons with $S = 3$

The regions of existence of ring solitons with $S = 3$ are shown in Fig. 3.23. Although the radially symmetric ring solitons may have very similar curves for their regions of existence independent of S, their bifurcations into the radially asymmetric ring structures vary significantly with S. The color notations for the curves in Fig. 3.23 are the same as in the previous examples. In the case of $S = 3$, the stable radially asymmetric solutions are completely separated in the ε-domain from the stable radially symmetric solutions. Namely, the solid part of the red curve starts when the solid part of the blue curve ends, i.e. the radially symmetric solutions become unstable when the radially asymmetric solutions appear.

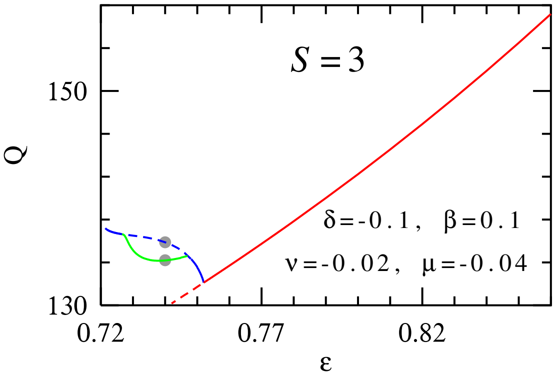

FIGURE 3.23: Regions of existence of vortex solitons with $S = 3$. The solid (dashed) red curve represents stable (unstable) radially symmetric solitons. The solid blue and green curves correspond to stable radially asymmetric ring solitons while the blue dashed curve stands for unstable ones.

All solutions presented in Fig. 3.23 have fixed power Q at any given ε. We did not find pulsating solitons in the region of ε shown in Fig. 3.23. The solitons of the branch colored in blue have four-fold bending symmetry. They become unstable when another type of solitons, completely asymmetric, appear. They are represented by the green branch. In this region, solitons with four-fold bending symmetry are unstable which is shown by a dashed blue line. The growth rate of the instability is small and this allows us to find them using our technique. Two illustrative examples of the solutions with $S = 3$ can be seen in Figs. 3.24(a) and (b). Figure 3.24 shows the intensity profiles of the two radially asymmetric solutions for $\varepsilon = 0.74$.

Each profile is modulated with four maxima and in Fig. 3.24 they might look similar to each other. The difference can be seen clearly from Figs. 3.25(a1) and 3.26(b1). While the solutions of the blue branch possess a four-fold azimuthal symmetry having roughly a square shape in the transverse plane, the solution

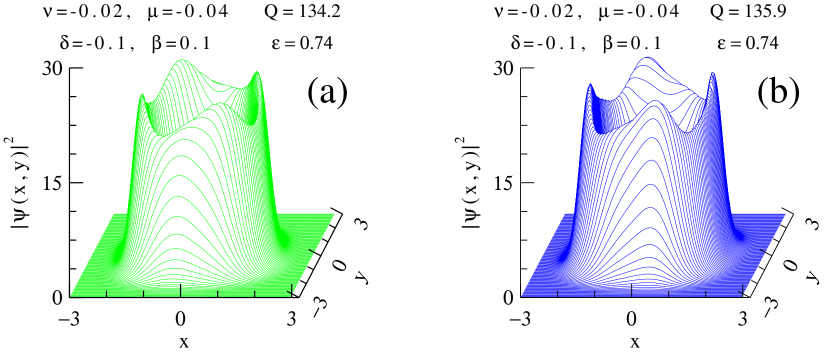

Figure 3.24: 3D intensity profiles of the radially asymmetric ring vortex solutions whose location in the parameter space is indicated in Fig. 3.23 by the gray filled circles. The two profiles belong to (a) the green and (b) the blue branches of solitons in Fig. 3.23 respectively. The green profile is stable while the blue one is slightly unstable and converges, on propagation, to the green one. The profile (b) has four-fold bending symmetry while the profile in (a) is completely asymmetric. Figs. 3.25 and 3.26 shows more clearly the difference between them.

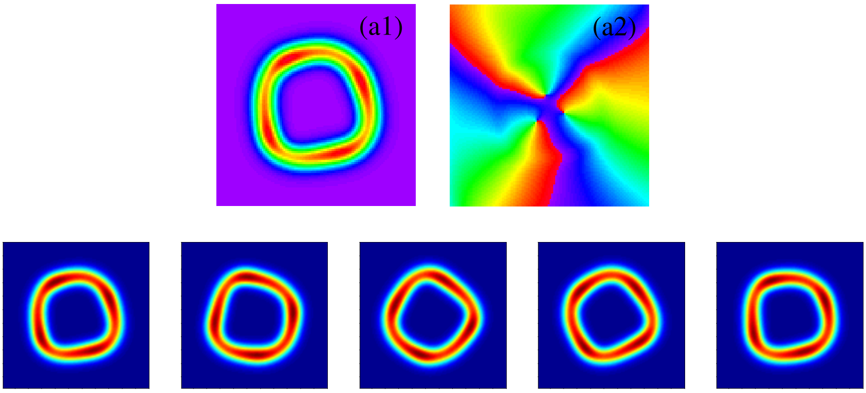

Figure 3.25: (Upper row) Color map plots of the intensity and phase profile of the ring soliton with $S = 3$ shown in Fig. 3.24(a) and corresponds to the lower grey filled circle in Fig. 3.23. (Lower row) Snapshots of dynamical evolution for this solution. The sequence corresponds with quarter-period of the clockwise rotation of this solution.

shown in green does not have that symmetry. The phase profiles corresponding to these solutions are shown in Figs. 3.25(a2) and 3.26(b2). The intensity evolution of the beam, in both cases, is recorded in the (lower row) associated snapshots sequence.

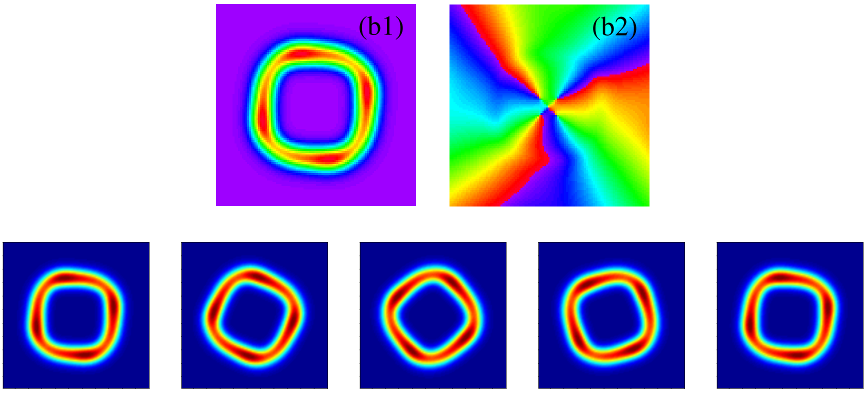

Figure 3.26: (Upper row) Color map plots of the intensity and phase profile of the ring soliton with $S = 3$ shown in Fig. 3.24(b) and corresponds to the upper grey filled circle in Fig. 3.23. (Lower row) Snapshots of dynamical evolution for this solution. The sequence corresponds with quarter-period of the clockwise rotation of this solution.

3.4.4 Ring solitons with $S = 4$

As the vorticity of the ring increases, so does the power of the solutions. This is basically because their diameter becomes larger while the width of the ring is kept essentially constant. Apart from that, the power versus ε diagrams for radially symmetric solitons look almost similar for all S. However, the transformations to solutions with broken symmetry become more complicated for higher values of S. Thus, the bifurcation diagrams are also becoming more complicated.

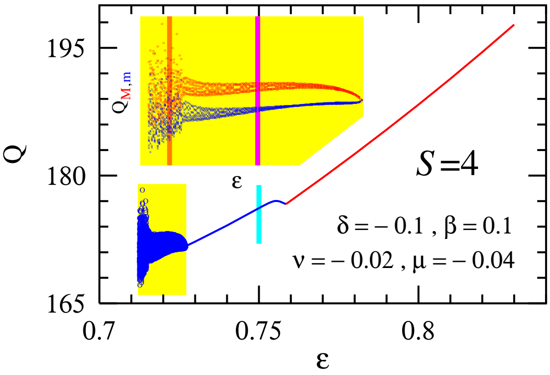

Figure 3.27: Bifurcation diagram for the ring vortex solitons with $S = 4$. The upper left yellow inset is a magnified part of the diagram in the lower small yellow box. In the inset, instead or representing the allowed values of Q on propagation, only maxima (red) and minima (blue) of $Q(z)$ are shown

Among the cases $S = 1, 2, 3$ and 4, we found the most complex bifurcation diagram for the case $S = 4$. It is shown in Fig. 3.27. As on the previous diagrams, the red line corresponds to the solutions with radial symmetry. The bifurcation into ring solitons with broken radial symmetry occurs at the edge of this range at $\varepsilon \approx 0.76$. The solid blue line corresponds to stable stationary solitons without radial symmetry.

For each ε, they have a fixed value of power Q. These solutions have a pentagonal shape close to the bifurcation point $\varepsilon \approx 0.76$. Five-fold symmetry disappears at lower values of ε and the shape of the solution becomes totally asymmetric. This is illustrated in Fig. 3.28. While the solution for $\varepsilon = 0.75$ (b), close to the bifurcation point still has approximately a pentagonal shape, the one for $\varepsilon = 0.73$ (a) does not have any particular symmetry. In each case, the ring has 5 intensity maxima.

Bifurcation into pulsating solitons occurs at $\varepsilon \approx 0.727$. This point corresponds to the right hand side limit of the lower little yellow box in Fig. 3.27. A magnified portion of this part of the bifurcation diagram is shown in the upper yellow inset of Fig. 3.27. In this inset, instead of representing the allowed values of Q, we show the maxima in red, Q_M, and minima Q_m, in blue, of the function $Q(z)$. These values are taken when they become fixed after the solution has converged to a pulsating soliton and any transitional behavior between the initial conditions and the final state has vanished. Oscillations occur with a single frequency when ε is close to the point of bifurcation. More frequencies appear at lower values of ε, thus resulting in wider stripes for maxima and minima. The motion becomes chaotic at ε around 0.715. Bifurcation into a chaotic pulsation results in two stripes mixed into a single wide band of Q values. In this example, we have a continuous transition into a chaotic state by increasing the number of frequencies involved in the dynamics rather than through a sequence of period doubling bifurcations (Akhmediev et al., 2001).

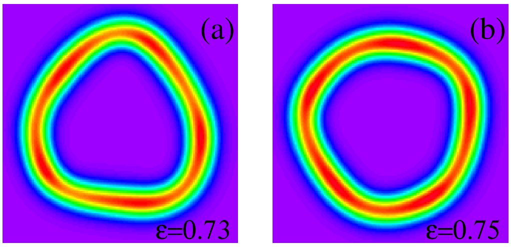

FIGURE 3.28: Two examples of radially asymmetric ring solitons with $S = 4$.

In order to show the multi-frequency dynamics of the oscillations of the ring solitons in the region of ε below 0.76, we present some illustrative $Q(z)$ curves in Fig. 3.29. These curves are plotted for the values of ε shown by the three vertical colored stripes in Fig. 3.27 (light blue, magenta and orange). The corresponding curves in Fig. 3.29 have the same colors. The light blue line with constant Q

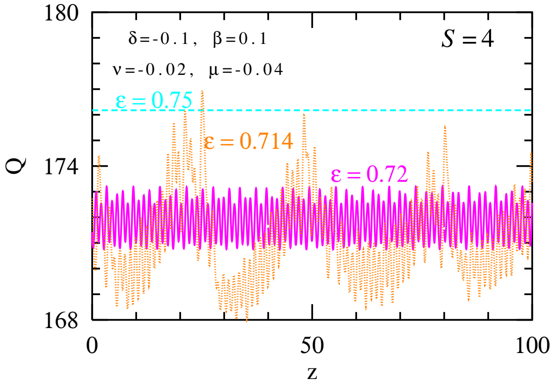

FIGURE 3.29: Evolution of Q for stationary (light blue curve), quasi-periodic pulsating (magenta) and chaotic (orange) vortex solitons. The colors correspond to the thick vertical lines in Fig. 3.27.

shows that the ring soliton at this ε has a fixed power despite the fact that the ring soliton has lost its radial symmetry. The curve in magenta shows a multi-frequency dynamics of a pulsating ring soliton. Finally, the orange curve shows a completely chaotic behavior of the solution at $\varepsilon = 0.72$. We should note that there can be intermediate bifurcations where new frequencies are added into the dynamics. However, the density of these bifurcations are high along the ε axis and cannot be well distinguished in our numerical simulations.

3.4.5 Ring solitons with $S = 9$

As it can be seen from Fig. 3.16, ring solitons have a wide range of existence which does not shrink with increasing the vorticity S. This fact allows us to conclude that ring solitons exist for any higher integer value of S. The fundamental mode always has radial symmetry. The modes which have lower symmetry bifurcate from the fundamental mode. Clearly we can present only a limited number of examples. Thus, to confirm the existence of ring solitons with higher values of S, we conclude this section with the case $S = 9$. Firstly, we confirmed that radially symmetric rings do exist in the region of parameters comparable in size with the regions for low values of S. Secondly, we have found the sequence of complicated bifurcations which are not shown here because of the extreme complexity of the bifurcation diagram. Instead, we present just one example of the ring soliton profile. Namely, we have chosen the case, which gained a few new striking features as a result of several bifurcations.

The first bifurcation is usually related to modulation instability. It creates a modulated structure along the ring with a number of maxima that can coincide with $S + 1$ but can also be different from that. In fact, in the case presented here (Fig. 3.30), the number of maxima does coincide with S. This modulated

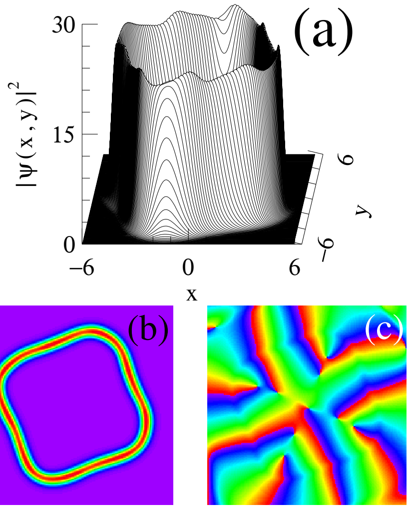

Figure 3.30: (a) Three-dimensional plot of the ring soliton with $S = 9$ for $\varepsilon = 0.745$. Color contour plots of (b) the intensity and (c) the phase of the same vortex dissipative soliton.

structure can be seen in Fig. 3.30(a). Another bifurcation results in the loss of radial symmetry and creates the bending structure. In the case shown in Fig. 3.30(b), the soliton still has four-fold bending symmetry. This can also be lost in subsequent bifurcations. However, what remains constant in all transformations is the vorticity S. The value $S = 9$ can easily be counted from the phase profile of the soliton in Fig. 3.30(c).

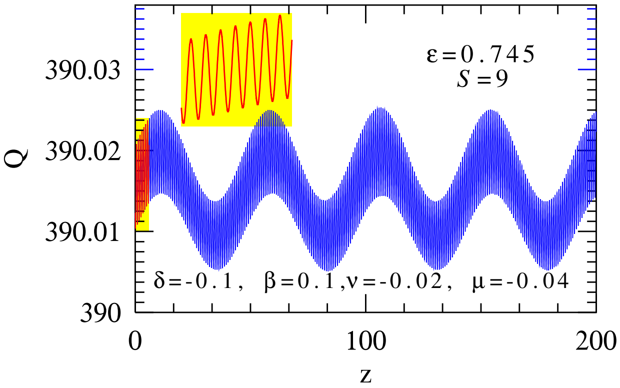

Figure 3.31: Double periodic evolution of Q vs z for vortex dissipative soliton with $S = 9$ (blue curve). The yellow inset on the top of the figure shows a magnified part of the blue curve enclosed into a small yellow box to the right of $z = 0$.

Subsequent bifurcations add oscillations into the structure, thus forcing the soliton to pulsate. After a set of bifurcations, the ring soliton with $S = 9$ becomes a pulsating solution with two frequencies. These two frequencies are clearly seen in Fig. 3.31 that shows evolution of Q along z for this pulsating solution. One of them is related to the fast rotation of the modulated structure clockwise around the ring. The lower frequency is related to the rotation of the four-fold azimuthally bended structure, Fig. 3.32(a), in the anti-clockwise direction. Fig. 3.32(b) show the nine maxima along the ring, only the field intensities that exceed the value 0.95 of the absolute maximum of the field intensity are shown. Each of the two frequencies appears as a result of a separate bifurcation similar to those presented in the diagrams for lower values of S. When increasing S however, the complexity of the bifurcation diagrams also increases. Nevertheless, the ring structure is preserved through all the bifurcations. The ring solitons gradually lose higher-order symmetries and become complicated both in shape and in its dynamics. As a final complication, the motion of the ring may become chaotic.

These features are characteristic for the ring solitons with values of S higher than 9. The radius of the ring increases with S but the amplitude of the ring stays the same. Thus, the power inside the ring increases roughly linearly with S. There is an infinite number of them but we have to limit ourselves to the lowest order ones. This last case concludes our presentation of the dissipative ring vortex solitons and their properties.

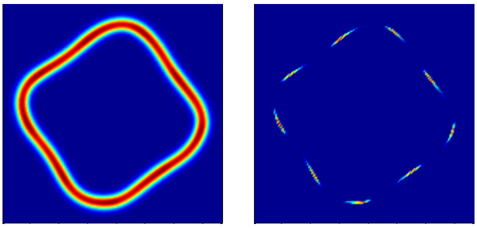

FIGURE 3.32: Color map plots with intensity profile for radially asymmetric rotating soliton with $S = 9$. (a) Dissipative vortex soliton with four-fold bending symmetry. (b) Nine maxima of the same solution.

3.5 Summary

We have analyzed the existence of two-dimensional beams and their evolution in dissipative continuous media. In particular we addressed the identification of subspaces, beyond the two main regions of existence of stable stationary beams with radial symmetry, where complex and exotic dynamics appear.

Close to the region of stable continuously self-focusing solitons (region I of ground state solitons) we have found several types of bifurcations. (1) Bifurcation into a stable stationary beam of elliptic shape. (2) Bifurcation into pulsating beams with harmonic pulsations or more complicated pulsations with highly involved shape evolution. Beams can be pulsating and rotating simultaneously. Near to the region of stable stationary continuously self-defocusing beams (region II of ground state solitons), the soliton keeps its radial symmetry after the bifurcation. Beams in this case are pulsating but stay radially symmetric. Pulsating beams can further be transformed into exploding ones, that loose the radial symmetry at the moment of the explosion but recover the original profile between the explosions.

In addition, we studied (2+1)D ring self-localized vortex structures. We have found regions of stability for ring solitons with vorticity S ranging from 1 to 5 and additionally for $S = 9$. They can also pulsate periodically or chaotically. Despite all these transformations, they remain stable as a single ring with given S.

"Y por amor a la memoria llevo sobre mi cara
la cara de mi padre (Yehuda Amijai)"
Hector Abad Faciolince - El Olvido que Seremos

4

Discrete Media Case

Self-localized structures, usually termed discrete solitons, have been predicted and observed for one- and two-dimensional nonlinear photonic lattices. In the previous decade, coherent structures were predicted (conservative cubic model) and experimentally obtained in studies of photorefractive crystals in nonlinear optics (Efremidis et al., 2002; Sukhorukov et al., 2003), and droplets of optical lattices in Bose-Einstein condensates (Cataliotti et al., 2001, 2003). Several patterns have been unveiled in lattices induced with a self-focusing nonlinearity, namely: discrete dipole (Yang et al., 2004b), quadrupole (Yang et al., 2004a), necklace (Yang et al., 2005) and discrete vortices (Fleischer et al., 2004; Neshev et al., 2004). Such structures have a definite potential to be used as carriers for data transmission and processing all-optical communication schemes.

By using different continuation methods, we unveil a wide region in the parameter space of the discrete complex cubic-quintic Ginzburg-Landau (CQGL) equation, where several families of stable vortex solitons coexist. All these stationary solutions have simultaneously two different topological charges for two different closed loops encircling, i.e., centered at, the singularity. Their regions of existence and stability were determined, and corroborated directly through propagation. We also discover the dynamical formation of a variety of "bound-state" solutions, composed of two or more of these vortex solitons. All of these stable composite structures persist in the conservative cubic limit, for high values of their power content. Additionally, we have analyzed the relationship between dissipation and stability for a number of solutions, finding that dissipation favors the stability of the vortex soliton solutions.

4.1 Introduction

The study of discrete systems has been a hot topic in the last years due both to its broad impact in diverse branches of science and its potential for technological applications (Vicencio et al., 2003; Campbell et al., 2004; Flach & Gorbach, 2008; Lederer et al., 2008). Nonlinear periodic structures offer alternative ways to control light propagation by modifying its diffraction properties through the modulation of its refractive index. For instance, periodic arrays of optical waveguides can create a novel kind of devices in which new types of spatial solitons can be generated and studied experimentally. The properties of spatially localized modes in a waveguide array are usually analyzed in the framework of a set of coupled-mode equations, each equation representing the soliton amplitude in a specific waveguide but coupled to the neighboring waveguides.

For instance, photonic crystals are structures of alternating refractive index that provide unprecedented control over light fields propagating through them; recent works show that lasers with square-lattices photonic crystal cavities posses enhanced functionality and performance when compared to conventional lasers (Altug et al., 2006). These systems can be analyzed in the framework of a set of coupled linear equations, which in solid-state physics is known as the *tight-binding* approximation, while in an optics context, it is known as the *coupled-mode* approach. This concept also appears in other contexts, such as the study of nonlinear dynamics of a Bose-Einstein condensate in optical lattices (Trombettoni & Smerzi, 2001). Stationary solutions obtained through this framework are called discrete solitons. In particular, discrete vortex solitons in conservative systems have been reported on several theoretical and experimental works (Malomed & Kevrekidis, 2001; Neshev et al., 2004; Arévalo, 2009; Desyatnikov et al., 2011), while dissipative discrete solitons have been found, analytically and numerically, in one dimensional waveguide arrays (Soto-Crespo et al., 2003; Maruno et al., 2005; Efremidis et al., 2007a).

In this chapter we report the finding of a wide region in the parameter space, of the discrete complex CQGL equation, where different discrete vortex solitons coexist. Almost all the individual solutions we examine in this chapter posses simultaneously two topological charges. We have studied their interactions and as a result the formation of bound states. In particular, we have found different families of these self-localized solutions. We studied their stability and found stable vortex families for $S = 1$, $S = 3$ (symmetric) and $S = 2$ (asymmetric) topological charges for the same set of equation parameters. In addition, we found novel solutions in which two topological charges coexist, such as solutions with swirl spatial configuration. They posses $S = 1$ and $S = 3$ topological charges simultaneously. Another kind of these vortex solutions posses $S = 2$ and $S = 6$ topological charges and its spatial configuration looks like a square rotated $\pi/4$ on the cartesian plane. Additionally, we have studied the formation and stability of bound states formed by at least two of those solutions described previously. We found here that the composite structure keeps the two topological charges feature, and increases its value.

Finally, we have selected some solutions of the whole set to analyze what happens when the dissipation is suppressed in the discrete complex CQGL equation. We have found that the stability regions shrink, and only solutions with high optical power remain stable.

4.2 Statement of the problem

Optical beam propagation in nonlinear, periodical two-dimensional waveguide arrays can be modeled by the following equation:

$$\begin{aligned} i\dot{\psi}_{m,n} + \hat{C}\psi_{m,n} + |\psi_{m,n}|^2\psi_{m,n} + \nu|\psi_{m,n}|^4\psi_{m,n} = \\ i\delta\psi_{m,n} + i\varepsilon|\psi_{m,n}|^2\psi_{m,n} + i\mu|\psi_{m,n}|^4\psi_{m,n} \ . \end{aligned} \tag{4.1}$$

Equation (4.1) is the discrete version of the complex CQGL model, Eq. (3.1), for continuous media analyzed in chapter (3). Here, $\psi_{m,n}$ is the complex field amplitude at the (m,n) lattice site and $\dot{\psi}_{m,n}$ denotes its first derivative with respect to the propagation coordinate z. The set

$$\{m = -M, ..., M\} \times \{n = -N, ..., N\},$$

defines the array, with $2M+1$ and $2N+1$ being the number of sites in the horizontal and vertical directions, respectively. The *tight binding* approximation establishes that the field propagating in each waveguide interacts linearly only with nearest-neighbor fields through their evanescent tails. This interaction is described by the discrete diffraction operator

$$\hat{C}\psi_{m,n} = C(\psi_{m+1,n} + \psi_{m-1,n} + \psi_{m,n+1} + \psi_{m,n-1}),$$

where C is a complex parameter. Its real part denotes the strength of the coupling between adjacent sites and its imaginary part denotes the gain or loss originated by this coupling. The nonlinear higher-order Kerr term is represented by ν while $\varepsilon > 0$ and $\mu < 0$ are the coefficients for cubic gain and quintic losses, respectively. Linear losses are accounted for a negative value of δ.

In contrast to the conservative discrete NLS equation, the optical power, defined as

$$Q(z) = \sum_{m,n=-M,-N}^{M,N} \psi_{m,n}(z)\psi^*_{m,n}(z) \ , \tag{4.2}$$

where ψ^* is the conjugate complex of ψ, is not a conserved quantity in the present model. Nevertheless, for a self-localized solution, the power and its evolution will be the main quantity that we will monitor in order to identify different families of stationary solutions.

We look for stationary solutions of Eq. (4.1) of the form $\psi_{m,n}(z) = \phi_{m,n}\exp(i\lambda z)$ where λ is real and $\phi_{m,n}$ are complex amplitudes. We are interested in solutions localized in space whose phase changes azimuthally by an integer number (S) of 2π along a discrete closed-circuit. In such a case, the self-localized solution is called a discrete vortex soliton (Pelinovsky et al., 2005) with vorticity S. By inserting the previous *ansatz* into Eq. (4.1) we obtain the following set of $(2M+1)\times(2N+1)$ algebraic coupled complex equations:

$$\begin{aligned} -\lambda\phi_{m,n} + \hat{C}\phi_{m,n} + |\phi_{m,n}|^2\phi_{m,n} + \nu|\phi_{m,n}|^4\phi_{m,n} = \\ i\delta\phi_{m,n} + i\varepsilon|\phi_{m,n}|^2\phi_{m,n} + i\mu|\phi_{m,n}|^4\phi_{m,n} \ . \end{aligned} \tag{4.3}$$

We solve Eq. (4.3) by using a multi-dimensional Newton-Raphson iterative algorithm (see appendix B). The method requires an initial guess that we construct as follows: In the high-confinement limit, single peak solutions (fundamental bright solitons) were predicted to exist in dissipative nonlinear media (Efremidis et al., 2002). From this limit, we can obtain the following approximation:

$$\phi_0^2 \approx -(\varepsilon + \sqrt{\varepsilon^2 - 4\mu\delta})/(2\mu), \quad \lambda \approx \phi_0^2 + \nu\phi_0^4, \quad \text{and} \quad \alpha \approx |C\phi_0/(\lambda + i\delta)|.$$

Here, ϕ_0 corresponds to the central amplitude, λ the nonlinear propagation constant, and α the first adjacent amplitudes. We can see that the amplitude of each peak is a function of ε, μ and δ; if we set the last two parameters, the amplitude takes a *bi*-quadratic form with ε as the bifurcation parameter. Now, we place a single peak approximation at each corner of a square sub-lattice L as a superposition of four fundamental bright solitons (Alexander et al., 2004):

$$L = \begin{bmatrix} 0 & \alpha & 0 & \alpha & 0 \\ \alpha & \phi_0 & \tilde{\alpha} & \phi_0 & \alpha \\ 0 & \tilde{\alpha} & 0 & \tilde{\alpha} & 0 \\ \alpha & \phi_0 & \tilde{\alpha} & \phi_0 & \alpha \\ 0 & \alpha & 0 & \alpha & 0 \end{bmatrix}, \tag{4.4}$$

where $\tilde{\alpha} = 2\alpha$. Now, we define a phase operator as $\Theta_{m,n} = \exp\left[i \arctan(-n/m)\right]$, and write our initial $S = 1$ *ansatz* as

$$\phi_{m,n} = L_{m,n} \cdot \Theta_{m,n} \ . \tag{4.5}$$

With this initial guess, we construct a family of 4-peaks symmetric vortex solitons with vorticity $S = 1$. Similar procedure is followed to find discrete vortex with $S = 2$ and $S = 3$. The stability for all the solutions reported in this chapter has been monitored through a linear stability analysis, and it will be described in the Appendix C. Additionally, we have corroborated the stability integrating the full model (4.1), with a fourh order Runge-Kutta scheme. Hereafter, we plot stable (unstable) solutions using solid (dashed) lines.

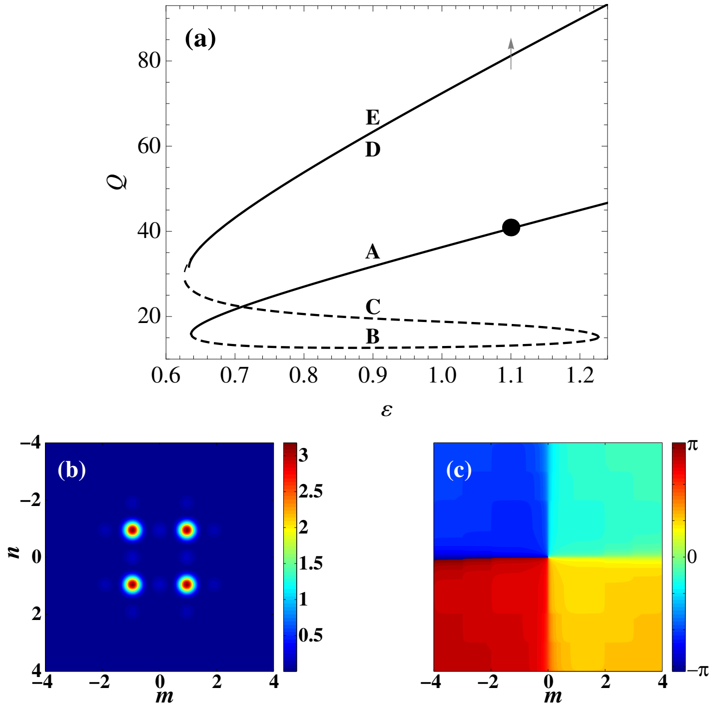

FIGURE 4.1: (a) Q versus ε diagram for discrete vortex solitons. Continuous and dashed lines correspond to stable and unstable solutions, respectively. (b) and (c) Color map plots for the amplitude and phase profiles, respectively, of the solution for $\varepsilon = 1.1$ indicated by a black dot in (a). $C = 0.8$, $\delta = -0.9$, $\mu = -0.1$, $\nu = 0.1$.

4.3 Fundamental and *swirl* vortex solitons

Using the *ansatz* (4.5) as an initial guess, we obtain a family of discrete vortex soliton with vorticity $S = 1$. Figure 4.1(a) shows a Q versus ε diagram for these solutions including their stability. This figure shows the coexistence, for the same set of parameters, of two different branches of stable solutions and, also, three different families of unstable solitons. Different families are successively connected by saddle-node bifurcation points. An example for a solution of branch A is shown in Figs. 4.1(b) and (c) (black dot in Fig. 4.1[a]).

This solution is very similar to our initial *ansatz* sketched in (4.5) with a full topological charge $S = 1$. This agreement validates the seed we constructed as a first approach to find stationary vortex-type solutions. As the nonlinear amplification is diminished, the stable branch **A** reaches a first saddle-node point for $\varepsilon \approx 0.637$. At this point, this family turns around and a new family emerges: the unstable branch labeled **B** . After that, two more saddle-node points appear connecting the new branches **B** with **C** and, then, **C** with **D**. The unstable

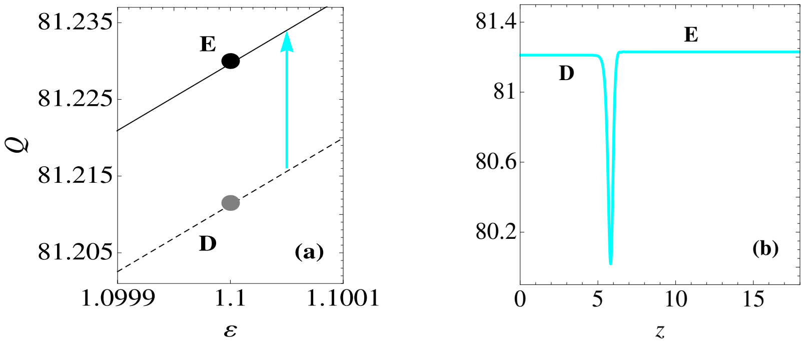

FIGURE 4.2: (a) Zoom of branches **D** and **E** for a narrow region around the gray arrow in the Fig. 4.1(a). (b) Numerical integration of Eq. (4.1) showing the power transition sketched by an cyan arrow in (a) for $\varepsilon = 1.1$.

branch **D** is mostly hidden because it is located at the same region that the stable branch labeled **E**. Branches **A-D** preserve the vorticity $S = 1$ while the amplitude profiles change adiabatically. It is worth mentioning that branches **A**, **D** and **E** also exist for higher ε values, with the power increasing monotonically, as the high-confinement limit predicts.

As it was said before, in Fig. 4.1(a), curves **D** and **E** are indistinguishable. In order to see their differences more clearly, we plot a zoom in Fig. 4.2(a) of region $Q \sim 81.2$ for a narrow region around the gray arrow in the Fig. 4.1(a). The first solution on branch **C** (black dot in Fig. 4.2[a]) was obtained dynamically; i.e., we numerically integrated Eq. (4.1) by using an unstable solution (gray dot in Fig. 4.2[a]) as initial condition. Contrary to previous observations, for the evolution of unstable vortex solitons (Leblond et al., 2009), we noticed that the power Q makes one oscillation and then stabilizes very rapidly around a new equilibrium value (see Fig. 4.2[b]). This new value was indeed very close to the initial one, but now it corresponds to a new stationary solution that propagates stably by keeping the same amplitude profile but a different phase structure. We took this new solution as an initial guess in our Newton-Raphson scheme and we constructed the whole stable branch **E** shown in Fig. 4.1(a).

The amplitude profile for solutions corresponding to the gray and black points at Fig. 4.2(a) is shown in Fig. 4.3(a). This profile is almost identical for both solutions and it corresponds to a new structure that we define as *swirl*-vortex soliton. However, both solutions have a quite different phase profile. The unstable solution (belonging to branch **D**) possesses a full phase profile with charge $S = 1$ (see Fig. 4.3[b]). A very interesting thing related with charges happens with the stable *swirl*-vortex soliton [see Fig. 4.3(c)]. For the first square contour [the innermost discrete square trajectory on the plane (n, m)] we can see that the vorticity has a $S = 1$ value, while for the next contours the vorticity has decreased to $S = -3$ ($S > 0$ [$S < 0$] means a clockwise phase

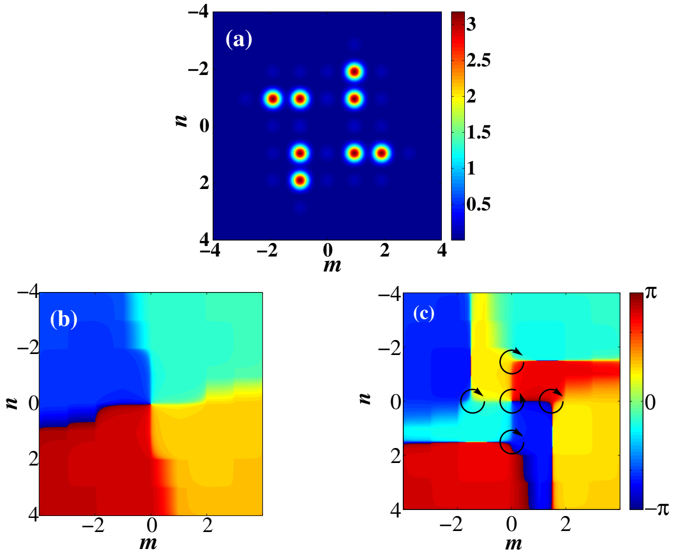

FIGURE 4.3: Color map plots for the solutions indicated with dots in Fig. 4.2(a). (a) Amplitude profile. (b) and (c) Phase profiles for the gray and the black points, respectively.

structure from $-\pi$ to π [π to $-\pi$]). Therefore, there is a stable coexistence of two different topological charges for the same mode. This new type of structure would correspond to a two-charges *swirl*-vortex soliton" and - as far as we know - this would be the first time they are predicted in nonlinear lattices. Moreover, this type of solutions can be understood as a bound state of five vortices (Chong et al., 2009; García-March et al., 2009). Indeed, we can identify a vortex with $S = 1$ at the origin (↺ symbol), surrounded by four vortex, each with $S = -1$, whose singularities are located at the center of the ↻ symbols on the Fig. 4.3(c). This interpretation agrees with the transition of the effective vorticity from $S = 1 \rightarrow S = -3$, as we move farther from the center.

To validate our phase definitions, we monitor $\sin(\theta_{m,n})$ vs φ for the first (Γ_1) -the innermost discrete square trajectory on the plane (m, n)- and the second (Γ_2) discrete contour. φ is the azimuthal angle for the lattice and $\theta_{m,n} = \arctan[\frac{\mathrm{Im}(\phi_{m.n})}{\mathrm{Re}(\phi_{m.n})}]$ is the phase of the field. From Fig. 4.4(a) we can see one period $(S = 1)$ for the sinusoidal function (gray line) along the first contour, and for the second contour we have three periods $(S = -3)$ as shown in Fig. 4.4(b). This constitutes an alternative proof of the different topological charges contained in any discrete vortex where, due to the small number of sites, it is not trivial to define the phases. Additionally, we used a linear interpolation in all profile figures to improve visualization.

Looking at the colormaps for the stable vortex soliton shown in Figs. 4.1(b)

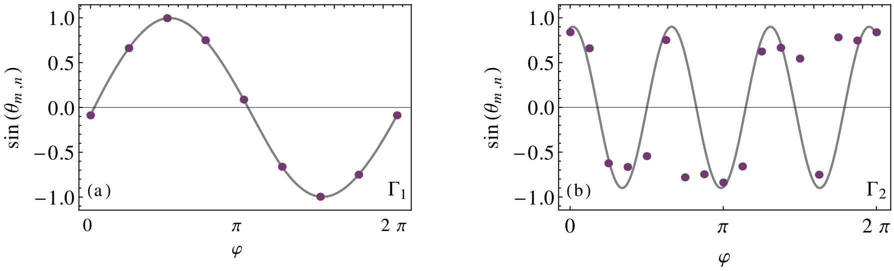

FIGURE 4.4: $\sin(\theta_{m,n})$ versus φ (azimuthal angle for the lattice) diagram for the first (a) and second (b) discrete contour for the *swirl*-vortex soliton, marked with a black dot on the **E** family in Fig. 4.2.

and (c) we can realize that amplitude and phase structures have the same reflection and rotation symmetries; similar happens in Figs. 4.3. As it was shown in previous works the stability for one solution with a high number of excited sites requires an increment of its topological charge (Pelinovsky et al., 2005; Terhalle et al., 2009). From this we understand why the dynamic evolution modifies the vorticity of our solutions. So, we may conclude that the instability for complex-structure solutions of charge $S = 1$ is essentially related to the geometric distribution and the number of excited sites.

4.3.1 Dynamical excitation

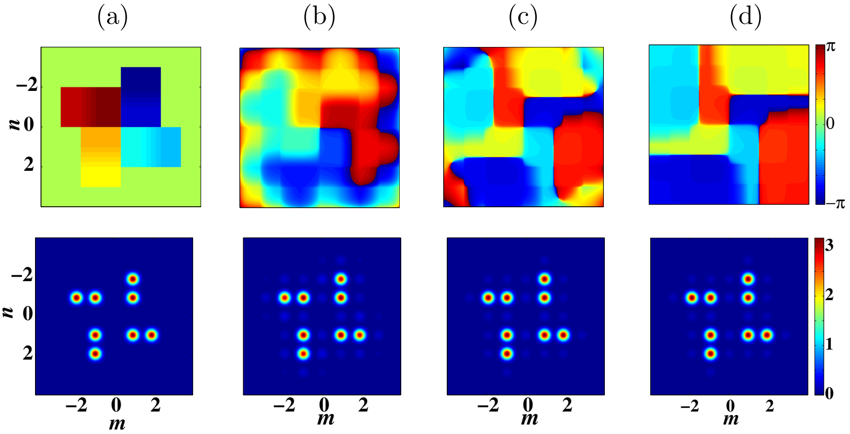

FIGURE 4.5: (Upper row) Color map plots of phase and (lower) amplitude profiles corresponding with different values of z marked by red points in Fig. 4.6

This example shows the robustness of our prediction and its chances to

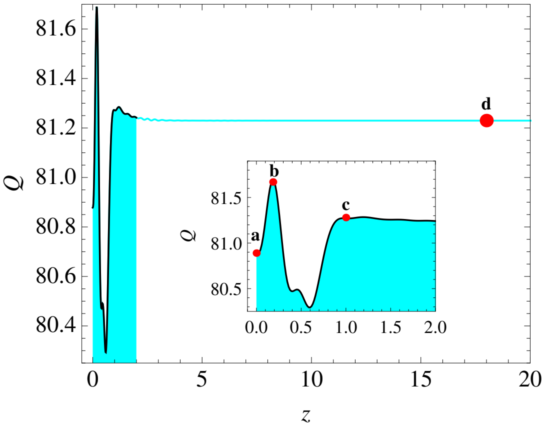

FIGURE 4.6: Evolution diagram of Q, for the initial condition displayed in Fig.4.5(a).

be observed in real dissipative systems because the initial condition could, in principle, be easily implemented in current experimental setups. Another very interesting point is that the system naturally evolves to a "two-charges" structure. Our initial condition has an unstable phase structure which guarantees decay to another type of mode, but not necessarily to the one we are interested in; it could perfectly well just be destroyed by the internal dynamics (Leblond et al., 2009). However, the system favors the excitation of a *swirl*-vortex solution which propagates stably for long propagation distances.

4.3.2 Dissipation and stability of the *swirl* vortex soliton

In this section, we are interested in analyzing how the stability of the solutions is affected when our model slowly goes to the Schrödinger limit, i.e when the value of the parameters in the discrete complex CQGL equation (4.1) tends to zero: $\{\delta, \varepsilon, \mu, \nu\} \to 0$. In particular, we will focus on the solution marked with a black dot on the **E** family in the inset of Fig. 4.2. The amplitude and phase profiles for this solution are displayed in Fig. 4.3(a) and (c).

Unlike the conservative cubic case (NLS equation), in the dissipative model the propagation constant λ is not an arbitrary parameter that can be chosen at will. It is fixed by the rest of the discrete complex CQGL equation parameters. By changing them, the value of the propagation constant also changes. As in other nonlinear problems with self-localization, e.g. the addressed by Soto-Crespo et al. (2000b), we can think of the dissipative terms as determinant to select one of the infinite solutions of the associated conservative problem. With this in mind we will find out the stability regions in terms of the propagation constant so we can compare with the Schrödinger limit.

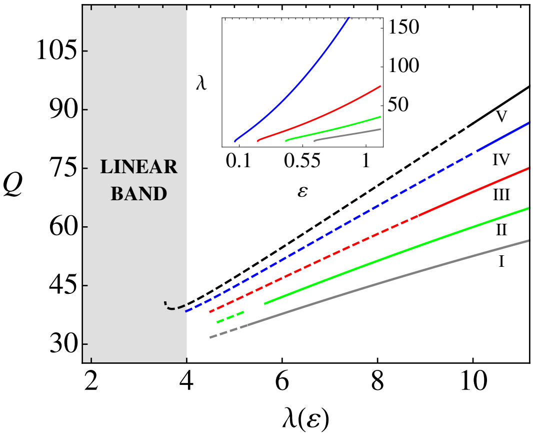

FIGURE 4.7: Q versus $\lambda(\varepsilon)$ diagram for several sets of parameters specified in Table I, of two charges *swirl*-vortex solitons. Inset shows λ vs ε.

For the sake of comparison we construct the Q versus λ diagram shown in Fig. 4.7. Here, we have fixed δ, μ and ν parameters and we only move through the ε parameter (nonlinear gain). In this way, we obtain a solution and its corresponding propagation constant for each value of ε. Then, we proceed to vary the rest of the parameters slightly, and construct a new curve, taking the solutions of the previous curve as initial conditions in our multidimensional Newton-Raphson scheme. In the inset of Fig. 4.7 we show the corresponding λ vs ε diagram.

TABLE 4.1: Discrete complex CQGL equation parameters

Curve	δ	μ	ν
I	-0.9	-0.1	0.1
II	-0.8	-0.08	0.08
III	-0.4	-0.03	0.03
IV	-0.1	-0.01	0.01
V	0	0	0

With the previous scheme we can find a large number of curves, but for the sake of clarity, we only show three of them; they are located between the conservative cubic case (black branch) and the **E** curve (gray branch). We can read from Table 4.1 the parameters of the discrete complex CQGL equation corresponding to the curves displayed in Fig. 4.7. These five branches belong to the same family composed of vortex solutions with amplitude and phase profiles such as those showed in Fig. 4.3. We have performed the standard linear stability analysis, described in appendix C, for each one of them. As announced at the end of section II, we use continuous (dashed) lines for stable (unstable) solutions.

Based on the above, we can clearly establish that if the dissipation is attenuated the stability regions for the soliton solutions are reduced (Soto-Crespo et al., 2000b). Indeed, we can see here a large difference between the stability regions for the Schrödinger limit and the **E** branch. The first one only has stable solutions for propagation constant values far away from the linear band, the last one has stable solutions for propagation constant values closer to the linear band.

4.4 Double and triple-charge vortex solitons

Equation (4.1) has a five-dimensional parameter space, namely $C, \delta, \varepsilon, \mu, \nu$. In order to look for any stationary solution, we need to choose first a fixed set of values for these parameters, and then an initial condition. By starting from a guess with eight peaks surrounding the central site - the first discrete contour of the lattice around of $(m, n) = (0, 0)$- with a topological charge $S = 3$ sampled on this path, the iterative algorithm rapidly converges to a stationary structure with the same features of the initial guess. Once we found a stationary solution with the desired properties, we use it as initial condition to find the corresponding solution for a slightly different set of equation parameters. Usually, we change just one of them. Therefore, for the dissipative case we construct families of solutions by fixing four parameters and varying the fifth one, usually the gain parameter, ε.

Using this procedure, we have constructed the σ_1 family (displayed as the curve Q versus ε in Fig. 4.9). We started from a highly localized solution and

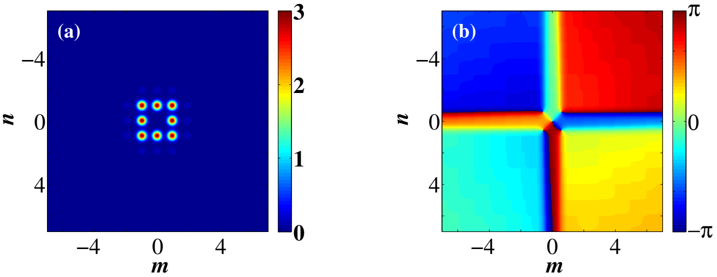

FIGURE 4.8: Color map plots for the eight peaks stable vortex solution with $S = 3$, marked with a green dot on the σ_1 family branch in Fig. 4.9. (a) Amplitude profile. (b) Phase profile.

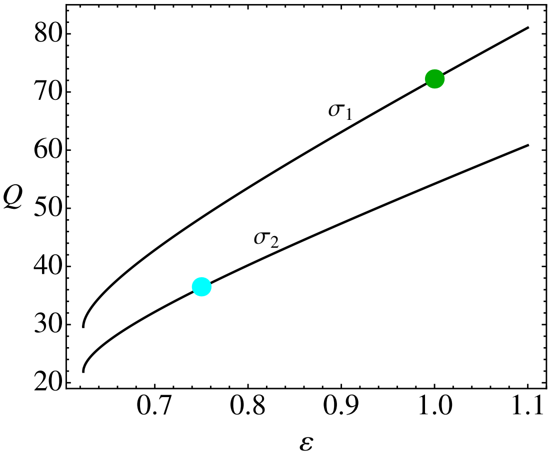

FIGURE 4.9: Q versus ε diagram for families σ_1 and σ_2 of discrete dissipative vortex solitons. (Discrete complex CQGL equation parameters: $C = 0.8$, $\delta = -0.9$, $\mu = -0.1$, $\nu = 0.1$).

we slowly decreased the nonlinear gain, observing that the solution became gradually more and more extended as ε (and Q) decreased. More specifically, the values for Q on this family diminish parabolically reaching the saddle-node point at $\varepsilon \approx 0.62$, where the curve turns around and a new, unstable family emerges. Similar behavior was reported in reference (Efremidis et al., 2007a) for dissipative bright solitons.

Figure 4.8 shows the amplitude and phase profiles corresponding to the solution marked with a green dot on the σ_1 family in Fig. 4.9. From the amplitude profile, Fig. 4.8(a), we can see how the stationary solution maintains the eight excited peaks of the initial seed. Besides, we can see some energy in the tails, i.e. on the second discrete contour. On the other hand, the phase profile, Fig. 4.8(b), shows a topological charge $S = 3$.

A similar procedure has been done to construct another family, labeled σ_2 (See Fig. 4.9). This family consists of asymmetric stationary solutions characterized for having six peaks located on the corners of an elongated hexagon in the n-axis direction of the lattice. This spatial configuration possesses a topological charge $S = 2$. Typical amplitude and phase profiles for this kind of solution are shown as color maps in Fig. 4.10. In the conservative case, four peaks structures have been reported to be stable (Pelinovsky et al., 2005) for $S = 1$ and unstable for $S = 2$; on the other hand, for hexagonal lattices, six peak structures are stable (Terhalle et al., 2009) for $S = 2$ and unstable for $S = 1$. In continuous systems assymetric four peaks structures has been found stable for $S = 1$ (Alexander et al., 2004).

The families σ_1 and σ_2 of stationary vortex solutions coexist for the same

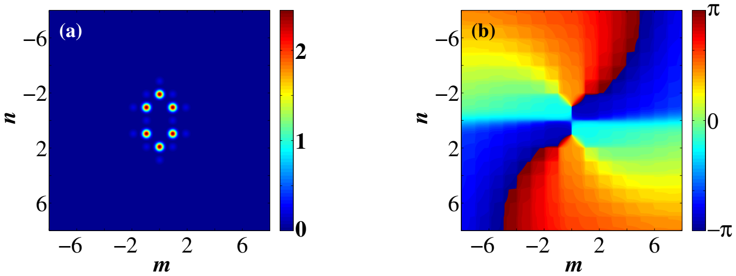

FIGURE 4.10: Color map plots for the six peaks stable vortex solution with $S = 2$ marked with a cyan dot on the σ_2 family branch in Fig. 4.9. (a) Amplitude profile. (b) Phase profile.

set of parameters of the discrete complex CQGL equation. Other families of solutions exist too for the same set of parameters.

4.5 “Two charges” vortex soliton

We show now another example where two topological charges coexist in the same solution. Let us start with a guess solution consisting of twenty peaks, spatially distributed like a rhombus, and with a topological charge $S = 2$. Using it as the starting point for the Newton-Raphson algorithm, we find a stationary solution that looks like the one shown in Fig. 4.11(a) and (b).

This solution belongs to the family displayed in Fig. 4.12 labeled with σ_3; it was constructed following the same procedure described in the previous section. Unlike the previous families, the σ_3 family does not reach the saddle node point *via* a monotonic decreasing of its power; rather, it passes through a minimum value ($\varepsilon \approx 0.64$), then, the power grows and finally, the saddle node point is

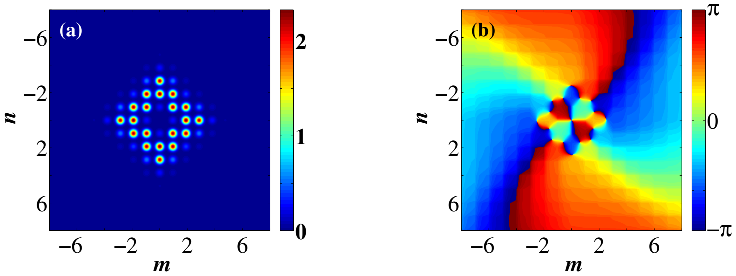

FIGURE 4.11: Color map plots for the twenty peaks stable two charges ($S = 2$ and $S = 6$) vortex solution, marked with a green dot on the σ_2 family in Fig. 4.9. (a) Amplitude profile. (b) Phase profile.

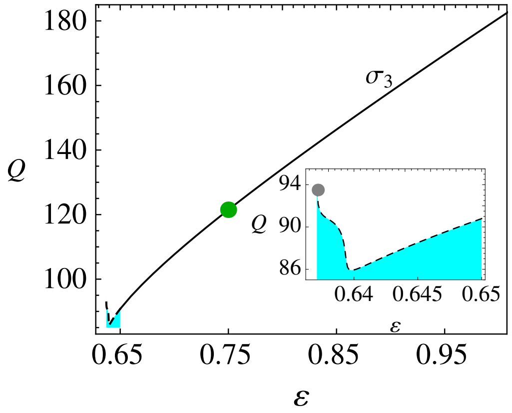

FIGURE 4.12: Q versus ε diagram for "two charges" ($S = 2$ and $S = 6$) discrete vortex solitons. Continuous and dashed lines correspond to stable and unstable solutions, respectively. The green dot on the σ_3 family corresponds to the profiles shown in Fig. 4.11.

reached (See inset in Fig. 4.12). The solutions of this family present a very interesting property related to its topological charge. The first square contour, Γ_1, -the innermost discrete square trajectory on the plane (m, n)- in Fig. 4.11(b) shows that the vorticity has a value $S = 2$. For the second contour Γ_2 we observe that the topological charge has changed to $S = 6$. Looking at the remaining contours, we note that the topological charge returns to $S = 2$, so, we can talk about a transition of the effective vorticity from $S = 2 \to S = 6 \to S = 2$, as we move farther from the center. For this reason, we can say that the stable solutions of this family possess two topological charges.

For the sake of clarity, we plot $\sin(\theta_{m,n})$ vs φ, the azimuthal angle for the lattice, for the first and second discrete contours. From Fig. 4.13(a) we can see

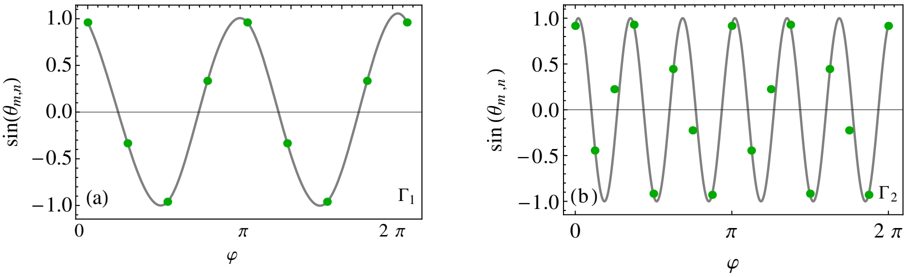

FIGURE 4.13: $\sin(\theta_{m,n})$ versus φ (azimuthal angle for the lattice) diagram for the first (a) and second (b) discrete contour for the vortex soliton, marked with a green dot on the σ_3 family in Fig. 4.12

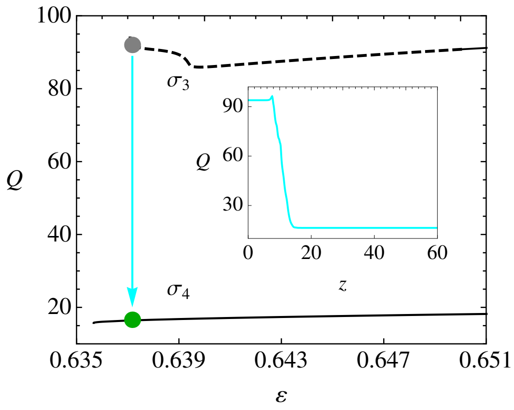

FIGURE 4.14: Q versus ε diagram showing the transition from the unstable solution marked with the gray dot to the stable solution marked with the green dot; the inset shows the power evolution for this transition.

that the data (green points) are perfectly fitted by the sinusoidal function (gray line) with two periods ($S = 2$) along the first contour, and for the second contour we have six periods ($S = 6$) as shown in Fig. 4.13(b). This shows explicitly the different topological charges contained in the solution, and it also proves that the discrete vortex is a well defined structure.

Figure 4.12 also shows that the σ_3 family has one large stable region and another small region, magnified in the inset, where the solutions are unstable. These unstable structures decay on propagation to another kind of stable solutions having less energy, $S = 2$ vorticity, and different amplitude profile with only four peaks. In particular, Fig. 4.14 illustrates how the unstable solution marked with a gray point (the saddle-node point for the σ_3 family in the Fig. 4.11) decays, by means of a radiative process shown in the inset, to the stable solution marked with a green dot on the σ_4 family. The amplitude and phase profiles showed in Figs. 4.15(a) and (b) and Figs. 4.15(c) and (d) correspond to the unstable and stable solutions marked with gray and green dots, respectively, in Fig. 4.14.

4.6 Multiplicity of stable vortex soliton families

As stated above, the nonlinear gain in the system is mainly controlled by ε; this parameter will be the only one that we will change in our simulations. Once we find a stationary solution - for a fixed set of parameters -, we compute its linear stability, and then change the parameters slightly and find the new solution using the previous one as an *ansatz*. In this manner we obtain all the solution families displayed in the Q vs ε diagram shown in Fig. (4.16). The first

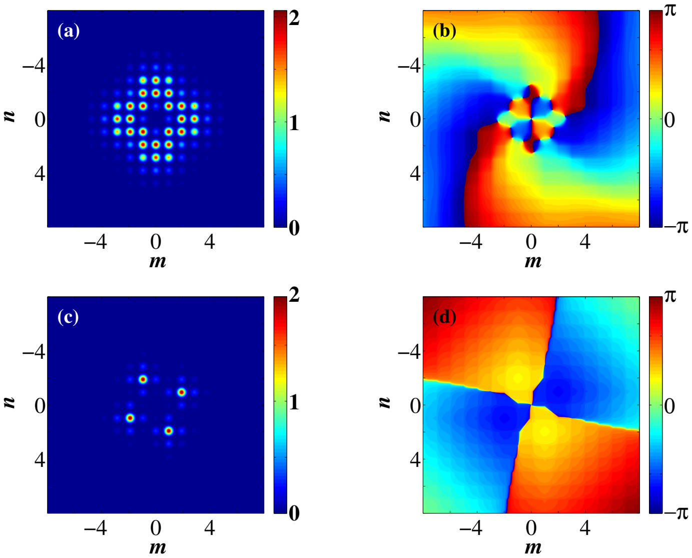

FIGURE 4.15: Color map plots for discrete dissipative solitons. (a) Amplitude profile and (b) phase profile for the unstable twenty peaks-vortex solution localized on the σ_3 family at the gray dot in the Fig. 4.14. (c) Amplitude profile and (d) phase profile for the four-peaks soliton solution localized on the σ_4 family at the green dot in the Fig. 4.14

of them (**E**-family), was already studied before (Sec 4.3). It was obtained by starting from the fundamental four-peaks discrete vortex soliton with $S = 1$, after passing throughout several saddle-node points. A striking property of all the solutions shown in Fig. (4.16) is that they have - simultaneously - two topological charges; i.e., they are two-charge vortices. Representative amplitude and phase profiles for these families are shown in Fig. (4.17).

Stable families **F**, **G**, **H** and **I** - shown in Figs. (4.16) and (4.17) - were unveiled after observing the dynamical evolution of solutions belonging to unstable branches (dashed gray lines). In some cases, the stable and unstable families are so close that they are nearly indistinguishable at the scale of Fig. (4.16). From the amplitude profiles we can see that there is a difference of four excited sites between one stable family and the next one. Family **E** has eight main excited sites and family **I** has twenty four main peaks. All these families show a coexistence of two topological charges.

The amplitude profile for case (**E**) shows a swirl spatial configuration. From its phase profile we can identify a topological charge $S = 1$ in the core - the most inner discrete contour - and a charge $S = -3$ away from the center. The phase profiles for families **F**, **G**, **H** and **I** show a topological charge $S = -3$ in the core of these solutions. From **F** to **G**, the topological charge has the

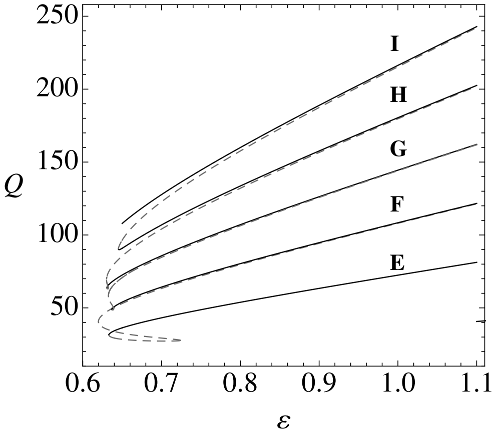

FIGURE 4.16: Q versus ε diagram for several vortex interconnected soliton families. Solid lines correspond to stable families while dashed lines to unstable ones. (Discrete complex CQGL equation parameters: $C = 0.8$, $\delta = -0.9$, $\mu = -0.1$, $\nu = 0.1$).

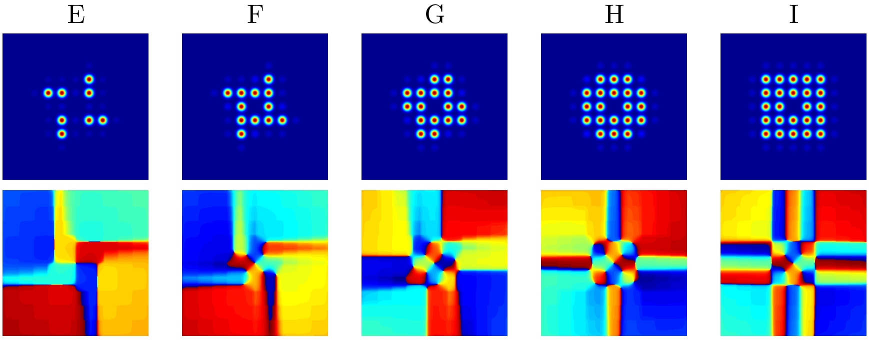

FIGURE 4.17: Color map plots for the amplitude (top) and phase (bottom) profiles of stable vortex solutions for the families marked in Fig. (4.16).

same value in the core and away from there, but the phase profile outside looks rotated respect to the center. For the last family, **I**, the topological charge has increased up to $S = -7$ away from the center.

4.7 Composite structures

Next, we study the formation of bound states composed of two vortex solitons belonging to the family **I** with $\varepsilon = 0.9$. We have chosen this family due to his high value of vorticity and squared symmetry equivalent to that of the optical lattice. We analyze dynamically the evolution of an initial condition composed

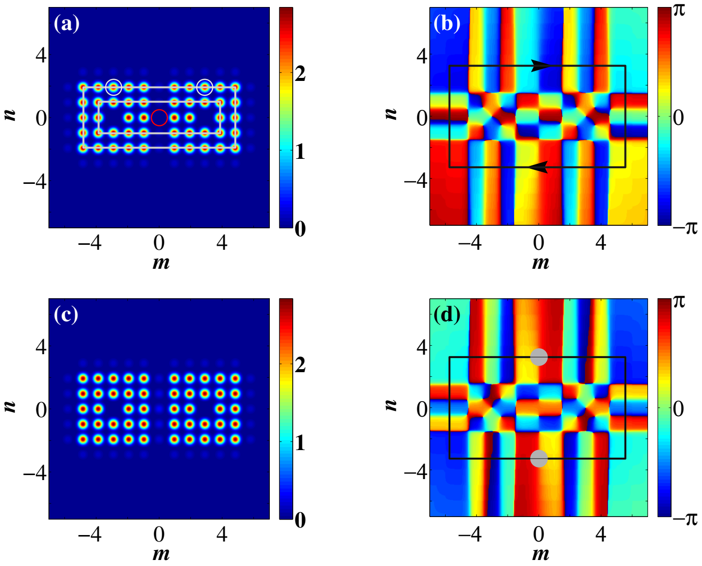

FIGURE 4.18: Color map plots showing the amplitude and phase profiles for the stable solutions corresponding with the basins of attraction shown in Fig. 4.19. For basins $\mathbf{b1}^{\leftrightarrow}$ the stable vortex soliton is similar to the profiles shown in (a) and (b). Profiles for the **b2** basin looks slightly different and are shown in (c) and (d).

by two of these solutions, horizontally shifted by a certain small distance. We tested two initial configurations differing in their initial separation and, for each one of them we try a broad range of initial phase differences, following a procedure similar to the one implemented by Akhmediev et al. (1997). For this purpose, we multiply the second solution by a phase factor $e^{i\theta_\alpha}$, where $\theta_\alpha \equiv \frac{\pi}{20}\alpha$, with $\alpha = 1, 2, ..., 40$. A bound state is reached when the relative phase ($\Delta\theta$, defined as the phase difference between two given sites in each solution) becomes a constant. In continuous and homogeneous systems, the separation distance also changes along the evolution and it becomes a constant when the bound state is formed. Here, in the dissipative discrete case we do not observe any soliton mobility and, therefore, the separation distance remains invariant.

We have measured the phase difference, in both configurations, for the sites enclosed by the white circles showed in Fig. 4.18(a). Figures. 4.19(a) and (b) show $\Delta\theta$ and Q versus z, respectively, for the first configuration shown in Fig. 4.18(a). We clearly identify two attraction basins, labeled as $\mathbf{b1}^{\leftarrow}$ and $\mathbf{b1}^{\rightarrow}$. Both ($\mathbf{b1}^{\leftrightarrow}$) correspond to the lower power value shown in Fig. 4.19(b). This implies that both basins are symmetrically equivalent solutions. The unstable configuration is labeled as **b2** and it corresponds to the upper power value in Fig. 4.19(b) (Figs. 4.18[c] and [d] show the amplitude and phase profiles of this unstable solution).

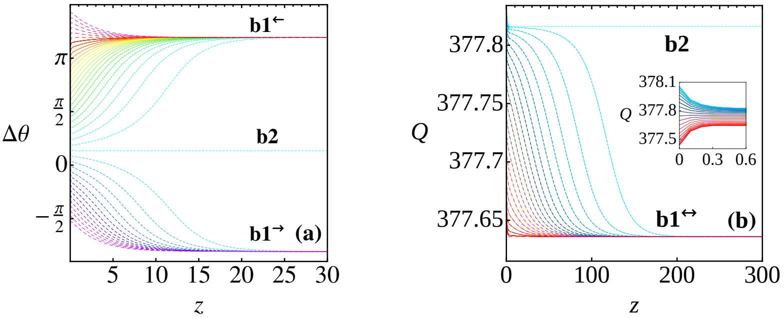

FIGURE 4.19: (a) Dynamic evolution of the relative phase between the two sites enclosed by the white circles in the vortex solutions shown in Fig. 4.18. (b) Optical power evolution for the same vortex solutions. The inset in (b) shows a magnification of the initial stage of evolution.

All these solutions preserve the central core structure, keeping the same topological charge as the initial input condition. Figure 4.18(a) and (c) show the amplitude profile for both of them; although they are very similar, the first one has an extra central core (marked by a red circle), located at the center of the structure. For the second structure we can note that the column in the middle ($m = 0$) is filled by small tails, without a central core. By taking a closed look at the rectangular contour sketched in Fig. 4.18(b), we find that the phase varies continuously. The charge increases in the direction indicated by the arrows in this contour, with an accumulated charge of $S = 11$.

On the other hand, if we look how the phase changes along the rectangle sketched in Fig. 4.18(d), we see that the topological charge is not well defined on this contour. Indeed, the topological charge is truncated (see gray filled circles) meaning that this structure is not a composite vortex beam. Nevertheless, this profile can be thought as two non-interacting vortex solitons with a π radians rotation between them. As we can see from Fig. 4.19(a), any small variation in

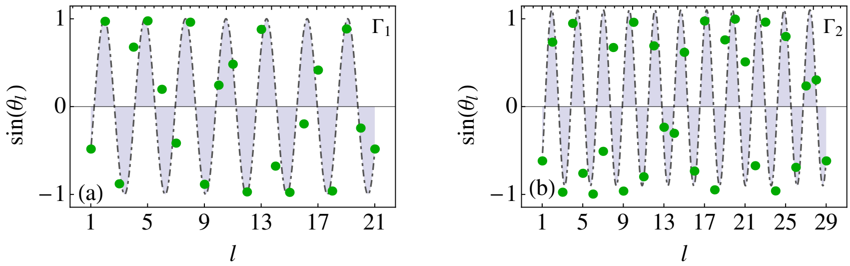

FIGURE 4.20: $\sin(\theta_l)$ versus l (site number) diagram for the first (a) and second (b) discrete contours, of the bound state vortex soliton, displayed on Fig. 4.18(a).

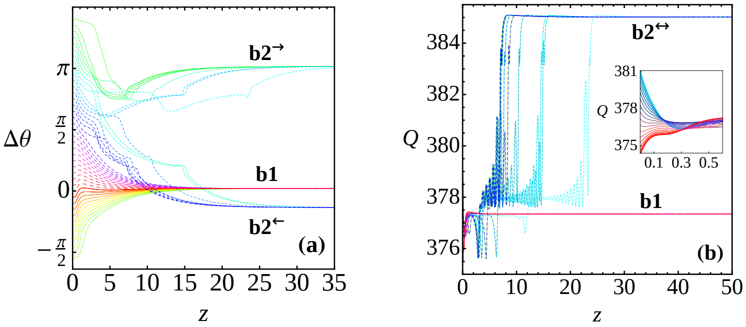

FIGURE 4.21: (a) Dynamic evolution of the relative phase between two sites enclosed by the white circles, on the bound states showed in Fig. (4.22). (b) optical power evolution for the same bound state. The inset in (b) shows a magnification of the initial stage of evolution.

the phase leads to this bound solution to evolve towards the basin of attraction $\mathbf{b1}^{\leftrightarrow}$. No other initial condition goes to **b2**, meaning that this is not properly a basin of attraction. So, we can say that vorticity is a necessary condition, achieved during the propagation, for the stability of this kind of structures.

For the sake of clarity, we plot $\sin(\theta_l)$ vs l, where l corresponds to the site on the inner (Γ_1) and outer (Γ_2) discrete contours sketched in Fig. 4.18(a). Figure 4.20(a) shows a good correspondence between the data (green points) and a sinusoidal function (gray line) with seven periods ($S = 7$) along the twenty one sites of the Γ_1 contour. For the Γ_2 contour, which contains twenty nine sites, we count eleven periods ($S = 11$) as shown in Fig. 4.20(b). Figure 4.20 explicitly shows the different topological charges contained simultaneously in this solution. This supports the right identification of discrete vortex solitons, which is not an easy task for discrete systems.

We consider now a second initial configuration where the two initially independent **I**-family vortices are placed closer to each other. We find a similar evolution than before but now, there are three different stable attraction basins for the relative phase evolution (see Fig. 4.21[a]). Two of them, the lowest ($\mathbf{b2}^{\leftarrow}$) and the highest ($\mathbf{b1}^{\rightarrow}$), correspond to the larger Q-value basin ($\mathbf{b2}^{\leftrightarrow}$ in Fig. 4.21[b]). The amplitude and phase profiles for these two vortices solutions are shown in Figs. 4.22(a) and (b), and (c) and (d), respectively. We can see from the amplitude profiles that these solutions lost one of the two original central cores (both solutions are equivalent if we perform a inversion symmetry through the $\hat{n}$-axis). The global vorticity is lost, and we can see from Figs. 4.22(b) and (d) how the phase circulation is truncated when we move to the region without a core. Here, we claim that this mixed bound state is composed of an **I**-family vortex soliton and a staggered bright soliton (with a π-phase shift between nearest neighbors).

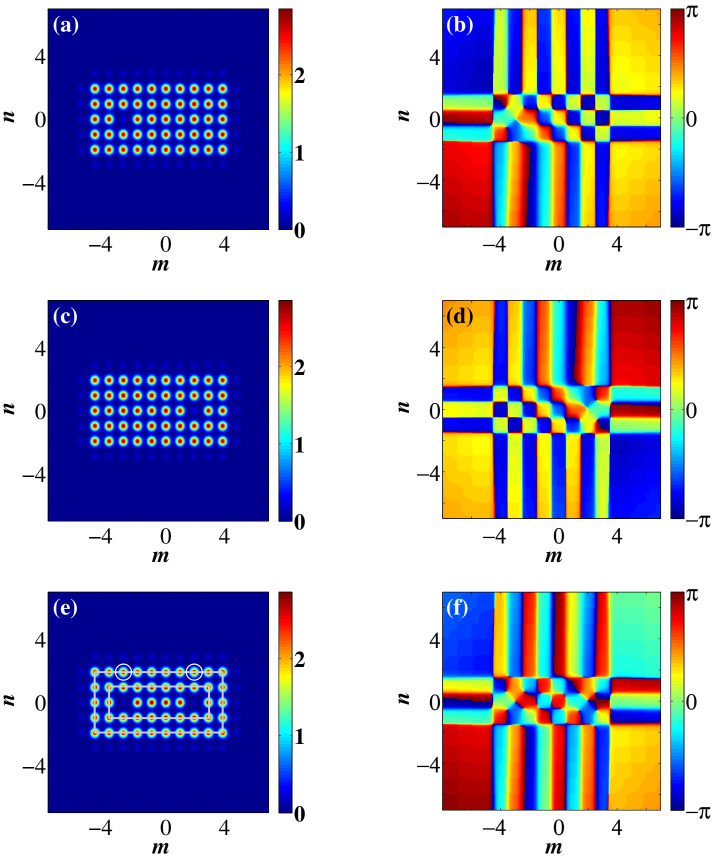

FIGURE 4.22: Color map plots showing the amplitude (left) and phase (right) profiles for the stable solutions corresponding with the basins of attraction showed in Fig. 4.21. For basin $\mathbf{b2}^{\leftarrow}$ the stable structure is similar to the profiles shown in (a) and (b), while (c) and (d) correspond with $\mathbf{b2}^{\rightarrow}$. For the remaining $b1$ basin, the vortex soliton is similar to the profiles shown in (e) and (f).

The third basin (**b1**), which corresponds to the lower Q-value basin in Fig. 4.21(b), has the amplitude and phase profiles displayed in Figs. 4.22(e) and (f). We clearly see that it preserves the initial two central cores keeping the same topological charge as the initial condition. Unlike the previous two basins, the global topological charge of this solution is well-defined. As for the first configuration, there are also two different topological charges for this composite vortex soliton. Again, to corroborate this, we plot $\sin(\theta_l)$ vs l in order to show in detail the topological charge along two different contours. The first one, Γ_3, corresponds to the inner rectangular contour sketched in Fig. 4.22(e),

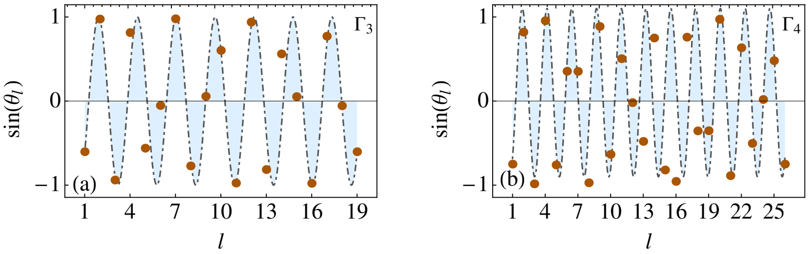

FIGURE 4.23: $\sin(\theta_l)$ vs l (site number) diagram for the first (a) and second (b) discrete contours shown on the Fig. 4.21(a) for the bound state vortex soliton.

while Γ_4 corresponds with the outer rectangular contour sketched in the same figure. Figure 4.23(a) shows how the inner charge is $S = 7$ while Fig. 4.23(b) indicates a charge $S = 11$ for contour Γ_4.

We show now two more examples of composite structures built from an initial superposition of two-and four solutions taken from the **H** and **I** families shown in Fig. 4.16. In both cases, the values of the parameters used are: $C = 0.8$, $\delta = -0.9$, $\varepsilon = 0.9$, $\mu = -0.1$ and $\nu = 0.1$. The typical propagation distance was $z \approx 300$, enough for the power content to become constant.

Figure 4.24 shows three stable solutions obtained by superposing two vortex solitons belonging to the **H**-family in Fig. 4.16. The first one is constructed by overlapping two of these vortices spaced by one site between their central cores. Figs. 4.24(a) and (b) show the amplitude and phase profiles for this stable solution. We note that this state has only one central core, located halfway between the initial ones. On the other hand, the phase profile shows a charge $S = 5$ at the inner contour and rotated with respect to the next discrete contours.

The next configuration is constructed in the same manner as the previous one, but now, the center-to-center distance between the cores has been increased to two sites. Figure 4.24(c) shows a dynamically stable solution with two central cores located at the same positions as the initial condition. The phase profile (see Fig. 4.24[d]) shows a value of $S = 5$ for the topological charge, as in the previous case.

A third stable composite structure is obtained by superposing again two vortex solitons with an initial center-to-center distance of three sites. The amplitude profile for the new dynamically stable solution has one horizontally elongated core, along two lattice sites, as shown in Fig. 4.24(e), and its topological charge has two different values as shown in Fig. 4.24(f). Indeed, the innermost discrete contour exhibits a charge $S = 6$, while the remaining contours have a charge $S = 10$.

Finally, we show another example of a composite structure that was obtained by combining four solutions belonging to the **I** family . We locate each **I**-vortex by placing their central cores forming the vertices of a 8×8 square. We use this

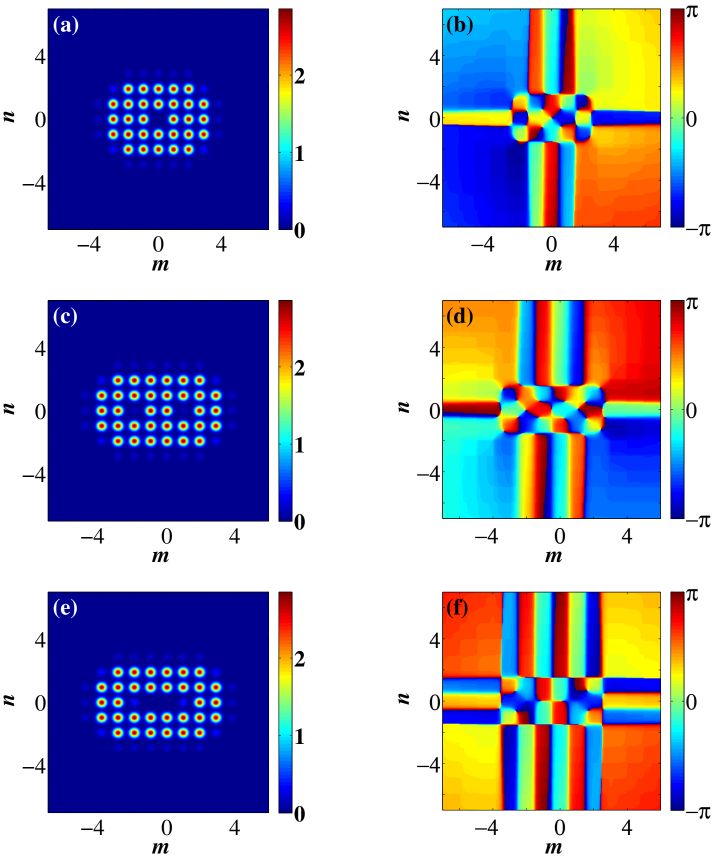

FIGURE 4.24: (Left) Color map plots showing the amplitude and (right) phase profiles for three stable vortex solutions obtained by superposing two vortex solitons belonging to the **H** family, at different initial distances.

configuration as initial condition for model (4.1) and find a dynamically stable stationary solution.

Figs. 4.25(a) and (b) show the amplitude and phase profiles for this composite solution. We observe a spatial amplitude distribution similar to the initial condition, where the four initial cores preserve their initial position and vorticity. In addition, an extra phase core appears at the lattice center $(n, m = 0)$, around which a $S = -1$ topological charge can be observed. If we follow a new contour that encloses all the sites with large amplitude, the topological charge measured will be $S = 15$.

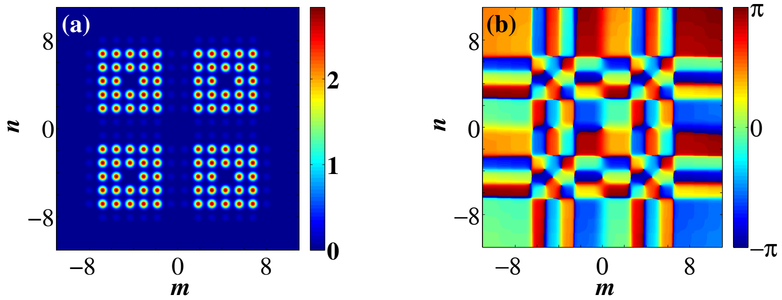

FIGURE 4.25: Color map plots for the amplitude (a) and phase (b) profiles for a dynamically stable solution obtained by combining four solutions belonging to the **I** family.

4.7.1 Schrödinger limit

Most of the present experiments with optical beams are performed under conditions that closely meet the cubic conservative limit. So, we are interested in knowing if all these previous dissipative structures can be observed also here. In this scenario, all the parameters of the discrete complex CQGL equation are suppressed, i.e., $\nu = \mu = \varepsilon = \delta = 0$, and model (4.3) reduces to the discrete NLS equation

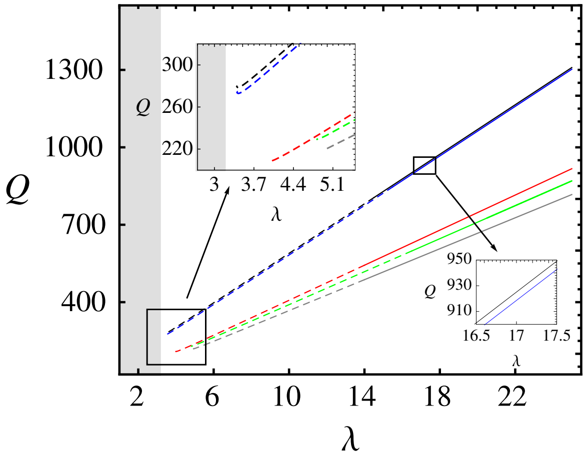

FIGURE 4.26: Q versus λ diagram displaying the families corresponding with some of dissipative solutions reported previously, but for the conservative cubic case.

$$-\lambda\psi_{m,n} + \hat{C}\psi_{m,n} + |\psi_{m,n}|^2\psi_{m,n} = 0. \tag{4.6}$$

Taking as an *ansatz* for the decoupled limit for some of the solutions previously described, we have obtained the same kind of structures for the discrete NLS equation. We have constructed the corresponding families and also computed their corresponding stability region. We note that all these solutions exist in the Schrödinger limit, but are stable only for high values of their optical power content.

In Fig. 4.26 we show five families of stationary solutions of the discrete NLS equation that correspond with some of the solutions reported in the previous sections. Namely, the blue line is the family corresponding with the solution displayed in Fig. 4.18(a) and (b), the black line with the Fig. 4.22(e) and (f), and the red, green and gray line with Fig. 4.24(a) and (b), Fig. 4.24(c) and (d) and Fig. 4.24(e) and (f) respectively. The stable (unstable) solutions are represented by continuous (dashed) lines. The inset located in the upper left corner at Fig. 4.26 shows a magnified view of the region close to the linear band (gray zone). As usual in discrete systems, each one of these families tends to increase its power steeply after passing through the point of minimum optical power closer to the linear band. The other inset at the lower right corner shows a zoom of the black and blue curves, which are almost indistinguishable because they have very similar spatial profiles. This last case concludes our presentation of the discrete dissipative vortex solitons and their properties.

4.8 Summary

We have analyzed the existence and stability of discrete vortex solitons in 2D dissipative optical lattices. We have identified families of discrete vortex-type structures, symmetric and asymmetric, with $S = 1, 2$ and 3, topological charges. Besides, we identify a subspace in the parameter space where coexist several families, which exhibits two topological charges, simultaneously. In particular, we have focused in the *swirl*-vortex soliton, showing how it can be conceived dynamically, starting from a simple initial configuration.

Also, we have studied the influence on the stability of the solutions when dissipation in the system is varied. We observe that the size of the stability region in parameter space increases as the dissipation is increased. A comparison with the conservative cubic case is done, showing that dissipation serves to provide stability to otherwise unstable conservative solutions.

Additionally, we have reported several new families of composite discrete vortex solitons, characterized for having two topological charges simultaneously, and coexisting for the same set of parameters. By superposing two or more of these vortices, we have been able to produce new, dynamically stable composite vortex solitons that are also endowed with multiple vorticity charges. Additionally, we have shown that these composite structures persist in the conservative limit where they are stable for high values of their power content.

5

Conclusion

Dissipative systems are most common in nature. In fact any physical model is only an idealization. Optical Solitons in dissipative media presents a rich variety of forms and behaviors. From scalar to vectorial ones, temporal to spatial and spatio-temporal, all of them can be observed in passively mode locked lasers and in optical cavities of wide aperture lasers. The main objective in this dissertation has been to analyze the existence and stability of two-dimensional soliton solutions in dissipative systems, as well as, the identification of regions where these structures exhibit novel transversal dynamics and exotic properties.

We found several types of self-localized light beams in both, continuous and discrete media. Along this work we have predicted exotic pulsating beams as well as rotating ones in continuous media. Additionally, we found stable vortex solutions with two topological charges, simultaneously, in discrete media. Besides, the relationship between the stability of discrete solutions and strength of the dissipation was analyzed.

We studied a variety of two-dimensional beams and their evolution in dissipative continuous media; in particular we focused on subspaces beyond the two main regions of existence of stable stationary beams with radial symmetry (regions of ground state solitons). We have found a multiplicity of transverse shapes of solitons and a myriad of bifurcations between them. We have also found that the beam shapes and their evolution depend strongly on which of the two regions in the parameter space we are close to.

Near the region of stable stationary continuously self-focusing solitons (region I of ground state solitons) we have found several types of bifurcations. (1) Bifurcation into a stable stationary beam of elliptic shape. (2) Bifurcation into pulsating beams with harmonic pulsations or more complicated pulsations with highly involved shape evolution. Beams can be pulsating and rotating simultaneously. Some of the evolution scenarios are caused by the attempts of soliton of splitting into two separate beams. Generally speaking, any bifurcation around this region destroys the radial symmetry of the solution. Near to the region of stable stationary continuously self-defocusing beams (region II of ground state solitons), the soliton keeps its radial symmetry after the bifurcation. Beams in this case are pulsating but stay radially symmetric. Pulsating beams can further be transformed into exploding ones, that loose the radial symmetry at the moment of the explosion but recover the original profile between the explosions.

Additionally, we studied (2+1)-D ring vortex structures in dissipative continuous media also governed by the complex cubic-quintic Ginzburg-Landau equation. We have found regions of stability for ring solitons with vorticity S ranging from 1 to 5 and additionally for $S = 9$. The existence of vortex ring solitons with S from 1 to 5 and the fact that their region of existence does not shrink when increasing S to 9 shows clearly that such structures can exist for any higher value of S. The unique property of dissipative ring structures is their bifurcation patterns. Radially symmetric ring structures can be transformed into ring structures which are modulated or bent along the ring. They can also pulsate periodically or chaotically. Despite all these transformations, they remain stable as a single ring with given S. These properties make them distinctively different from any known vortex solitons in conservative media.

On the other hand, for the first time, we have addressed the existence and stability of discrete vortex solitons in dissipative two-dimensional optical lattices. We have found symmetric and asymmetric soliton solutions with higher order of its topological charge, all them coexisting for the same set of values in the parameters space. Besides, we have found several new families of discrete vortex solitons, characterized for having two topological charges simultaneously, and also, coexisting for the same set of parameters. In particular, we have shown in detail the *so-called* swirl vortex solution. We have analyzed the stability of this kind of solution when dissipation in the system is varied. We observe that the size of the stability region in parameter spaces increases as the dissipation is increased. A comparison with the conservative cubic case is done, showing that dissipation serves to provide stability to otherwise unstable conservative solutions. We were able to dynamically excite it by using a simple initial configuration and therefore, believe in the feasibility of experimental observation of this novel type of dissipative structures.

Finally, in order to complete the description for discrete dissipative systems, we addressed the interaction between vortex solitons with two topological charges, simultaneously. By superposing two or more of these vortices, we have been able to produce new, dynamically stable composite vortex solitons that are also endowed with multiple topological charges. Additionally, we have shown that these composite structures persist in the conservative limit where they are stable for high values of their power content.

There are different directions which the research may take. In particular, the next three topic seems interesting to continue our investigation field:

Complexity - Optical modes in the presence of ‘imperfect’ (correlated) disorder. Anderson’s localization is rigorously true only for perfect disorder (uncorrelated). We will examine how the presence of spatial correlations affects the pulse mobility.

Pulse management - Competition between spatial frequency chirping and disorder in photonic crystal fibers. Disorder tends to localize excitations while a chirp in the index of refraction acts like an external field which tends to accelerate the excitation.

$\mathcal{PT}$ symmetric systems - Self trapped beams in nonlinear pseudo-Hamiltonian systems, which feature a balance between optical losses and gain. This is a hot, recent development, that is gaining applications in many fields where losses and gain are present. They are characterized by a non- Hermitian Hamiltonian which however, possesses real eigenvalues.

A

Beam Propagation Method

There are no known analytic solutions of the two dimensional complex CQGL equation (3.1). It is possible consider the simplest case of stationary 2D solitons with plain “bell-shaped” profiles. This class of solutions can be well approximated with reasonably simple trial functions, and this allows predict the existence of semi analytical solutions using, e.g. the method of moments or Lagrangian formalism. On the other hand, numerical simulations are not restricted to cylindrically symmetric beams. They allow us to find more complicated beam shapes, as well as their dynamics.

Since the work of Fleck et al. (1976), the beam propagation method (BPM) is by far the most widely used, and it is adopted in the present work. A different approach is to use a finite difference method, e.g. the Crank-Nicolson method, but these are typically more computationally intensive and will not be covered here.

A.1 Operator Splitting

The complex CQGL equation (3.1) can be written in the form

$$\frac{\partial \psi}{\partial z} = \hat{\mathbb{P}}\psi. \tag{A.1}$$

Equation (A.1) can be integrated in quadratures by separating the variables as

$$\frac{\partial \psi}{\psi} = \hat{\mathbb{P}}\partial z \rightarrow \ln \psi = \hat{\mathbb{P}}z \rightarrow \psi = \exp\left(\hat{\mathbb{P}}z\right) \tag{A.2}$$

$\hat{\mathbb{P}}$ is the propagation operator, which can be split as sum of $\hat{\mathbb{D}}$, the diffraction operator, and $\hat{\mathbb{N}}$, the nonlinear operator. The first one can be written as

$$\hat{\mathbb{D}} = \left(\frac{i\mathcal{D}}{2} + \beta\right)\nabla_\perp, \tag{A.3}$$

where $\nabla_\perp$ is the transversal Laplace operator. The first term in (A.3) accounts for diffraction upon propagation in free space, the last one stands for spatial filtering in the cavity.

The second contribution in $\hat{\mathbb{P}}$ can be written as

$$\hat{\mathbb{N}} = \delta\psi + (\varepsilon + i)|\psi|^2\psi + (\mu + i\nu)|\psi|^4\psi, \tag{A.4}$$

which contains Kerr focusing terms, linear losses and nonlinear amplification.

Formally, solutions of Eq. (A.1) can be written as $\psi = \exp[(\hat{\mathbb{D}} + \hat{\mathbb{N}})z]$. $\hat{\mathbb{D}}$ is differential operator and $\hat{\mathbb{N}}$ is a multiplication operator, which do not commute and the rule $\exp(\hat{A} + \hat{B}) = \exp(\hat{A})\exp(\hat{B})$ is not applicable. However,

$$e^{ih_z(\hat{\mathbb{D}}+\hat{\mathbb{N}})} \approx e^{ih_z\hat{\mathbb{D}}/2}e^{ih_z\hat{\mathbb{N}}}e^{ih_z\hat{\mathbb{D}}/2}, \tag{A.5}$$

is an approximation, which have an error proportional to h_z^3.

The principle of the BPM consists of solving Eq. (A.1) for steps h_z small enough, so that the dispersive (linear) step and the nonlinear step can be taken separately. Then, the beam is repeatedly propagated in small steps until it reaches the end of the media (Agrawal, 2006). The implementation of the BPM is relatively straightforward if we think the system as a bulk media divided, along its longitudinal axis, into a large number of transversal segments.

The exponential operator $\exp(h_z\hat{\mathbb{D}})$ can be evaluated in the Fourier domain as follows:
First we take the Fourier transform over the field,

$$\tilde{\psi}(k_x, k_y) = \int \psi(x, y)e^{i(xk_x+yk_y)}\,\mathrm{d}\,x\,\mathrm{d}\,y. \tag{A.6}$$

Then, propagating h_z is the Fourier space

$$\tilde{\psi}(k_x, k_y, h_z) = e^{-i(k_x^2+k_y^2)h_z}\tilde{\psi}(k_x, k_y). \tag{A.7}$$

Finally, Fourier back transformation yields

$$\psi(x, y) = \int e^{-i(xk_x+yk_y)}\tilde{\psi}(k_x, k_y, h_z)\frac{\mathrm{d}\,k_x}{2\pi}\frac{\mathrm{d}\,k_y}{2\pi}. \tag{A.8}$$

On the other hand, the nonlinear step represented by $\exp(h_z\hat{\mathbb{N}})$, must in general be solved by numerical integration

$$\psi(x, y, h_z) = \int_0^{h_z} \hat{\mathbb{N}}\psi(x, y)\,\mathrm{d}\,x\,\mathrm{d}\,y, \tag{A.9}$$

using, e.g. a Runge-Kutta algorithm.

B

Newton Rapshon Method

As was explained in the Appendix (C), the two dimensional discrete complex CQGL equation can be mapped into a one dimensional equation. It can be written as

$$i\dot{\psi}_k + C(\psi_{k+1} + \psi_{k-1} + \psi_{k+K} + \psi_{k-K}) + |\psi_k|^2\psi_k + \\ \nu|\psi_k|^4\psi_k = i\delta\psi_k + i\varepsilon|\psi_k|^2\psi_k + i\mu|\psi_k|^4\psi_k, \tag{B.1}$$

which have stationary solutions that, usually, can be presented as

$$\psi_k(z) = \phi_k \exp(i\lambda z), \quad \text{where } \lambda \in \mathbb{R} \text{ and } \phi_k \in \mathbb{C}. \tag{B.2}$$

By inserting the previous *ansatz* into Eq. (B.1) we obtain the following set of algebraic coupled complex equations:

$$-\lambda\phi_k + \hat{C}\phi_k + |\phi_k|^2\phi_k + \nu|\phi_k|^4\phi_k - i\delta\phi_k - i\varepsilon|\phi_k|^2\phi_k - i\mu|\phi_k|^4\phi_k = 0. \tag{B.3}$$

Usually, solutions of Eq. (B.3) are found by means of a root-finding algorithm. In a waveguide array the number of equation is larger, hence, a numerical implementation of these algorithms becomes imperative to find a solution of the system.

Let us define $\vec{\Phi} = \{\phi_1, \phi_2, ..., \phi_N\}$ as a solution of Eq. (B.3), such that

$$\mathbf{F}(\vec{\Phi}) = \mathbf{0}, \tag{B.4}$$

where $\mathbf{F}$ denotes the entire vector of functions F_i. In the neighborhood of $\vec{\Phi}$, each one of the functions F_i can be expanded in Taylor series

$$F_i(\vec{\Phi} + \delta\vec{\Phi}) = F_i(\vec{\Phi}) + \sum_{j=1}^{N} \frac{\partial F_i}{\partial \phi_j} \delta\phi_j + \mathcal{O}(\delta\vec{\Phi}^2), \tag{B.5}$$

The matrix of partial derivatives appearing in equation Eq. (B.5) is the Jacobian matrix $\hat{\mathbf{J}}$:

$$J_{ij} \equiv \frac{\partial F_i}{\partial \phi_j}. \tag{B.6}$$

Hence, we use the matrix notation to write Eq. (B.5) can be written as

$$\mathbf{F}(\vec{\Phi} + \delta\vec{\Phi}) = \mathbf{F}(\vec{\Phi}) + \hat{\mathbf{J}} \cdot \delta\vec{\Phi} + \mathcal{O}(\delta\vec{\Phi}^2), \tag{B.7}$$

By neglecting terms of order $\delta\vec{\Phi}^2$ and higher and by setting $\mathbf{F}(\vec{\Phi} + \delta\vec{\Phi}) = \mathbf{0}$, we obtain a set of linear equations for the corrections $\delta\vec{\Phi}$ that move each function closer to zero simultaneously, namely

$$\hat{\mathbf{J}} \cdot \delta\vec{\Phi} = -\mathbf{F}, \tag{B.8}$$

and from here we obtain the correction

$$\delta\vec{\Phi} = -\hat{\mathbf{J}}^{-1} \cdot \mathbf{F}. \tag{B.9}$$

Matrix equation (B.9) can be solved by LU factorization. Thus, the corrections are then added to the solution vector,

$$\vec{\Phi}_{k+1} = \vec{\Phi}_k + \delta\vec{\Phi}. \tag{B.10}$$

Equation (B.10) can be used iteratively from some initial guess to yield a better and better approximation of $\vec{\Phi}$. The algorithm terminates once a value of $\vec{\Phi}$ is reached such that $\mathbf{F}(\vec{\Phi})$ is sufficiently close to zero.

C

Stability of Discrete Solutions

We now focus on the analysis of the two-dimensional discrete complex CQGL equation of the form

$$\begin{aligned} i\dot{\psi}_{m,n} + C(\psi_{m+1,n} + \psi_{m-1,n} + \psi_{m,n+1} + \psi_{m,n-1}) + |\psi_{m,n}|^2\psi_{m,n} + \\ \nu|\psi_{m,n}|^4\psi_{m,n} = i\delta\psi_{m,n} + i\varepsilon|\psi_{m,n}|^2\psi_{m,n} + i\mu|\psi_{m,n}|^4\psi_{m,n} \ . \end{aligned} \tag{C.1}$$

As we can see, this set of equations relates the wave function $\psi_{m,n}$, for the optical field propagating along the waveguide located at (m, n) site, with its first neighbors, i.e., $\psi_{m+1,n}$, $\psi_{m-1,n}$, $\psi_{m,n+1}$ and $\psi_{m,n-1}$. Although this set of ordinary differential equations describes a system with a bi-dimensional geometry, it can be possible re-write the set in such way that only we need use one index to cover each one of the sites in the optical array.

C.1 Euclidean Dimensionality Reduction

Without loss of generality, we can consider that our optical array have square symmetry, i.e., the index n and m has the same domain

$$\{(n, m)| \ n \text{ and } m \in (1, 2, ..., K)\}$$

where K is the size of the edge in the square lattice. With the previous assumption and keeping in mind the coupled-mode approximation, we can reorganize the two dimensional optical array as only one linear chain, preserving their original couplings. Indeed, the whole array can be thought as the *add* of each one

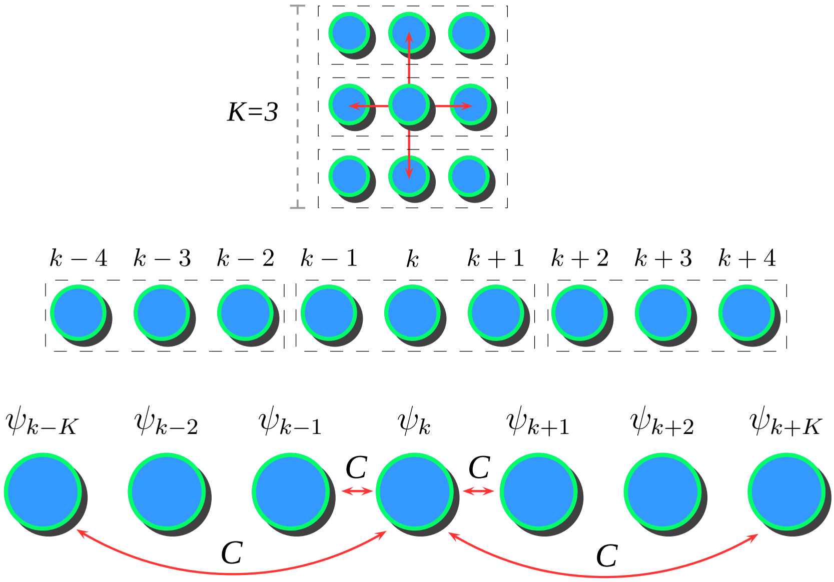

FIGURE C.1: Transformation of two-dimensional lattice in a linear chain. All the original couplings has been preserved by complying with the coupled-mode approach.

of the rows (or columns) to set up it as one dimensional array. This is illustrated on the diagram depicted in Fig. C.1.

From this reorganization is natural to think that the physical description of the original problem must be reformulated. In fact, all the couplings has been redistributed along the same dimension such that the ψ_k field is coupled two times to the left and two more to the right. Two of them comes from the original left and right neighbor fields, the other two coupling correspond to the upper a lower neighbors, which has been relocated at K sites to the left and right from kth field. Taking into account the previous description, Eq. (C.2) can be presented as

$$\begin{aligned} i\dot{\psi}_k + C(\psi_{k+1} + \psi_{k-1} + \psi_{k+K} + \psi_{k-K}) + |\psi_k|^2\psi_k + \\ \nu|\psi_k|^4\psi_k = i\delta\psi_k + i\varepsilon|\psi_k|^2\psi_k + i\mu|\psi_k|^4\psi_k, \end{aligned} \tag{C.2}$$

where $k \in (1, 2, ..., K^2)$.

C.2 Linear Stability Analysis

As was mentioned in the section 4.2, there exist stationary solutions for the discrete complex CQGL equation. Usually they can be written as

$$\psi_k(z) = \phi_k \exp(i\lambda z), \quad \text{where } \lambda \in \mathbb{R} \text{ and } \phi_k \in \mathbb{C}. \tag{C.3}$$

On propagation, small perturbations around the stationary solution can grow exponentially, leading to the destruction of the vortex soliton. A stability analysis provides us with the means for establishing which solutions are linearly stable. Let us introduce a small perturbation $\tilde{\phi}$, to the localized stationary solution (C.3)

$$\tilde{\psi}_k = [\phi_k + \tilde{\phi}_k(z)]e^{i\lambda z}, \qquad \tilde{\phi}_k \in \mathbb{C}. \tag{C.4}$$

Taking into account that $\tilde{\phi}_k^p \to 0$ for $p \geq 2$, the nonlinear terms are:

$$\begin{aligned} |\tilde{\psi}_k|^2\tilde{\psi}_k &= [\phi_k + \tilde{\phi}_k(z)][\phi_k^* + \tilde{\phi}_k^*(z)]^2 e^{i\lambda z} \\ &\approx (\phi_k^2\tilde{\phi}_k{}^* + 2|\phi_k|^2\tilde{\phi}_k + |\phi_k|^2\phi_k)e^{i\lambda z} \end{aligned} \tag{C.5}$$

and

$$\begin{aligned} |\tilde{\psi}_k|^4\tilde{\psi}_k &= [\phi_k + \tilde{\phi}_k(z)]^2[\phi_k^* + \tilde{\phi}_k^*(z)]^3 e^{i\lambda z} \\ &\approx (2|\phi_k|^2\phi_k^2\tilde{\phi}_k{}^* + 3|\phi_k|^4\tilde{\phi}_k + |\phi_k|^4\phi_k)e^{i\lambda z} \end{aligned} \tag{C.6}$$

then, after replacing (C.4), (C.5) and (C.6) into Eq. (C.2) and then linearizing with respect to $\tilde{\phi}$, we obtain:

$$\begin{gathered} i\dot{\tilde{\phi}}_k - i\delta\tilde{\phi}_k + C(\tilde{\phi}_{k+1} + \tilde{\phi}_{k-1} + \tilde{\phi}_{k+K} + \tilde{\phi}_{k-K}) - \lambda\tilde{\phi}_k \\ -2i\varepsilon\,|\phi_k|^2\tilde{\phi}_k - 3i\mu\,|\phi_k|^4\tilde{\phi}_k + 3\nu\,|\phi_k|^4\tilde{\phi}_k + 2\,|\phi_k|^2\tilde{\phi}_k \\ -2i\mu\phi_k^2\,|\phi_k|^2\tilde{\phi}_k{}^* + 2\nu\phi_k^2\,|\phi_k|^2\tilde{\phi}_k{}^* - i\varepsilon\phi_k^2\tilde{\phi}_k{}^* + \phi_k^2\tilde{\phi}_k{}^* = 0, \end{gathered} \tag{C.7}$$

and factorizing the perturbation function in (C.7), we have

$$\begin{gathered} i\dot{\tilde{\phi}}_k + \hat{C}\tilde{\phi}_k - i\delta\tilde{\phi}_k + [2(1-i\varepsilon)|\phi_k|^2 + 3(\nu - i\mu)|\phi_k|^4 - \lambda]\tilde{\phi}_k + \\ [(1-i\varepsilon)\phi_k^2 + 2(\nu - i\mu)|\phi_k|^2\phi_k^2]\tilde{\phi}_k^* = 0. \end{gathered} \tag{C.8}$$

The previous equation describes how the perturbation evolves. In general terms, this kind of differential equation have solutions that can be written as linear combination of exponential functions, where their arguments determine when the perturbation grows or it remains constant during the evolution. To solve equations (C.8) we first separate the real and imaginary part of the solution and its perturbation,

$$\phi_k = u_k + iv_k, \quad \tilde{\phi}_k(z) = x_k(z) + iy_k(z), \quad \text{where } u,\ v,\ x, \text{ and } y \in \mathbb{R}. \tag{C.9}$$

Replacing (C.9) in (C.8) and separating real and imaginary parts we obtain two ordinary differential equations, namely

$$\begin{aligned} \dot{x}_k + \hat{C}y_k + h_1 y_k + h_2 x_k &= 0, \\ \dot{y}_k - \hat{C}x_k + h_3 x_k + h_4 y_k &= 0, \end{aligned} \tag{C.10}$$

where, the h factors are given by:

$$\begin{aligned} h_1 &= -2uv - \delta - u^2\varepsilon - 3v^2\varepsilon - u^4\mu - 6u^2v^2\mu - 5v^4\mu - 4u^3v\nu - 4uv^3\nu, \\ h_2 &= -3u^2 - v^2 - 2uv\varepsilon + \lambda - 4u^3v\mu - 4uv^3\mu - 5u^4\nu - 6u^2v^2\nu - v^4\nu, \\ h_3 &= 2uv - \delta - 3u^2\varepsilon - v^2\varepsilon - 5u^4\mu - 6u^2v^2\mu - v^4\mu + 4u^3v\nu + 4uv^3\nu, \\ h_4 &= u^2 + 3v^2 - 2uv\varepsilon - \lambda - 4u^3v\mu - 4uv^3\mu + u^4\nu + 6u^2v^2\nu + 5v^4\nu. \end{aligned} \tag{C.11}$$

We define four matrices as follows:

$$\begin{aligned} \mathbf{A} &= C(\delta_{k+1,l} + \delta_{k-1,l}) + h_1\delta_{k,l}, & \mathbf{B} &= h_2\delta_{k,l}, \\ \mathbf{C} &= -C(\delta_{k+1,l} + \delta_{k-1,l}) + h_3\delta_{k,l}, & \mathbf{D} &= h_4\delta_{k,l}, \end{aligned}$$

where $\delta_{k,l}$ is the Krocnecker symbol. The system (C.10) can be expressed by means of these matrices; then now it looks like,

$$\dot{\vec{x}} + \mathbf{A}\vec{y} + \mathbf{B}\vec{x} = 0, \qquad \dot{\vec{y}} + \mathbf{C}\vec{x} + \mathbf{D}\vec{y} = 0,$$

or in matricial form,

$$\dot{\mathbf{R}} = -\begin{pmatrix} \mathbf{B} & \mathbf{A} \\ \mathbf{D} & \mathbf{C} \end{pmatrix}\mathbf{R}, \quad \text{where} \quad \mathbf{R} = \begin{pmatrix} \vec{x} \\ \vec{y} \end{pmatrix}. \tag{C.12}$$

The matrix equation (C.12) is a linear and homogeneus system of ordinary differential equations, for which its solution can be written as

$$\mathbf{R} = \begin{pmatrix} l_1 \\ l_2 \\ \vdots \\ l_N \end{pmatrix} e^{\gamma z} = \mathbf{L}e^{\gamma z}, \tag{C.13}$$

being $N = 2K^2$. If we replace the *ansatz* (C.13) in (C.12) the system becomes:

$$\mathbf{L}\gamma e^{\gamma z} = \mathbf{H}\mathbf{L}e^{\gamma z}, \quad \text{where} \quad \mathbf{H} = -\begin{pmatrix} \mathbf{B} & \mathbf{A} \\ \mathbf{D} & \mathbf{C} \end{pmatrix}. \tag{C.14}$$

Now, if we divide (C.14) by $e^{\gamma z}$, and rearranging we have

$$(\mathbf{H} - \gamma\mathbf{I})\mathbf{L} = \mathbf{0}. \tag{C.15}$$

The equation (C.15) is equivalent to the algebraic system

$$\begin{array}{rrr} (h_{11}-\gamma)l_1+ & h_{12}l_2+\ldots+ & h_{1N}l_N=0 \\ h_{21}l_1+ & (h_{22}-\gamma)l_2+\ldots+ & h_{1N}l_N=0 \\ & & \\ h_{N1}l_1+ & h_{N2}l_2+\ldots+ & (h_{NN}-\gamma)h_{NN}l_N=0. \end{array} \tag{C.16}$$

Thus, to determine a non trivial solution $\mathbf{L}$ of the system (C.12) is necessary that

$$\det\left(\mathbf{H}-\gamma\mathbf{I}\right)=0. \tag{C.17}$$

This is the characteristic equation of the $\mathbf{H}$ matrix; in other words, $\mathbf{R}=\mathbf{L}e^{\gamma z}$ will be a solution of the system (C.12) if and only if γ is a eigenvalue of $\mathbf{H}$, and $\mathbf{L}$ is an eigenvector corresponding to γ. The general solution of this system is

$$\mathbf{R}=c_1\mathbf{L}_1e^{\gamma_1 z}+c_2\mathbf{L}_2e^{\gamma_2 z}\cdots+c_N\mathbf{L}_Ne^{\gamma_N z}, \tag{C.18}$$

being $c_1, c_2, \cdots$ integration constants. The set $\{\gamma_1, \gamma_2, \cdots, \gamma_N\}$ is the spectrum of the *eigensystem* associated with (C.12). If at least one of the eigenvalues is a complex number then $\mathbf{R}^*$, the conjugate complex, also is a solution to the system (C.12).

Here, we have to remind that the vector $\mathbf{R}$ contains all the components of the perturbation function $\tilde{\phi}_k$. The stability of localized structure ϕ_k is determined by the discrete spectrum of the eigenvalues of (C.17) with a nonzero real part. More precisely, a localized structure is unstable if $\mathbb{R}(\gamma)>0$, where the maximum is chosen among all the roots of (C.17). If at least one of the eigenvalues has real part greater than zero the perturbation $\tilde{\phi}_k$ grows exponentially, what leads to an uncontrolled evolution of the stationary solution profile.

List of Figures

Bibliography

Abdullaev, F. K., Baizakov, B. B., Darmanyan, S. A., Konotop, V. V., & Salerno, M. (2001). Nonlinear excitations in arrays of bose-einstein condensates. *Phys. Rev. A*, *64*, 043606. 9

Agrawal, G. (2006). *Nonlinear Fiber Optics*. Optics and Photonics. Academic Press. 100

Akhmediev, N., & Ankiewicz, A. (1997). *Solitons: Nonlinear Pulses and Beams*. Optical and quantum electronics series. Chapman & Hall. 17

Akhmediev, N., & Ankiewicz, A. (2008). *Dissipative solitons: from optics to biology and medicine*. Lecture notes in physics. Springer. 15

Akhmediev, N., Soto-Crespo, J. M., & Town, G. (2001). Pulsating solitons, chaotic solitons, period doubling, and pulse coexistence in mode-locked lasers: Complex ginzburg-landau equation approach. *Phys. Rev. E*, *63*, 056602. 42, 46, 53, 64

Akhmediev, N. N., & Ankiewicz, A. (2005). *Dissipative solitons*. Lecture notes in physics. Springer. 15

Akhmediev, N. N., Ankiewicz, A., & Soto-Crespo, J. M. (1997). Multisoliton solutions of the complex ginzburg-landau equation. *Phys. Rev. Lett.*, *79*(21), 4047–4051. 86

Alexander, T. J., Sukhorukov, A. A., & Kivshar, Y. S. (2004). Asymmetric vortex solitons in nonlinear periodic lattices. *Phys. Rev. Lett.*, *93*(6), 063901. 54, 72, 80

Alfimov, G. L., Kevrekidis, P. G., Konotop, V. V., & Salerno, M. (2002). Wannier functions analysis of the nonlinear schrödinger equation with a periodic potential. *Phys. Rev. E*, *66*, 046608. 9

Altug, H., Englund, D., & Vuckovic, J. (2006). Ultrafast photonic crystal nanocavity laser. *Nature*, *2*(330), 484–488. 70

Ankiewicz, A., Devine, N., Akhmediev, N., & Soto-Crespo, J. M. (2008). Continuously self-focusing and continuously self-defocusing two-dimensional beams in dissipative media. *Phys. Rev. A*, *77*, 033840. 39, 40, 41, 42

Aranson, I. S., & Kramer, L. (2002). The world of the complex ginzburg-landau equation. *Rev. Mod. Phys.*, *74*(1), 99. 37

Arecchi, F. T., Giacomelli, G., Ramazza, P. L., & Residori, S. (1991). Vortices and defect statistics in two-dimensional optical chaos. *Phys. Rev. Lett.*, *67*, 3749–3752. 8

Arévalo, E. (2009). Soliton theory of two-dimensional lattices: The discrete nonlinear schrödinger equation. *Phys. Rev. Lett.*, *102*(22), 224102. 70

Artigas, D., Torner, L., Torres, J. P., & Akhmediev, N. N. (1997). Asymmetrical splitting of higher-order optical solitons induced by quintic nonlinearity. *Optics Communications*, *143*(4-6), 322 – 328. 19

Ashkin, A., Dziedzic, J. M., & Yamane, T. (1987). Optical trapping and manipulation of single cells using infrared laser beams. *Nature*, *330*(330), 769–771. 8

Askaryan, G. A. (1962). Effects of the gradient of strong electromagnetic beam on electrons and atoms. *SOVIET PHYSICS JETP*, *15*(6), 1088–1090. 6

Baker, H. F. (1897). *Abelian functions: Abel's theorem and the allied theory of theta functions*. Cambridge mathematical library. Cambridge University Press. 3

Baranova, N. B., Mamaev, A. V., Pilipetsky, N. F., Shkunov, V. V., & Zel'dovich, B. Y. (1983). Wave-front dislocations: topological limitations for adaptive systems with phase conjugation. *J. Opt. Soc. Am.*, *73*(5), 525–528. 8

Basistiy, I., Soskin, M., & Vasnetsov, M. (1995). Optical wavefront dislocations and their properties. *Optics Communications*, *119*(5-6), 604 – 612. 8

Batchelor, G. (2000). *An introduction to fluid dynamics*. Cambridge mathematical library. Cambridge University Press. 38

Bazhenov, V., Soskin, M., & Vasnetsov, M. (1992). Screw dislocations in light wavefronts. *Journal of Modern Optics*, *39*(5), 985–990. 38

Bergé, L. (1998). Wave collapse in physics: principles and applications to light and plasma waves. *Physics Reports*, *303*(5-6), 259 – 370. 9

Bishop, A. R. (Ed.) (1981). *Solitons and Condensed Matter Physics*, Springer Series in Solid-State Science. Berlin, Germany: Springer-Verlag. 3

Boyd, R. W. (2008). *Nonlinear optics*. Academic Press. 4

Brambilla, M., Battipede, F., Lugiato, L. A., Penna, V., Prati, F., Tamm, C., & Weiss, C. O. (1991). Transverse laser patterns. i. phase singularity crystals. *Phys. Rev. A*, *43*, 5090–5113. 8

Campbell, D. K., Flach, S., & Kivshar, Y. S. (2004). Localizing energy through nonlinearity and discreteness. *Physics Today*, *57*(1), 43–49. 10, 70

Cataliotti, F. S., Burger, S., Fort, C., Maddaloni, P., Minardi, F., Trombettoni, A., Smerzi, A., & Inguscio, M. (2001). Josephson junction arrays with bose-einstein condensates. *Science*, *293*(5531), 843–846. 9, 69

Cataliotti, F. S., Fallani, L., Ferlaino, F., Fort, C., Maddaloni, P., & Inguscio, M. (2003). Superfluid current disruption in a chain of weakly coupled bose‚Äìeinstein condensates. *New Journal of Physics*, *5*(1), 71. 9, 69

Chiao, R. Y., Garmire, E., & Townes, C. H. (1964). Self-trapping of optical beams. *Phys. Rev. Lett.*, *13*, 479–482. 6

Chong, C., Carretero-González, R., Malomed, B., & Kevrekidis, P. (2009). Multistable solitons in higher-dimensional cubic-quintic nonlinear schrödinger lattices. *Physica D: Nonlinear Phenomena*, *238*(2), 126 – 136. 75

Christodoulides, D. N., & Eugenieva, E. D. (2001). Blocking and routing discrete solitons in two-dimensional networks of nonlinear waveguide arrays. *Phys. Rev. Lett.*, *87*, 233901. 13

Christodoulides, D. N., & Joseph, R. I. (1988). Discrete self-focusing in nonlinear arrays of coupled waveguides. *Opt. Lett.*, *13*(9), 794–796. 10

Cramer, J. G., Forward, R. L., Morris, M. S., Visser, M., Benford, G., & Landis, G. A. (1995). Natural wormholes as gravitational lenses. *Phys. Rev. D*, *51*, 3117–3120. 38

Crasovan, L.-C., Malomed, B. A., & Mihalache, D. (2000). Stable vortex solitons in the two-dimensional ginzburg-landau equation. *Phys. Rev. E*, *63*, 016605. 39

Crasovan, L.-C., Malomed, B. A., & Mihalache, D. (2001). Stable vortex solitons in the two-dimensional ginzburg-landau equation. *Phys. Rev. E*, *63*, 016605. 54

Dauxois, T., Peyrard, M., & Bishop, A. R. (1993). Entropy-driven dna denaturation. *Phys. Rev. E*, *47*, R44–R47. 9

Davydov, A. (1991). *Solitons in molecular systems*. Mathematics and its applications (Kluwer Academic Publishers).: Soviet series. Kluwer Academic Publishers. 3

Deissler, R. J., & Brand, H. R. (1994). Periodic, quasiperiodic, and chaotic localized solutions of the quintic complex ginzburg-landau equation. *Phys. Rev. Lett.*, *72*, 478–481. 38

Denschlag, J., Simsarian, J. E., Feder, D. L., Clark, C. W., Collins, L. A., Cubizolles, J., Deng, L., Hagley, E. W., Helmerson, K., Reinhardt, W. P., Rolston, S. L., Schneider, B. I., & Phillips, W. D. (2000). Generating solitons by phase engineering of a bose-einstein condensate. *Science*, *287*(5450), 97–101. 3

Desyatnikov, A. S., Dennis, M. R., & Ferrando, A. (2011). All-optical discrete vortex switch. *Phys. Rev. A*, *83*(6), 063822. 70

Dreischuh, A., Paulus, G. G., Zacher, F., Grasbon, F., & Walther, H. (1999). Generation of multiple-charged optical vortex solitons in a saturable nonlinear medium. *Phys. Rev. E*, *60*, 6111–6117. 38

Efremidis, N. K., Christodoulides, D. N., & Hizanidis, K. (2007a). Two-dimensional discrete ginzburg-landau solitons. *Phys. Rev. A*, *76*(4), 043839. 70, 80

Efremidis, N. K., Hizanidis, K., Malomed, B. A., & Di Trapani, P. (2007b). Three-dimensional vortex solitons in self-defocusing media. *Phys. Rev. Lett.*, *98*, 113901. 38

Efremidis, N. K., Sears, S., Christodoulides, D. N., Fleischer, J. W., & Segev, M. (2002). Discrete solitons in photorefractive optically induced photonic lattices. *Phys. Rev. E*, *66*, 046602. 9, 13, 69, 72

Eisenberg, H. S., Morandotti, R., Silberberg, Y., Arnold, J. M., Pennelli, G., & Aitchison, J. S. (2002). Optical discrete solitons in waveguide arrays. i. soliton formation. *J. Opt. Soc. Am. B*, *19*(12), 2938–2944. 9

Eisenberg, H. S., Silberberg, Y., Morandotti, R., Boyd, A. R., & Aitchison, J. S. (1998). Discrete spatial optical solitons in waveguide arrays. *Phys. Rev. Lett.*, *81*(16), 3383–3386. 11

Fedorov, S. V., Rosanov, N., Shatsev, A. N., Veretenov, N. A., & Vladimirov, A. G. (2003). Topologically multicharged and multihumped rotating solitons in wide-aperture lasers with a saturable absorber. *IEEE J. Quantum Electron.*, *39*, 197. 54

Firth, W. J., & Skryabin, D. V. (1997). Optical solitons carrying orbital angular momentum. *Phys. Rev. Lett.*, *79*, 2450–2453. 9

Fistul, M. V. (2003). Resonant breather states in josephson coupled systems. *Chaos: An Interdisciplinary Journal of Nonlinear Science*, *13*(2), 725–732. 9

Flach, S., & Gorbach, A. V. (2008). Discrete breathers – advances in theory and applications. *Physics Reports*, *467*(1-3), 1 – 116. 10, 70

Flach, S., & Willis, C. (1998). Discrete breathers. *Physics Reports*, *295*(5), 181 – 264.

9

Fleck, J., Morris, J., & Feit, M. (1976). Time-dependent propagation of high energy laser beams through the atmosphere. *Applied Physics A: Materials Science and Processing*, *10*, 129–160. 10.1007/BF00896333. 99

Fleischer, J. W., Bartal, G., Cohen, O., Manela, O., Segev, M., Hudock, J., & Christodoulides, D. N. (2004). Observation of vortex-ring “discrete” solitons in 2d photonic lattices. *Phys. Rev. Lett.*, *92*(12), 123904. 14, 69

Fleischer, J. W., Carmon, T., Segev, M., Efremidis, N. K., & Christodoulides, D. N. (2003a). Observation of discrete solitons in optically induced real time waveguide arrays. *Phys. Rev. Lett.*, *90*, 023902. 13

Fleischer, J. W., Segev, M., Efremidis, N. K., & Christodoulides, D. N. (2003b). Observation of two-dimensional discrete solitons in optically induced nonlinear photonic lattices. *Nature*, *422*(16), 147–150. 13

G. A. Swartzlander, J., & Law, C. T. (1992). Optical vortex solitons observed in kerr nonlinear media. *Phys. Rev. Lett.*, *69*, 2503–2506. 54

Ganichev, S. D., Ivchenko, E. L., Danilov, S. N., Eroms, J., Wegscheider, W., Weiss, D., & Prettl, W. (2001). Conversion of spin into directed electric current in quantum wells. *Phys. Rev. Lett.*, *86*(19), 4358–4361. 8

García-March, M.-A., Ferrando, A., Zacarés, M., Sahu, S., & Ceballos-Herrera, D. E. (2009). Symmetry, winding number, and topological charge of vortex solitons in discrete-symmetry media. *Phys. Rev. A*, *79*(5), 053820. 75

Gardner, C. S., Greene, J. M., Kruskal, M. D., & Miura, R. M. (1967). Method for solving the korteweg-devries equation. *Phys. Rev. Lett.*, *19*, 1095–1097. 3

Govan, D. S., Forysiak, W., & Doran, N. J. (1998). Long-distance 40-gbit/s soliton transmission over standard fiber by use of dispersion management. *Opt. Lett.*, *23*(19), 1523–1525. 5

Hachair, X., Pedaci, F., Caboche, E., Barland, S., Giudici, M., Tredicce, J., Prati, F., Tissoni, G., Kheradmand, R., Lugiato, L., Protsenko, I., & Brambilla, M. (2006). Cavity solitons in a driven vcsel above threshold. *Selected Topics in Quantum Electronics, IEEE Journal of*, *12*(3), 339 – 351. 38

Hasegawa, A. (2002). Optical Solitons in Fibers for Communication Systems. *Optics and Photonics News*, *13*(2), 33. 5

Hasegawa, A., & Tappert, F. (1973). Transmission of stationary nonlinear optical pulses in dispersive dielectric fibers. i. anomalous dispersion. *Applied Physics Letters*, *23*(3), 142 –144. 5

Haus, H. A. (1975). Theory of mode locking with a slow saturable absorber. *IEEE Journ. of Quantum Electron.*, *11*(9), 736. 37

He, Y. J., Malomed, B. A., Mihalache, D., & Wang, H. Z. (2008). Crescent vortex solitons in strongly nonlocal nonlinear media. *Phys. Rev. A*, *78*, 023824. 54

Heckenberg, N. R., McDuff, R., Smith, C. P., Rubinsztein-Dunlop, H., & Wegener, M. J. (1992a). Laser beams with phase singularities. *Optical and Quantum Electronics*, *24*. 8

Heckenberg, N. R., McDuff, R., Smith, C. P., & White, A. G. (1992b). Generation of optical phase singularities by computer-generated holograms. *Opt. Lett.*, *17*(3), 221–223. 8

Infeld, E., & Rowlands, G. (2000). *Nonlinear waves, solitons, and chaos*. World Books Publishing Corporation. 3

Jones, A. L. (1965). Coupling of optical fibers and scattering in fibers. *J. Opt. Soc. Am.*, *55*(3), 261–269. 11

Kartashov, Y. V., Vysloukh, V. A., & Torner, L. (2005). Stable ring-profile vortex solitons in bessel optical lattices. *Phys. Rev. Lett.*, *94*, 043902. 54

Kivshar, Y. S., & Luther-Davies, B. (1998). Dark optical solitons: physics and applications. *Physics Reports*, *298*(2-3), 81 – 197. 54

Kivshar, Y. S., & Pelinovsky, D. E. (2000). Self-focusing and transverse instabilities of solitary waves. *Physics Reports*, *331*(4), 117 – 195. 9

Kleinert, H. (2008). *Multivalued fields in condensed matter, electromagnetism, and gravitation*. World Scientific. 38

Komarov, A., Leblond, H., & Sanchez, F. (2005). Quintic complex ginzburg-landau model for ring fiber lasers. *Phys. Rev. E*, *72*, 025604. 37

Leblond, H., Malomed, B. A., & Mihalache, D. (2009). Stable vortex solitons in the ginzburg-landau model of a two-dimensional lasing medium with a transverse grating. *Phys. Rev. A*, *80*(3), 033835. 74, 77

Lederer, F., Stegeman, G. I., Christodoulides, D. N., Assanto, G., Segev, M., & Silberberg, Y. (2008). Discrete solitons in optics. *Physics Reports*, *463*(1-3), 1 – 126. 10, 70

Longhi, S., Marangoni, M., Lobino, M., Ramponi, R., Laporta, P., Cianci, E., & Foglietti, V. (2006). Observation of dynamic localization in periodically curved waveguide arrays. *Phys. Rev. Lett.*, *96*, 243901. 11

Mair, A., Weihs, G., & Zeilinger, A. (2001). Entanglement of the orbital angular momentum states of photons. *Nature*, *412*(1), 313–316. 8

Malomed, B., Crasovan, L.-C., & Mihalache, D. (2002). Stability of vortex solitons in the cubic-quintic model. *Physica D: Nonlinear Phenomena*, *161*(3-4), 187 – 201. 38

Malomed, B. A., & Kevrekidis, P. G. (2001). Discrete vortex solitons. *Phys. Rev. E*, *64*(2), 026601. 70

Malos, J., Vaupel, M., Staliunas, K., & Weiss, C. O. (1996). Dynamical structures of a photorefractive oscillator. *Phys. Rev. A*, *53*, 3559–3564. 8

Maruno, K., Ankiewicz, A., & Akhmediev, N. (2005). Dissipative solitons of the discrete complex cubic-quintic ginzburg-landau equation. *Physics Letters A*, *347*(4-6), 231 – 240. 70

Mazo, J. J., & Orlando, T. P. (2003). Discrete breathers in josephson arrays. *Chaos: An Interdisciplinary Journal of Nonlinear Science*, *13*(2), 733–743. 9

McDonald, D. A. (1974). *Blood flow in arteries / Donald A. McDonald*. Edward Arnold, London :, 2nd ed. ed. 3

Michinel, H., Campo-Táboas, J., Quiroga-Teixeiro, M. L., Salgueiro, J. R., & García-Fernández, R. (2001). Excitation of stable vortex solitons in nonlinear cubic-quintic materials. *J. Opt. B: Quantum Semiclass. Opt.*, *3*, 317. 9, 54

Michinel, H., Salgueiro, J. R., & Paz-Alonso, M. J. (2004). Square vortex solitons with a large angular momentum. *Phys. Rev. E*, *70*, 066605. 54

Mihalache, D., Mazilu, D., Lederer, F., Leblond, H., & Malomed., B. A. (2008).

Collisions between coaxial vortex solitons in the three-dimensional cubic-quintic complex ginzburg-landau equation. *Phys. Rev. A*, *77*, 033817. 54

Molina-Terriza, G., Torres, J. P., & Torner, L. (2001). Management of the angular momentum of light: Preparation of photons in multidimensional vector states of angular momentum. *Phys. Rev. Lett.*, *88*(1), 013601. 7

Mollenauer, L. F., Stolen, R. H., & Gordon, J. P. (1980). Experimental observation of picosecond pulse narrowing and solitons in optical fibers. *Phys. Rev. Lett.*, *45*, 1095–1098. 5

Montes, C., Mikhailov, A., Picozzi, A., & Ginovart, F. (1997). Dissipative three-wave structures in stimulated backscattering. i. a subluminous solitary attractor. *Phys. Rev. E*, *55*, 1086–1091. 38

Neshev, D. N., Alexander, T. J., Ostrovskaya, E. A., Kivshar, Y. S., Martin, H., Makasyuk, I., & Chen, Z. (2004). Observation of discrete vortex solitons in optically induced photonic lattices. *Phys. Rev. Lett.*, *92*(12), 123903. 14, 69, 70

Neshev, D. N., Dreischuh, A., Shvedov, V., Desyatnikov, A. S., Krolikowski, W., & Kivshar, Y. S. (2008). Observation of polychromatic vortex solitons. *Opt. Lett.*, *33*(16), 1851–1853. 54

O. Descalzi, G. D., & Tirapegui, E. (2005). On the stable hole solutions in the complex ginzburg-landau equation. *Physica A*, *356*(99), 66–71. 37

Ouzounov, D., Hensley, C., Gaeta, A., Venkateraman, N., Gallagher, M., & Koch, K. (2005). Soliton pulse compression in photonic band-gap fibers. *Opt. Express*, *13*(16), 6153–6159. 5

Pelinovsky, D., Kevrekidis, P., & Frantzeskakis, D. (2005). Persistence and stability of discrete vortices in nonlinear schrödinger lattices. *Physica D: Nonlinear Phenomena*, *212*(1-2), 20 – 53. 72, 76, 80

Peschel, U., Egorov, O., & Lederer, F. (2004). Discrete cavity solitons. *Opt. Lett.*, *29*(16), 1909–1911. 20

Peschel, U., Morandotti, R., Arnold, J. M., Aitchison, J. S., Eisenberg, H. S., Silberberg, Y., Pertsch, T., & Lederer, F. (2002). Optical discrete solitons in waveguide arrays. 2. dynamic properties. *J. Opt. Soc. Am. B*, *19*(11), 2637–2644. 9

Petrov, D. V., Torner, L., Martorell, J., Vilaseca, R., Torres, J. P., & Cojocaru, C. (1998). Observation of azimuthal modulational instability and formation of patterns of optical solitons in a quadratic nonlinear crystal. *Opt. Lett.*, *23*(18), 1444–1446. 9

Peyrard, M., Dauxois, T., Hoyet, H., & Willis, C. (1993). Biomolecular dynamics of dna: statistical mechanics and dynamical models. *Physica D: Nonlinear Phenomena*, *68*(1), 104 – 115. 9

Quiroga-Teixeiro, M., & Michinel, H. (1997). Stable azimuthal stationary state in quintic nonlinear optical media. *J. Opt. Soc. Am. B*, *14*(8), 2004–2009. 9

Rosanov, N. N. (2005). Solitons in laser systems with saturable absorption. In N. Akhmediev, & A. Ankiewicz (Eds.) *Dissipative Solitons*, vol. 661 of *Lecture Notes in Physics*, (pp. 9–17). Springer Berlin / Heidelberg. 37, 38, 54

Rubi, J. M. (2004). Book review: Bose,Äìeinstein condensation. lev pitaevskii and sandro stringari, oxford university press, oxford, 2003. *Journal of Statistical Physics*, *115*, 1763–1764. 10.1023/B:JOSS.0000028243.07395.b3. 3

Scheuer, J., & Orenstein, M. (1999). Optical vortices crystals: Spontaneous generation in nonlinear semiconductor microcavities. *Science*, *285*(5425), 230–233. 8

Scott Russell, J. (1844). Report on waves. In *Report on Waves*, (pp. 311–390). 14th Meeting of the British Association for the Advancement of Science, York. 2

Sergeev, A. M., & Petviashvili, V. I. (1984). Spiral solitons in active media with an excitation threshold. *Sov. Phys. Dokl.*, *276*, 1380–1384. 39

Skryabin, D. V., & Firth, W. J. (1998). Dynamics of self-trapped beams with phase dislocation in saturable kerr and quadratic nonlinear media. *Phys. Rev. E*, *58*, 3916–3930. 9

Somekh, S., Garmire, E., Yariv, A., Garvin, H., & Hunsperger, R. (1973). Channel optical waveguide directional couplers. *Applied Physics Letters*, *22*(1), 46–47. 31

Soto-Crespo, J., Akhmediev, N., & Ankiewicz, A. (2003). Motion and stability properties of solitons in discrete dissipative structures. *Physics Letters A*, *314*(1-2), 126 – 130. 70

Soto-Crespo, J. M., Akhmediev, N., & Ankiewicz, A. (2000a). Pulsating, creeping, and erupting solitons in dissipative systems. *Phys. Rev. Lett.*, *85*, 2937–2940. 19, 21, 41, 53

Soto-Crespo, J. M., Akhmediev, N. N., Collings, B. C., Cundiff, S. T., Bergman, K., & Knox, W. H. (2000b). Polarization-locked temporal vector solitons in a fiber laser: theory. *J. Opt. Soc. Am. B*, *17*(3), 366–372. 77, 79

Soto-Crespo, J. M., Heatley, D. R., Wright, E. M., & Akhmediev, N. (1991). Stability of the higher-bound states in a saturable self-focusing medium. *Phys. Rev. A*, *44*, 636–644. 54, 58, 60

Stegeman, G., Christodoulides, D., & Segev, M. (2000). Optical spatial solitons: historical perspectives. *Selected Topics in Quantum Electronics, IEEE Journal of*, *6*(6), 1419 –1427. 6

Sukhorukov, A., Kivshar, Y., Eisenberg, H., & Silberberg, Y. (2003). Spatial optical solitons in waveguide arrays. *Quantum Electronics, IEEE Journal of*, *39*(1), 31 – 50. 9, 69

Taki, M., Ouarzazi, N., Ward, H., & Glorieux, P. (2000). Nonlinear front propagation in optical parametric oscillators. *J. Opt. Soc. Am. B*, *17*(6), 997–1003. 37

Terhalle, B., Richter, T., Law, K. J. H., Göries, D., Rose, P., Alexander, T. J., Kevrekidis, P. G., Desyatnikov, A. S., Krolikowski, W., Kaiser, F., Denz, C., & Kivshar, Y. S. (2009). Observation of double-charge discrete vortex solitons in hexagonal photonic lattices. *Phys. Rev. A*, *79*. 76, 80

Tikhonenko, V., & Akhmediev, N. (1996). Excitation of vortex solitons in a gaussian beam configuration. *Opt. Commun.*, *126*, 108. 54

Tikhonenko, V., Kivshar, Y. S., Steblina, V. V., & Zozulya, A. A. (1998). Vortex solitons in a saturable optical medium. *J. Opt. Soc. Am. B*, *15*(1), 79–86. 54

Torres, J. P., Soto-Crespo, J. M., Torner, L., & Petrov, D. V. (1998). Solitary-wave vortices in quadratic nonlinear media. *J. Opt. Soc. Am. B*, *15*(2), 625–627. 38

Towers, I., Buryak, A. V., Sammut, R. A., Malomed, B. A., Crasovan, L. C., & Mihalache, D. (2001). Stability of spinning ring solitons of the cubic-quintic nonlinear schrödinger equation. *Phys. Lett. A*, *288*, 292. 54

Towers, I., & Malomed, B. A. (2002). Stable (2+1)-dimensional solitons in a layered medium with sign-alternating kerr nonlinearity. *J. Opt. Soc. Am. B*, *19*(3), 537–543.

28

Trombettoni, A., & Smerzi, A. (2001). Discrete solitons and breathers with dilute bose-einstein condensates. *Phys. Rev. Lett.*, *86*, 2353–2356. 70

Trompeter, H., Peschel, U., Pertsch, T., Lederer, F., Streppel, U., Michaelis, D., & Bräuer, A. (2003). Tailoring guided modes in waveguide arrays. *Opt. Express*, *11*(25), 3404–3411. 11

Tsoy, E. N., & Akhmediev, N. (2005). Bifurcations from stationary to pulsating solitons in the cubic-quintic complex ginzburg landau equation. *Physics Letters A*, *343*(6), 417 – 422. 46

Ultanir, E., Stegeman, G., Michaelis, D., Lange, C., & Lederer, F. (2005). Dissipative solitons in semiconductor optical amplifiers. In N. Akhmediev, & A. Ankiewicz (Eds.) *Dissipative Solitons*, vol. 661 of *Lecture Notes in Physics*, (pp. 37–54). Springer Berlin / Heidelberg. 38

Vicencio, R. A., Molina, M. I., & Kivshar, Y. S. (2003). Controlled switching of discrete solitons in waveguide arrays. *Opt. Lett.*, *28*(20), 1942–1944. 12, 70

W. H. Renninger, A. C., & Wise, F. W. (2008). Dissipative solitons in normal-dispersion fiber lasers. *Phys. Rev. A*, *77*(77), 023814. 37

Wang, J., & Yang, J. (2008). Families of vortex solitons in periodic media. *Phys. Rev. A*, *77*, 033834. 54

Yang, J. (2004). Stability of vortex solitons in a photorefractive optical lattice. *New J. Phys.*, *6*, 47. 54

Yang, J., Makasyuk, I., Bezryadina, A., & Chen, Z. (2004a). Dipole and quadrupole solitons in optically induced two-dimensional photonic lattices: Theory and experiment. *Studies in Applied Mathematics*, *113*(4), 389–412. 69

Yang, J., Makasyuk, I., Bezryadina, A., & Chen, Z. (2004b). Dipole solitons in optically induced two-dimensionalphotonic lattices. *Opt. Lett.*, *29*(14), 1662–1664. 69

Yang, J., Makasyuk, I., Kevrekidis, P. G., Martin, H., Malomed, B. A., Frantzeskakis, D. J., & Chen, Z. (2005). Necklacelike solitons in optically induced photonic lattices. *Phys. Rev. Lett.*, *94*, 113902. 69

Zabusky, N. J., & Kruskal, M. D. (1965). Interaction of "solitons" in a collisionless plasma and the recurrence of initial states. *Phys. Rev. Lett.*, *15*, 240–243. 3

Zakharov, V. E., & Shabat, A. B. (1974). Interaction between solitons in a stable medium. *SOVIET PHYSICS JETP*, *37*(5), 823–828. 5, 28

Zener, C. (1934). A theory of the electrical breakdown of solid dielectrics. *Proceedings of the Royal Society of London. Series A*, *145*(855), 523–529. 11